The Precision Magnetic Field Analysis for the Fermilab Muon g-2 Experiment

by

Alexander Tewsley-Booth

A dissertation submitted in partial fulfillment
of the requirements for the degree of
Doctor of Philosophy
(Physics)
in The University of Michigan
2019

Doctoral Committee:

Professor Timothy Chupp, Chair
Associate Professor Christine Aidala
Professor Wolfgang Lorenzon
Professor Georg Raithel
Professor John Schotland

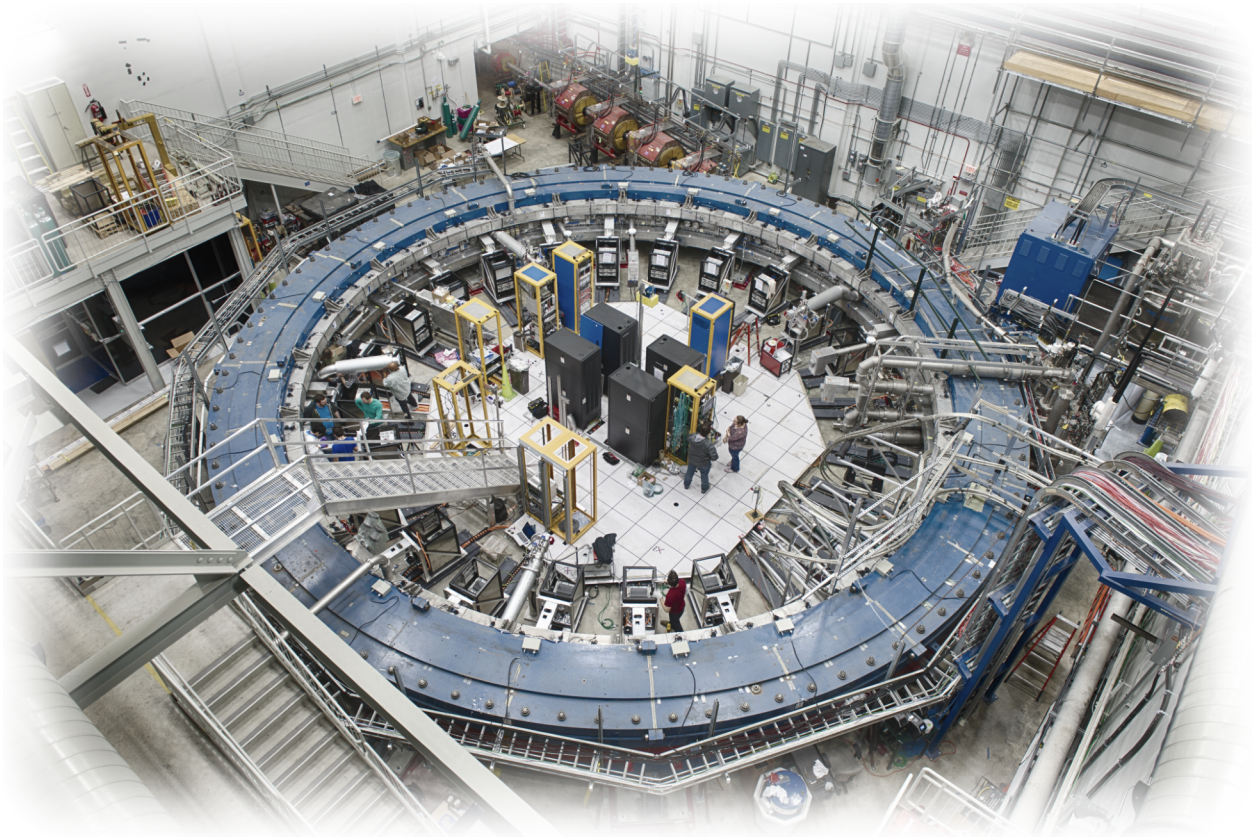

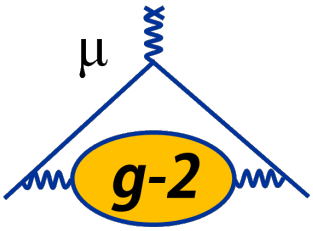
μ
g-2

Alexander Tewsley-Booth

aetb@umich.edu

ORCID iD: 0000-0002-6624-8522

To my wife Lily, for all her faith and support.

ACKNOWLEDGEMENTS

I want to thank my advisor, Tim Chupp, for helping me every step of the way towards this dissertation, explaining the importance of "Concept 1," and teaching me how to think in Allan deviations. I also want to thank my group mates: Natasha Sachdeva for all the discussion both about physics and not-physics; Midhat Farooq for being a ray of sunshine given human form; Chelsea Hendrus for her enthusiasm about so many cool things; and Eva Kraegeloh for all the ideas bounced back and forth. I want to extend a special thanks to Joe Grange, who always asked what he could do to help me succeed. I owe an enormous amount of thanks to everyone on the Muon $g-2$ field team. I want to especially call out Simon Corrodi for not bending to the pressures of ROOT; Brendan Kiburg for being the one to make me feel like part of the experiment; and Ran Hong for doing more than should be humanly possible. An additional thanks must be made to Rachel Osofsky, for both the illuminating discussions about the experiment and analysis, and the sanity-preserving, non-work-related conversations. Outside of my research, I want to thank all my friends here for being generally great people, including a special callout to Anthony Charles, my pocket theorist. Finally, I want to thank my family for everything they've done for me, especially my wife, Lily. But she already got the dedication page.

Funding acknowledgment

This work was supported by NSF grants PHY-1506021 and PHY-1812314 and the DOE SCGSR program.

TABLE OF CONTENTS

LIST OF FIGURES

Figure

LIST OF TABLES

Table

ABSTRACT

There is presently a disagreement between the theoretical prediction and experimental measurement of the muon's anomalous magnetic moment, $a_\mu = \frac{g_\mu - 2}{2}$,

$$a_\mu^{(expt.)} - a_\mu^{(theor.)} = (2,706 \pm 726) \times 10^{-12}.$$

Such a discrepancy could be a signal for new physics. The goal of Fermilab E989 is to make a more precise measurement of the muon's magnetic moment to 140 ppb to shed light on the current discrepancy. Part of the new measurement requires a precision measurement of the magnetic field averaged by the muon motion as they circulate in a 14 m diameter storage ring.

This work describes one of two independent analyses of measurements from the magnetometer systems to calculate the precision field map in the Run 1 data sets. It also lays out the framework for averaging the magnetic field in both time and space, weighted by the muon distribution. The field is precisely mapped using a trolley that carries 17 NMR probes around the muon storage region. The field's behavior in the times between the trolley scans is interpolated using an array of 378 NMR probes positioned around the outside of the muon storage region. The results are maps of the magnetic field as functions of time and space in the storage ring. Conservative estimates of the systematic uncertainties are also made for each data set in Run 1, with suggested improvements in both the data taking methods and future analyses.

CHAPTER I

Introduction

Fermilab E989, the Muon $g-2$ experiment, represents the efforts of many collaborating scientists, engineers, and technicians, to perform the most precise measurement of the muon's anomalous magnetic dipole moment to date. The experiment is a massive effort with many parts that must work together, but this work focuses on the aspects of the precision measurement of the magnetic field and the interpolation of a full field map in which the author was significantly involved. The experiment collects data in "runs," with one run per year, separated by scheduled downtime at Fermilab. Within each run, the data are further categorized into data sets lasting on the order of days to weeks. This work focuses on the analysis of the first run. Run 1 nominally covered the 2017–2018 year, but all the production data sets come from early 2018. At the time of writing, Run 2 has been completed, and Run 3 is about to start data taking.

This chapter explains the motivation for a precision measurement of the muon's anomalous magnetic dipole moment, $a_\mu = \frac{g-2}{2}$, and provides historical context to the experiment. Chapter II outlines the principle of measurement and the Standard Model prediction of a_μ. Chapter III begins to cover the various measurements that must be performed simultaneously to calculate a_μ. It also provides an overview of the systems required to make the measurements. Chapter IV focuses on the set of subsystems that are used to make the precision magnetic field measurement and emphasizes the calibration chain connecting the various subsystems. Chapter VI explains in detail the author's algorithm that takes large sets of magnetometer measurements and interpolates them to produce a magnetic field map over time and space. Chapter VII goes on to detail how the field map is combined with the muon distribution to calculate the average magnetic field experienced by the muons while they are in the storage ring. Finally, Chapter VIII provides details on the systematic corrections and uncertainties determined from the measurements, calculations, and dedicated systematics tests. Chapter IX presents the muon-weighted average fields for the main data sets of Run 1, and lays out an outline for the path forward to reach the goals for the uncertainties.

1.1 Motivation

The magnetic moment of the electron, often expressed by its g-factor g_e or its anomalous magnetic moment $a_e = \frac{g-2}{2}$, is one of the most precisely measured quantities today [1]. It provides an unparalleled test of quantum electrodynamics, which shows remarkable agreement with experiment. As a heavier version of the electron, a muon might be supposed to have a magnetic moment that is also in agreement with the prediction of the standard model. However, this turns out not to be the case. Because the muon is approximately 200 times heavier than the electron, it is about $40,000$ more sensitive to effects caused by off-shell massive virtual particles, including possibly undiscovered particles, such as those predicted by supersymmetric theories or dark matter candidates. Because of this sensitivity, when Brookhaven E821, a muon $g-2$ experiment, observed a discrepancy with the Standard Model prediction [2] scientists launched a dedicated effort to improve both the experimental and theoretical uncertainties, both to confirm the observed discrepancy and to understand what sort of physics beyond the Standard Model the muon anomalous magnetic moment could reveal. Fermilab E989 is the successor to Brookhaven E821 and seeks to reduce the total uncertainty by a factor of four by improving both statistical and systematic uncertainties.

1.2 History

Since the discovery of parity violation by Lee, Yang, and Wu [3, 4], experimenters have designed experiments that measure the magnetic moment of the muon by observing the parity-violating asymmetry in the muon decay to electrons (see Section 3.3 for further discussion). Early experiments used stopped muons in a magnetic field, which permitted low-precision measurements of the muon g-factor that provided early evidence that the muon behaved as a heavy electron [5]. By 1960, the magnetic moment of the muon was measured precisely enough to agree with the lowest-order prediction of QED [6].

The CERN Experiments

The first experiment carried out at CERN was motivated as a precision test of QED, beyond the first-order radiative corrections calculated by Julian Schwinger [7]. The experiment was searching for a breakdown of QED at high energies, which would manifest as a modified anomalous magnetic moment. The experiment used non-relativistic muons, drifting in a magnetic gradient, that were then stopped, and the forward-backward decay asymmetry was measured. CERN I measured a_μ to the $5,000$ ppm level in 1962 [8]. The main limiting

factor on its measurement was the 2.2 μs lifetime of the muon that drastically limited the number of measured muon decays [5].

CERN II improved the low muon lifetime by using relativistic muons. It was the first muon $g-2$ experiment to use a storage ring. Muons were injected with $\gamma = 12.06$, which increased their lifetime in the lab frame to 26.5 μs. The extended lab frame lifetime allowed CERN II to measure a_μ with a precision of 270 ppm [9]. The improvement on the previous result's precision by a factor of 20 allowed CERN II to test QED through three-loop level. However, the low number of stored muons and the background signal in the detectors caused by putting the pion production target in the ring limited the experimental precision [5].

In CERN II, vertical beam focusing was achieved using magnetic gradients. However, as precision increased, it became necessary to use a more uniform magnetic field. CERN III used electric quadrupoles to provide vertical focusing, allowing the magnetic field to be more uniform. However, electric focusing introduced a new problem. In the fully relativistic treatment of spin precession in electromagnetic fields, there is a term in the precession frequency proportional to the external electric field (see Equation 2.7). However, it is possible to reduce that term to zero (or at least make it small) by choosing a muon momentum such that

$$a_\mu - \frac{1}{\gamma^2 - 1} \approx 0. \tag{1.1}$$

(See Section 2.1.2 for the mathematical formulation.) The solution to this equation is $\gamma = 29.3$, which has the added benefit of extending the lab frame muon lifetime to 64.3 μs, allowing longer measurement times.

Besides the more uniform magnetic field and longer measurement times, CERN III also improved the particle injection into the ring. Instead of injecting protons, with a pion production target in the ring, a beam of pions were injected into the ring, which reduced the background signal in the detectors so the measurement could begin sooner after injection. These improvements allowed CERN III to measure a_μ to 7.3 ppm precision [10]. At this level, the measurement could be compared to theory, including QED through the three-loop level plus the hadronic contribution. It was not sensitive to the electroweak contribution to the theoretical value [5].

Brookhaven E821

The goal of Brookhaven E821 was to observe the electroweak contribution to a_μ and any contributions from new physics. The experiment used the CERN III "magic momentum" that canceled the electric field contribution and made additional, significant improvements.

The magnetic field and field measurements systems were improved. The field was much more uniform, and an array of 378 fixed plus 17 trolley-based NMR magnetometers were added, including a trolley that could map the field in the vacuum chamber at the location of the muons. The electric quadrupole focusing was improved, creating a more uniform muon spatial distribution. Collimators were inserted into the storage ring, which reduced the dependence of higher-order beam moments in the muon-weighted field average. Finally, the experiment used direct muon injection with a much more intense beam than at CERN. Even so, E821 was ultimately statistics limited [5].

The final result from E821 measured $a_\mu^{\text{E821}} = 1165920890(640) \times 10^{-12}$ [2], an uncertainty of 0.54 ppm. Combined with previous experiments, this leads to a current world average of $a_\mu^{\text{expt. avg.}} = 1165920890(630) \times 10^{-12}$ [11]. Comparing this to a current theoretical calculation, $a_\mu^{\text{theory}} = 1165918204(356) \times 10^{-12}$, there is a difference

$$a_\mu^{\text{expt.}} - a_\mu^{\text{theory}} = 2706(726) \times 10^{-12} \tag{1.2}$$

between the experiment and theory of 3.7σ [12].

Fermilab E989

The observation of this discrepancy led to the formation of Fermilab E989, dedicated to driving down the experimental uncertainty. In concert with a coordinated theory effort, the goal is to confirm or refute the experimental disagreement with the Standard Model. E989 is in many ways a continuation of E821; it evens uses the same magnet, which was shipped from Brookhaven to Fermilab. The specifics of E989 are covered more fully in this work, but a general outline of notable upgrades over the previous experiment are listed here:

1. The new experiment takes advantage of the new muon beamline at Fermilab, which has a purer beam with higher intensity and faster fill rate.

2. The kicker, which puts injected muons onto a stable orbit in the ring, has been upgraded for a faster kick.

3. The calorimeters used for the decay positron detection have also been improved to increase sensitivity, especially to muons lost from the ring.

4. Two "straw trackers" have been installed that allow a non-destructive direct measurement of the beam profile during production runs.

5. The magnetic uniformity has been improved, as well as the measurement systems and algorithms to calculate $\widetilde{\omega}_p$ [5].

For a more in-depth discussion of these systems, see Chapter III.

CHAPTER II

Theoretical Background

2.1 Magnetic Moments and Spin Precession

Charged elementary particles, or composite particles of charged constituents, have intrinsic magnetic dipole moments (MDMs) directed along the same axis as their spin. MDMs lead to a rich array of behaviors when the particle is moving through an external electromagnetic field. The Standard Model can be used to predict the magnitude of the MDMs, and the agreement between the theory and experiment for the electron magnetic moment is the best precision test of the Standard Model, with a relative uncertainty on the measurement of the electron $g-2$ of 1.7×10^{-13} [11]. For Fermilab E989, the precession of an MDM that is not parallel to an external field around the field gives us insight into how to measure the MDM.

2.1.1 The Classical Picture

A magnetic dipole in an external magnetic field exhibits several behaviors that one can measure to probe the properties of the dipole. The potential energy of a dipole in an external field is

$$U = -\boldsymbol{\mu} \cdot \mathbf{B}, \tag{2.1}$$

where μ is the magnetic dipole moment and $\mathbf{B}$ is the external field, which implies that the minimum energy occurs when the moment and field are aligned, and the maximum energy occurs when the moment and field are anti-aligned. There also exists a torque on the dipole

$$\tau = \mu \times \mathbf{B}. \tag{2.2}$$

In particles, the magnetic moment must lie be along the same axis as the spin, allowing the expression $\mu = \gamma \mathbf{S}$, where γ is the particle's gyromagnetic ratio and $\mathbf{S}$ is its spin. A particle

at rest has no orbital angular momentum, so the total angular momentum equals its spin. Therefore, we can write

$$\tau = \frac{\mathrm{d}\mathbf{S}}{\mathrm{d}t} = \gamma \mathbf{S} \times \mathbf{B}. \tag{2.3}$$

The torque is always perpendicular to both $\mathbf{S}$ and $\mathbf{B}$, causing the initial spin to precess about the field with a frequency $|\omega| = |\gamma B|$. An experiment that simultaneously measures the particle's spin precession and the external magnetic field can be used to calculate γ.

The gyromagnetic ratio of a particle is an intrinsic quantity, and is defined by $\gamma = g\frac{q}{2m}$ where q is the particle's charge, m is its mass, and g is the "g-factor," a unitless constant that arises from the relationship between the particle's magnetic dipole moment and its spin. In the classical picture of a spinning ball of charge $g = 1$, but this turns out to not be correct for elementary particles.

2.1.2 Relativistic Extension

Spin precession in a magnetic field becomes significantly more complicated than explained in Section 2.1.1 when we allow for the possibility of an external electric field and consider relativistic effects. A fully relativistic expression for the spin precession of a magnetic moment in an external electromagnetic field in the lab frame is [13]

$$\frac{\mathrm{d}\mathbf{S}}{\mathrm{d}t} = \frac{e}{2m}\mathbf{S} \times \left[\left(g - 2 + \frac{2}{\gamma} \right) \mathbf{B} - (g-2)\frac{\gamma}{\gamma+1}(\boldsymbol{\beta} \cdot \mathbf{B})\boldsymbol{\beta} - \left(g - 2\frac{\gamma}{\gamma+1} \right) \boldsymbol{\beta} \times \mathbf{E} \right]. \tag{2.4}$$

The first term of this equation, $\frac{ge}{2mc}\mathbf{S} \times \mathbf{B}$, is identical to the non-relativistic equation for the spin precession, so we can consider the other terms to be corrections. All the terms that are proportional to g come from the motional magnetic field, which is the effective magnetic field experienced by a particle in its rest frame and is calculated by a Lorentz transformation from the fields in the lab frame. The terms that are not proportional to g come from the Thomas precession, which is a relativistic effect coming from the curving path of the particle in the lab frame. This causes an effective rotational velocity of the particle's rest frame of

$$\omega_T = \frac{\gamma^2}{\gamma+1}\frac{\mathbf{a} \times \mathbf{v}}{c^2}, \tag{2.5}$$

where $\mathbf{a}$ is the particle's acceleration, and $\mathbf{v}$ is its velocity.

A useful expression that can be derived from Equation 2.4 is for the time derivative of the projection of the spin along the muon's momentum. This is essentially the rate at which the angle between the momentum vector and the spin vector changes, which is important for

the experimental measurement as explained in Section 3.1. The equation for this quantity is

$$\frac{\mathrm{d}}{\mathrm{d}t}(\hat{\boldsymbol{\beta}} \cdot \mathbf{S}) = -\frac{e}{m}\mathbf{S}_{\perp} \cdot \left[a\hat{\boldsymbol{\beta}} \times \mathbf{B} + \beta \left(a - \frac{1}{\gamma^2 - 1} \right) \mathbf{E} \right]. \tag{2.6}$$

Note that, here, a is the anomalous magnetic moment defined in Equation 2.15. The rate of change of the angle between the momentum and spin vector, called the anomaly frequency ω_a, is therefore

$$\boldsymbol{\omega}_a = \frac{e}{m} \left[a\mathbf{B} - \left(a - \frac{1}{\gamma^2 - 1} \right) \boldsymbol{\beta} \times \mathbf{E} \right]. \tag{2.7}$$

Three important results can be seen immediately from this equation. First, if a particle had a zero anomalous magnetic moment and were in a magnetic field (but not an electric field), the anomaly frequency would be zero, meaning that the spin and momentum vectors would precess at the same rate and the angle between them would be constant. Second, the term proportional to the electric field can be eliminated by setting

$$\left(a - \frac{1}{\gamma^2 - 1} \right) = 0. \tag{2.8}$$

For a charged lepton, to first order the anomalous magnetic moment is $\frac{\alpha}{2\pi}$ where $\alpha \approx 1/137$ is the fine structure constant (see Section 2.2.1). Choosing a momentum such that $\gamma \approx 29.36$ cancels any effect the electric field has on the anomaly frequency, which in this experiment corresponds to a momentum of 3.094 GeV/c. Third, assuming no contribution from the electric field term, the anomaly frequency is directly proportional to the product of the anomalous magnetic moment and the magnetic field. This relationship is the key to understanding how the anomalous magnetic moment is measured experimentally (see Section 3.1).

2.1.3 The Quantum Picture

The quantum treatment of the magnetic dipole moment in an external magnetic field produces the same result for the spin precession. A dipole in an external field (without loss of generality oriented along the z-axis) has the Hamiltonian

$$H = -\gamma \mathbf{S} \cdot \mathbf{B} = \begin{pmatrix} -\gamma\hbar B/2 & 0 \\ 0 & \gamma\hbar B/2 \end{pmatrix}, \tag{2.9}$$

where the Hamiltonian acts on the 2-state system

$$\psi = \begin{pmatrix} |\uparrow\rangle \\ |\downarrow\rangle \end{pmatrix}. \tag{2.10}$$

A state that is a superposition of the up and down spin states (any state with a component along the x- or y-axis) will have an evolving relative phase between the up and down spin states at a frequency $\omega = \frac{1}{\hbar}\Delta E$ where ΔE is the difference in the energies of the eigenstates. By projecting onto the x and y bases, this evolving phase can be interpreted as the state oscillating between the spin $+x$, $+y$, $-x$, and $-y$ states. The frequency is $\omega = \gamma B$, recovering the classical result of the precession frequency as the state precesses around the z axis. However, neither the classical nor the non-relativistic quantum treatments make a prediction for the value of g.

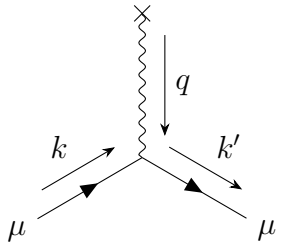

Figure 2.1: The Dirac vertex function.

The Dirac equation, the relativistic extension of the Schrodinger equation, can be used to make a prediction for the value of g. To tree-level, the S-matrix element for the scattering from a classical external field (Figure 2.1) is

$$iM = -ie\bar{u}(k')\gamma^i u(k) \cdot \tilde{A}_i(q), \tag{2.11}$$

where $A = (0, \mathbf{A}(x))$ is the 4-vector of the external magnetic potential. Taking the non-relativistic expansion of the spinors through first order in momentum and keeping only the spin-dependent term, this expression simplifies to

$$iM = -i(2m)\ e\xi'^{\dagger}\left(\frac{-i}{2m}\epsilon^{ijk}q^j\sigma^k\right)\xi \cdot \tilde{A}_\mu(q). \tag{2.12}$$

We can identify $-i\epsilon^{ijk}q^i\tilde{A}^i = \tilde{B}^k$, where B^k is the magnetic field, which allows the subsitution

$$iM = -i(2m)\ \frac{-e}{2m}\xi'^{\dagger}\sigma^k\xi\tilde{B}^k, \tag{2.13}$$

which we interpret as the Born approximation for scattering from the potential

$$U = -\frac{e}{m}\mathbf{S} \cdot \mathbf{B}, \tag{2.14}$$

which is the potential for a magnetic moment in an external field. Setting $\gamma = e/m$, we find $g = 2$ [14]. Including higher-order corrections adds a small correction to the result $g = 2$

that is called the *anomalous magnetic moment*. The anomalous magnetic moment is often written mathematically as

$$a = \frac{g-2}{2} \tag{2.15}$$

to express that is is a deviation from the tree-level value.

2.2 The Standard Model

The muon anomalous magnetic moment appears in calculations as part of the vertex function (see Figure 2.2) that describes the interaction between the muon and a photon. At tree level, the vertex function is [14]

$$\Gamma^{\mu} = -ie\gamma^{\mu}. \tag{2.16}$$

However, when one starts to account for radiative corrections, the physical Γ^{μ} picks up additional terms. Satisfying both Lorentz Invariance and the Ward Identity, a more general Γ can be written

$$\Gamma^{\mu}(k,k') = \gamma^{\mu}F_1(q^2) + \frac{i\sigma^{\mu\nu}q_{\nu}}{2m}F_2(q^2). \tag{2.17}$$

Here, F_1 and F_2 are functions of q^2 called the form factors. Comparing this to the tree level result, we see that at lowest order, $F_1(0) = 1,\ F_2(0) = 0$. $F_1(0)$ is the electric charge and $F_2(0)$ is the anomalous magnetic moment. Calculating the corrections to the muon anomalous magnetic moment, therefore, is a matter of calculating the radiative corrections to the form factor $F_2(0)$ [14].

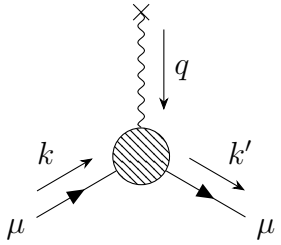

Figure 2.2: The physical vertex function.

The Standard Model prediction for the muon anomalous magnetic moment a_{μ} can be broken up into contributions from different sectors. This is generally written

$$a_{\mu}^{\mathrm{SM}} = a_{\mu}^{(QED)} + a_{\mu}^{(EW)} + a_{\mu}^{(had)}, \tag{2.18}$$

where $a_\mu^{(QED)}$ is the contribution from quantum electrodynamics, $a_\mu^{(EW)}$ is the contribution from electroweak theory, and $a_\mu^{(had)}$ is the contribution from quantum chromodynamics. The hadronic term further splits into two parts, $a_\mu^{(HVP)}$ and $a_\mu^{(HLbL)}$, corresponding to the hadronic vacuum polarization and light-by-light corrections, respectively; more detailed descriptions of each of these contributions follow. Table 2.1 summarizes the current state of the field of standard model calculations. Notice that contributions from QED dominate the anomalous magnetic moment but are known to the highest absolute precision. The uncertainty is dominated by the hadronic corrections, due to the difficulty in performing calculations in QCD.

Contribution	a_μ ($\times 10^{-12}$)	σa_μ ($\times 10^{-12}$)
QED	1165847189.7	0.7
EW	1536	10
HVP	68468	242
HLbL	980	260
total	1165918204	356
expt.	1165920910	632
diff.	2706	726

Table 2.1: Current values for the Standard model contributions to the muon anomalous magnetic moment and their uncertainties [12]. Also included are the current world average experimental value, and the difference between experiment and theory [15].

2.2.1 QED Contribution

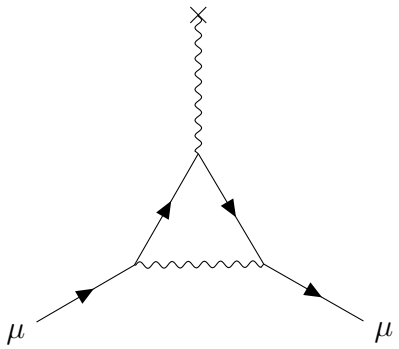

Figure 2.3: The Schwinger term diagram.

The muon $g-2$ is dominated by QED. This includes all interactions which are composed of only leptons and photons. The QED contribution, a_μ^{QED}, can be written as a the perturbative expansion

$$a_\mu^{(QED)} = \sum_n \left(\frac{\alpha}{\pi}\right)^n a_\mu^{(2n)}, \tag{2.19}$$

where α is the fine structure constant [16]. The value of $a_\mu^{(2)}$ is famously $\frac{1}{2}$, calculated by Julian Schwinger in 1948 [7], leading to $a_\mu^{(QED)} = 1161409733 \times 10^{-12}$ at the $n = 1$ level (using the current accepted value of α [11]). It corresponds to the Feynman diagram in Figure 2.3. The higher loop order diagrams of the sort seen in Figure 2.4 have been calculated through $n = 5$ by Kinoshita *et al.* and found to be $a_\mu^{(QED)} = (1165847189.7 \pm 0.7) \times 10^{-12}$[16, 17]. This number depends on the value used for α, which can be found in different ways. This calculation uses a value of α calculated by direct measurements in rubidium [18]. Kinoshita notes that a more precise calculation of α can be done using the electron $g - 2$, but that the theoretical calculation of a_e is highly correlated to that of a_μ, which requires increased caution [16].

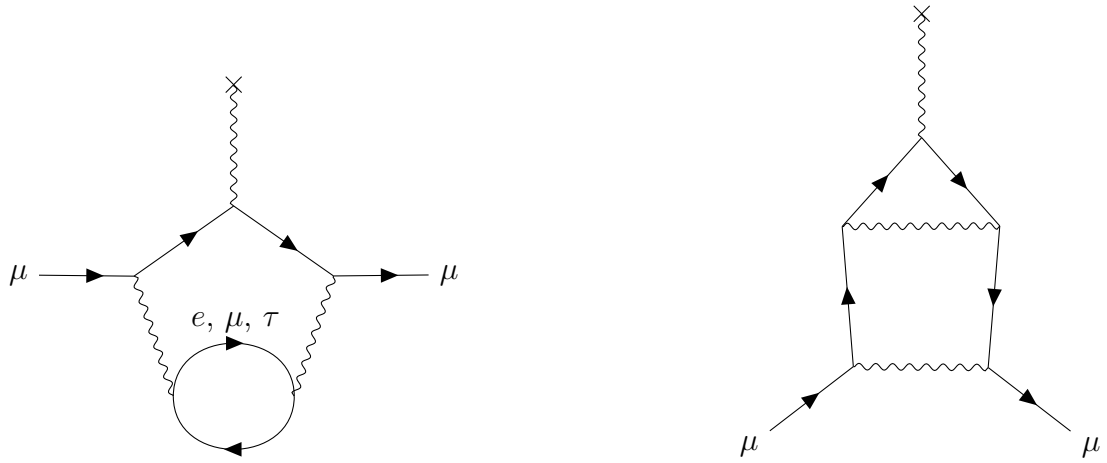

(a) Muon mass dependent

(b) Muon mass independent.

Figure 2.4: Sample μ $g-2$ two-loop Feynman diagrams for the QED contribution. The mass-dependent terms are different for the muon compared the electron, because the muon's higher mass leads to an enhancement of terms with heavy virtual particles. The mass-independent terms are the same for both the muon and the electron.

The uncertainty in a_μ^{QED} is driven by uncertainties in the lepton mass measurements and statistical uncertainties from Monte Carlo integration techniques. However, its contribution to the uncertainty of the total anomalous magnetic moment is still sub-ppb, which is below the precision of Brookhaven E821, the expected precision of Fermilab E989, and the uncertainties from the calculations of the other SM contributions to a_μ^{SM}.

2.2.2 Weak Sector Contribution

The electroweak contribution to the total anomalous magnetic moment, $a_\mu^{(EW)}$, covers all terms that include weak or Higgs bosons. Figure 2.5 shows the two first-order diagrams, which correspond to the emission and reabsorption of a neutral boson (Z or H), or the conversion of the muon into a charged boson (W) and neutrino and their subsequent recombination.

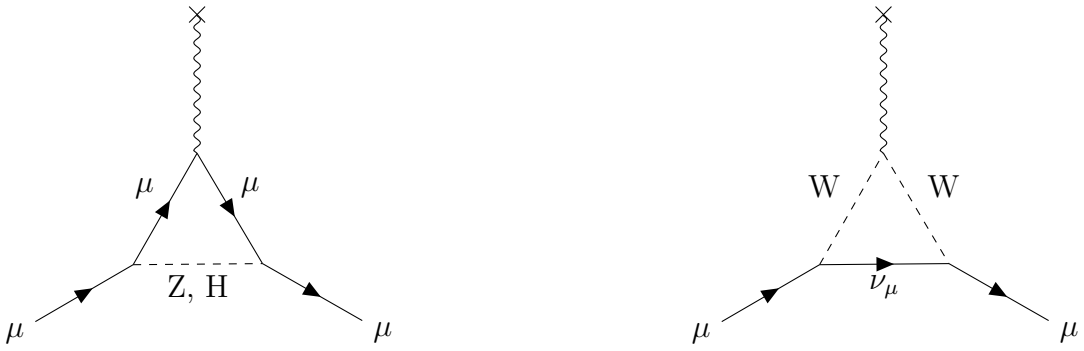

(a) Neutral bosons (b) Charged bosons

Figure 2.5: Leading order diagrams for $a_\mu^{(EW)}$.

This contribution is small compared to the total a_μ because the virtual bosons are much heavier than the muon, leading to large suppressing factors on the amplitudes. The SM contribution has been calculated through second-order [19] and is

$$a_\mu^{(EW)} = (1536 \pm 10) \times 10^{-12}. \tag{2.20}$$

The uncertainty in this calculation is dominated by hadronic uncertainties in the two-loop diagrams, such as those seen in Figure 2.6. This uncertainty is larger than the QED uncertainty, but it is still small compared to both the experimental precision and the hadronic calculations' uncertainties.

2.2.3 Hadronic Sector Contribution

Interactions that include quarks but neither the weak nor Higgs boson are categorized as hadronic contributions to a_μ^{SM}. Although their contribution to a_μ^{SM} is small, their uncertainties dominate the total uncertainty, because a_μ^{had} cannot be calculated perturbatively. Instead, a_μ^{had} must be calculated through other methods. The hadronic contributions are divided into two parts: the hadronic vacuum polarization contribution (HVP) and the hadronic light-by-light contribution (HLbL).

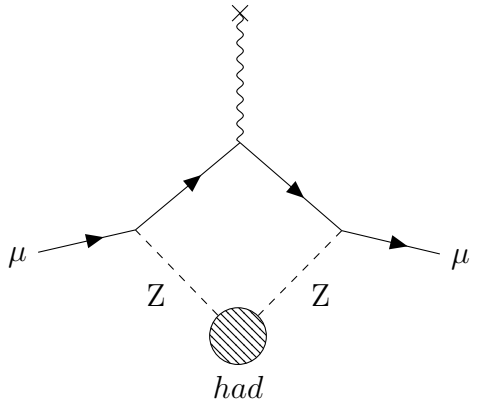

Figure 2.6: Example EW diagram including hadronic terms.

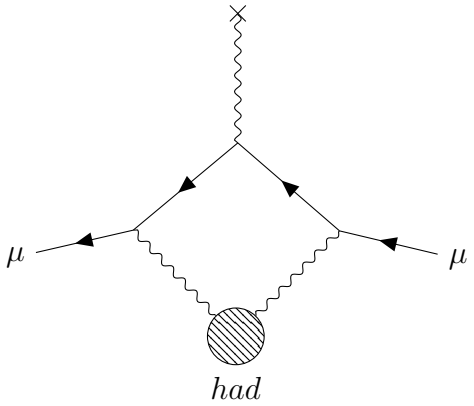

(a) Hadronic vacuum polarization (HVP)

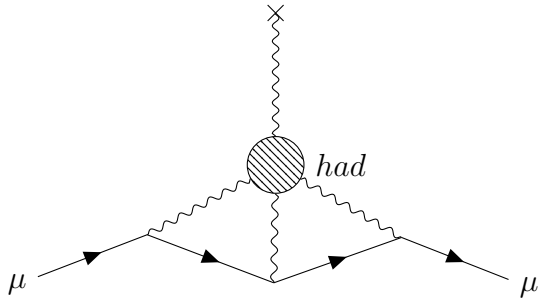

(b) Hadronic light-by-light (HLbL)

Figure 2.7: Leading order diagrams for hadronic sector.

Hadronic vacuum polarization contribution (HVP) The leading-order (LO) contribution to $a_\mu^{(HVP)}$ is shown in Figure 2.7a. HVP diagrams differ from leptonic vacuum polarization ones because the hadronic loop includes QCD interactions that cannot be calculated perturbatively. Instead, they are evaluated using dispersion relations and experimentally measured cross sections for $ee \to$ hadrons. The analysis involves combining cross section measurements for different hadronic channels from different experiments. Keshavarzi *et al.* (KNT18) [12] find the values

$$a_\mu^{(HVP,\ LO)} = (69326 \pm 246) \times 10^{-12} \tag{2.21}$$

$$a_\mu^{(HVP,\ NLO)} = (-982 \pm 4) \times 10^{-12}. \tag{2.22}$$

Other independent calculations are in agreement with these numbers within uncertainty (DHMZ17 [20], FJ16 [21]). For example, Davier *et al.* (DHMZ17) [20] find

$$a_\mu^{(HVP,\ LO)} = (69230 \pm 420) \times 10^{-12}. \tag{2.23}$$

Work on NNLO terms [22] has produced the value

$$a_\mu^{(HVP,\ NNLO)} = (124 \pm 10) \times 10^{-12}. \tag{2.24}$$

Combining these three contributions yields [12]

$$a_\mu^{(HVP)} = (68468 \pm 242) \times 10^{-12}. \tag{2.25}$$

Efforts are also being made to supplement the dispersion calculation with other methods. Blum *et al.* [23] performed a first-principles calculation of the LO HVP via lattice QCD. Their result had an uncertainty an order of magnitude larger than the KNT18 result and was consistent within uncertainty. When they supplemented the lattice data at short and long distances with experimental data as described above, they arrived at $a_\mu^{(HVP,\ LO)} = (69250 \pm 270) \times 10^{-12}$, which is in agreement with and comparable to the KNT18 number. Additionally, an experiment that can directly measure $a_\mu^{(HVP,\ LO)}$ via μe scattering has been proposed [24].

Hadronic light-by-light contribution (HLbL) Like the HVP calculation, the HLbL cannot be calculated with a perturbative approach. Previous calculations of it, such as the "Glasgow consensus" [25] were highly model dependent, and, unlike the HVP, could not be calculated using a data-driven approach. Note that the original Glasgow consensus value for

$a_\mu^{(HLbL)}$ has since been found to contain a small error [21]. A corrected value is [26]

$$a_\mu^{(HLbL)} = (980 \pm 260) \times 10^{-12}. \tag{2.26}$$

There is a significant push by the $g-2$ theory community to improve the calculation of this term. Despite being the smallest contribution to the total value of a_μ^{SM}, it has the greatest uncertainty. Current efforts focus on applying both lattice QCD and dispersion relations, such as those mentioned used in the HVP calculation. Even though both methods are significantly more complicated than in the HVP case with more work needed to make a complete estimate of $a_\mu^{(HLbL)}$, significant progress has already been made [27].

2.3 Beyond the Standard Model

If there are no errors in either the experimental determination of a_μ or the calculations described in Section 2.2, then new "Beyond the Standard Model" (BSM) physics is required to explain the discrepancy. Despite not having the same level of experimental precision as the electron anomalous magnetic moment, the muon provides a better testing ground for BSM physics because effects are typically proportional to m^2/Λ^2, where m is the mass of the particle (the electron or muon, in this case) and Λ is the mass scale of the new physics. There is a relative enhancement of BSM physics in the muon over the electron of $m_\mu^2/m_e^2 \approx 42,750$ [28]. Many theories exist that can account for the experimental discrepancy including supersymmetry (SUSY), alternative Higgs, weak theories in a "dark sector", and axion-like particles.

Supersymmetry

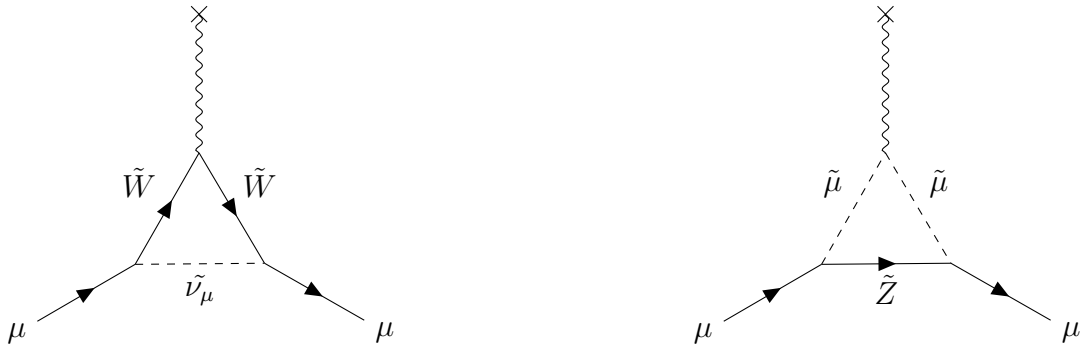

(a) Sneutrino-wino loop (b) Smuon-neutralino loop

Figure 2.8: Sample diagrams involving supersymmetric particles.

SUSY remains a popular theory for explaining the discrepancy between experimental results and the Standard Model prediction [28]. It would enter at leading order to the calculation of a_μ through a vertex loop including either a sneutrino-wino loop or a smuon-neutralino loop as seen in Figure 2.8[28, 29]. Experiments at the LHC have excluded many regions of parameter space for SUSY theories that can explain the muon $g-2$ discrepancy by excluding mass ranges for the wino and higgsino particles. However, there still exist a couple of regions that are not excluded by the LHC that could also explain the muon $g-2$ [30].

Alternative Higgs

Extensions to the Higgs mechanism can resolve the experimental-Standard Model discrepancy. One simple theory is the two-Higgs doublet model (2HDM), where a second Higgs doublet leads to more abundant parameter space that could solve not just the muon anomalous magnetic moment discrepancy but also other open questions in high energy physics, like dark matter and neutrino masses [31, 32]. Other extensions to the Standard Model Higgs mechanism have also been proposed, such as a light scalar particle arising from the Higgs mechanism operating in a "dark sector" [33].

Dark Sector

Another extension to the standard model that could resolve the anomalous magnetic moment discrepancy is the addition of one or more additional "dark bosons" that interact weakly with the muon. One attractive option would be a dark photon, which has been the target of many experimental searches [34, 35]. However, at the current time, other experiments have excluded the region of parameter space where a dark photon explains the muon's anomalous magnetic moment [36]. Other dark boson theories exist, though, that could still resolve the tension between the standard model and experiment [37, 38].

Axion-like Particles

Light spin-0 particles, referred to as axion-like particles (ALPs) can arise naturally in extensions to the Standard Model. ALPs form a vast class of interactions with many free parameters that must be set by experiments (see Figure 2.9). The muon $g-2$ could prove to be a sensitive probe of the parameter space for ALP physics [39].

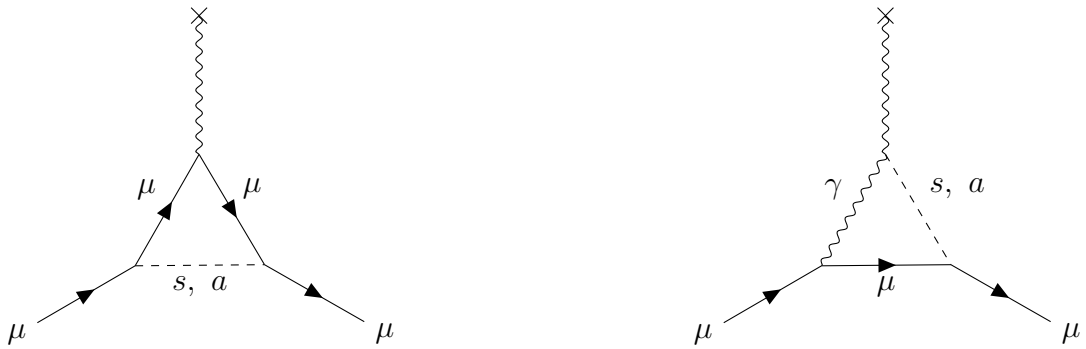

Figure 2.9: Leading order diagrams for axion-like particle contributions to a_μ. Here s represents a scalar ALP while a represents a pseudoscalar ALP.

CHAPTER III

Experimental Overview

3.1 The Required Measurements

The principle behind measuring a_μ is demonstrated by Equation 2.7. After choosing gamme such that the term proportional to the electric field is zero, we can write

$$\omega_a = a_\mu \frac{e}{m_\mu} B. \tag{3.1}$$

With a measurement of the anomaly frequency ω_a and the magnetic field B, and precise knowledge of e and m_μ (the charge and mass of the muon), we could calculate the value of a_μ. It is useful to redefine e and B in terms of other constants, for reasons that will be seen momentarily.

First, the electric charge of the muon, e, is equal to the electric charge of the electron. We can rewrite the charge of the electron as

$$e = \frac{4 m_e \mu_e}{\hbar g_e} \tag{3.2}$$

using the definition of the magnetic moment μ_e of the electron. Then, because the experiment uses NMR probes calibrated to the shielded proton in water to measure the magnetic field, it is convenient to write the magnetic field in terms of the precession frequency of the (shielded) protons

$$B = \frac{\hbar \omega_p'}{2 \mu_p'}. \tag{3.3}$$

Substituting into Equation 3.1, we can rewrite it as

$$a_\mu = \frac{g_e}{2} \frac{m_\mu}{m_e} \frac{\mu_p'}{\mu_e} \frac{\omega_a}{\omega_p'}. \tag{3.4}$$

The experiment must be run for long periods of time to gain statistical significance. Therefore, the two measured quantities, ω_a and ω_p' must be averages over the data sets. The measurement of ω_a is naturally a statistical average, due to the method used to calculate it (see Section 3.3). The natural measurement of the magnetic field, however, is based on a time-dependent field map — a measurement of the magnetic field at all times and points in the storage ring. The field map must be averaged, weighted by the muon distribution, to find the average field experienced by a muon during the data set. This weighted average is generally written $\widetilde{\omega}_p'$, and so the final equation for a_μ is

$$a_\mu = \frac{g_e}{2}\frac{m_\mu}{m_e}\frac{\mu_p'}{\mu_e}\frac{\omega_a}{\widetilde{\omega}_p'}. \tag{3.5}$$

The reason for expressing a_μ this way is that each of the first three fractions are unitless and have been measured at precisions high enough to meet the 100 ppb systematic uncertainty goal for the measurement of a_μ (see Table 3.1 for CODATA recommended values).

Constant	Value	Uncertainty
g_e	2.00231930436256	0.17 ppt
$\frac{m_\mu}{m_e}$	206.7682830	22 ppb
$\frac{\mu_p'}{\mu_e}$	0.00151923134	11 ppb

Table 3.1: CODATA recommended values for the constants and ratios in Equation 3.5 [11].

3.2 Muon Injection and Beam Dynamics

3.2.1 Muon Production

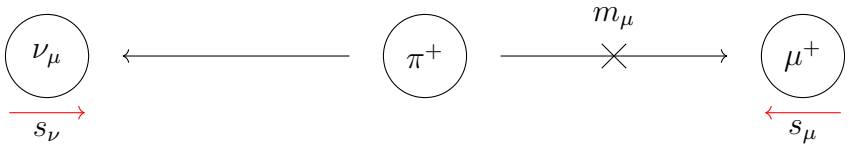

Figure 3.1: The decay of the pion at rest produces muons of definite helicity. Notice the helicity-flipping mass insertion that allows a right-handed chirality μ^+ to be produced with left-handed helicity, conserving angular momentum.

Muons are produced as the primary channel of charged pion decays. The pion decays into a muon and a muon neutrino, $\pi^+ \to \mu^+\nu_\mu$. Because this decay is mediated by the weak force,

Uncertainty source	E821 (ppb)	E989 (ppb)
ω_a statistical	460	100
ω_a systematics	180	70
$\widetilde{\omega}'_p$ sytematics		
Absolute calibration	50	35
Trolley probe calibration	90	30
Trolley measurements	50	30
Fixed probe interpolation	70	30
Muon distribution	30	10
Time-dependent external fields	-	5
Others	100	30
$\widetilde{\omega}'_p$ **total**	170	70
Total	540	140

Table 3.2: A comparison of the final uncertainties from Brookhaven E821 [2] and the proposed error budget for Fermilab E989 [40].

the decay products are naturally polarized. This is because the weak force only interacts with left-handed particles and right-handed anti-particles. In the case of the positive pion above, this means that the (near-massless) neutrino will have left-handed helicity. Because the pion is spin 0, the anti-muon will also have left-handed helicity, to conserve angular momentum. This is also the reason that pions decay to muons more often than electrons, despite the electron decay having more phase space available. If the charged anti-lepton decay product was massless, it would have to be right-handed, making this decay forbidden through the weak interaction. A massive charged lepton can have a helicity different from its chirality, but this is mediated through the mass term in the Lagrangian. Therefore, a more massive muon is more likely to be produced in the parity-violating decay than the less massive electron. In the lab frame, if one collects only the highest energy muons (the muons that were boosted along the pion's trajectory), then their spins will be highly polarized anti-parallel to their momentum.

Muons are produced in the muon campus beamline at Fermilab (see Figure 3.2). Positive pions are produced by focusing an 8 GeV proton beam onto a production target. Positive particles with a momentum within approximately 10% of 3.11 GeV are collected and diverted into the M2 and M3 lines that capture 3.094 GeV muons from the pion decays. The beam is diverted into the Delivery Ring, which both provides time for the remaining pions to decay and for the muons to separate from any remaining protons. The protons are sent to an abort station while the muons travel through the M4 and M5 lines into the g-2 storage ring [40].

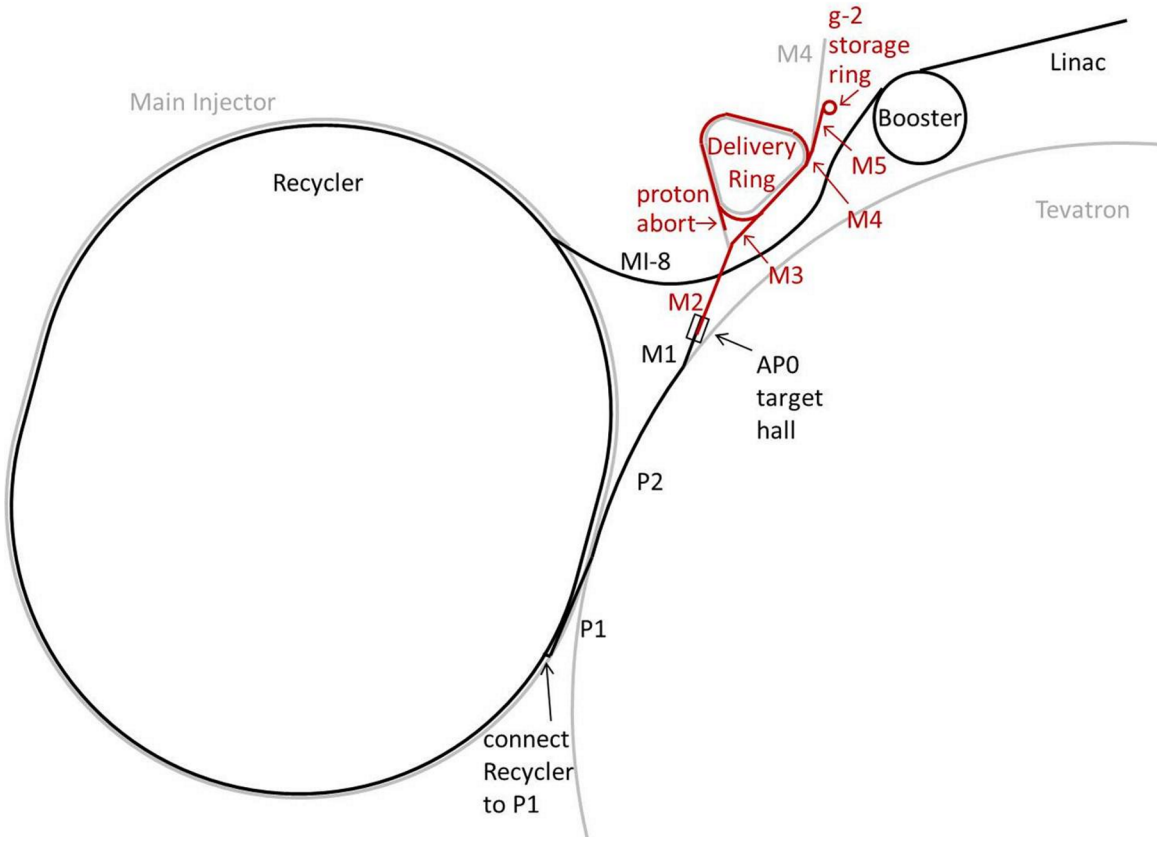

Figure 3.2: The muon campus beamline at Fermilab, reproduced from [40].

3.2.2 The Magnetic Storage Ring

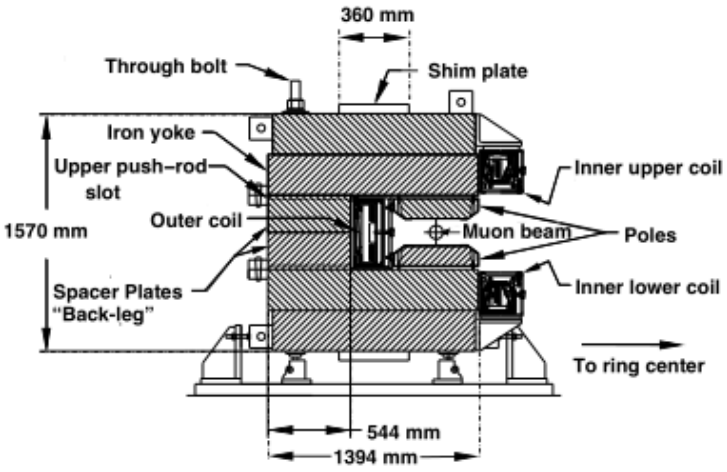

Figure 3.3: A cross section of the E989 magnetic storage ring, reproduced from [40]. Note the C-shaped iron yoke and pole pieces that direct the magnetic flux from the three coils and concentrate the field at the muon beam.

The magnetic storage rings used for E989 is the same ring that was used for E821, transported from Brookhaven to Fermilab. The ring uses C-shaped iron yokes to direct magnetic flux generated by three superconducting loops into a high-uniformity region at a nominal field of 1.451 T, centered at the muon's ideal orbit of 711.2 cm (see Figure 3.3). The magnet includes an extensive shimming kit — a set of passive controls and adjustable materials that provide fine control over the magnetic field over the full 44.69 m of the ideal orbit's azimuth, which will be covered in Chapter IV. The ideal magnetic field would be entirely directed vertically (in the $\hat{\mathbf{y}}$-direction), with no azimuthal, radial, or vertical gradients. The shimming kit is used to achieve this goal within acceptable levels. The field is controlled over a 9 cm diameter aperture centered on the muon's ideal orbit, which defines the muon storage region. Figure 3.4 shows the two main coordinates systems used when discussing the experiment.

3.2.3 The Electrostatic Quadrupoles

The magnetic field provides a restoring force in the radial direction, focusing the beam radially. However, it does not prevent the beam from defocusing and being lost vertically. Rather than use a magnetic field to achieve vertical focusing, which would make measuring the field experienced by the muons very difficult, electrostatic quadrupoles provide vertical focusing (see Figure 3.5). The electric field they produce creates a restoring force in the ver-

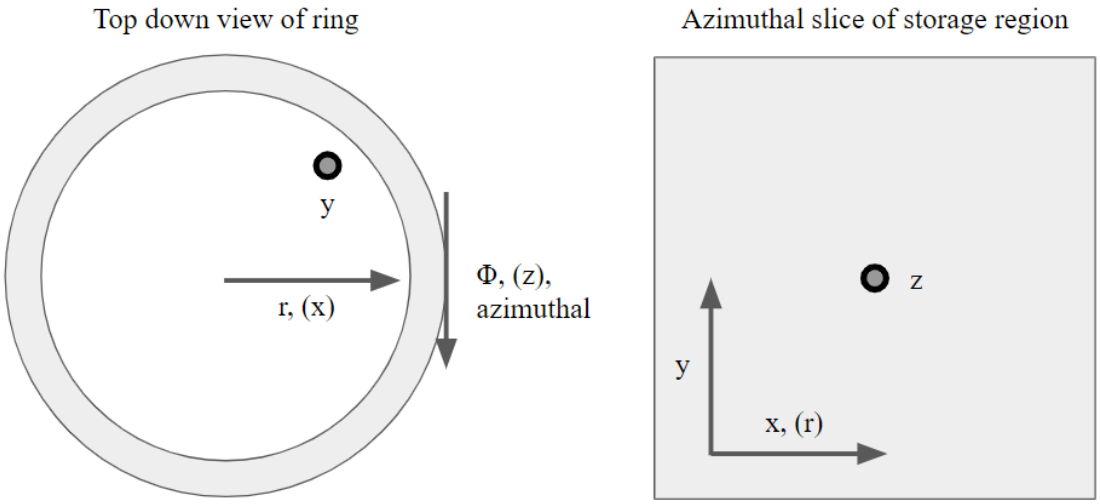

Figure 3.4: The two coordinate systems used in this document. Left: The top down view of the ring in cylindrical coordinates. Right: A view of an azimuthal slice of the ring in Cartesian coordinates.

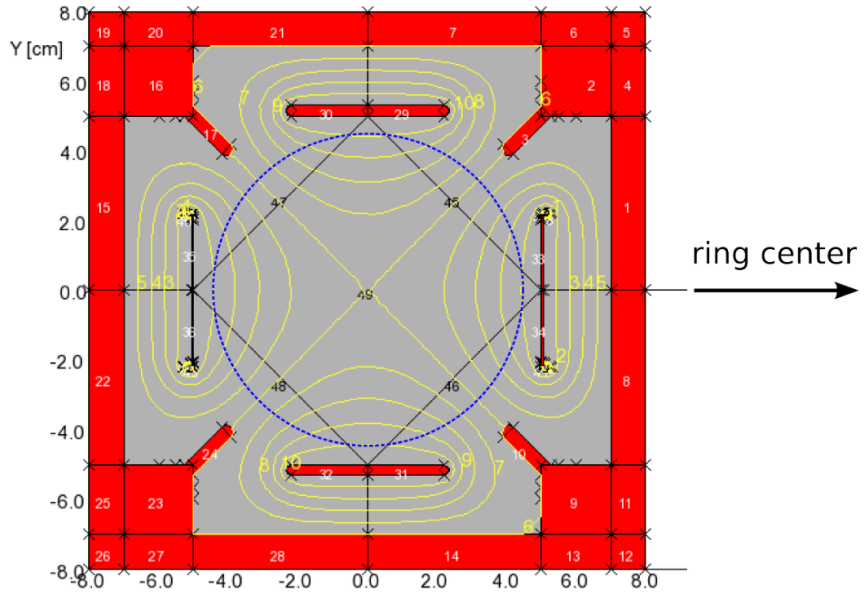

Figure 3.5: A cross section of the muon storage region showing the electrostatic quadrupoles, from quad stations Q2, Q3, and Q4, reproduced from [40]. The yellow lines show the equipotential lines of the electric field and the blue circle shows the 9 cm diameter muon storage region. Quad station Q1 has a slightly different configuration to avoid blocking muon injection.

tical direction. They also cause defocusing radially, but this is counteracted by the magnetic force. The combination of the magnetic field and the electrostatic quadrupoles, the stored beam is contained both radially and vertically.

Ideally, the vertical focusing would be present constantly around the ring corresponding to a constant electric quadrupole as a function of azimuth (this is actually a common approximation, the "continuous quad" approximation). However, this ideal setup would require the high voltage plates to be continuous around the ring, which is impractical for technical reasons. The quads are instead broken up into four stations the each consist of a long set of plates and a short set of plates. Overall, the electrodes occupy 43% of the total azimuth and maintain four fold symmetry around the ring.

3.2.4 Beam Injection and the Inflector Magnet

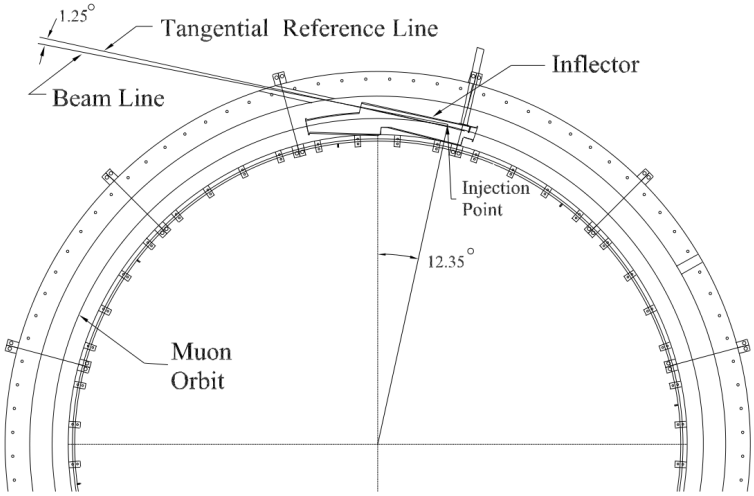

Figure 3.6: The inflector magnet allows the muon beam to pass through the storage ring yokes without being deflected and lost. The muons are not directly injected onto the ideal orbit, and require correction down stream by the kicker magnet.

Muons are injected into the g-2 storage ring in discrete groups called *fills*. In order to pass into the storage rings, muons must travel through the magnet yoke and the associated field. In order to prevent this field from deflecting the incoming muons, an inflector magnet is used to cancel the main 1.5 T field in the pass through. The inflector magnet must minimally distort the magnetic field in the storage region. The solution is to use a superconducting magnet in the pass-through that cancels the 1.5 T field, but has low edge fields. The muon beam is able to pass un-deflected into the storage region, almost tangentially to the ideal orbit, without ruining the precision magnetic field on the ideal orbit.

3.2.5 The Muon Kicker

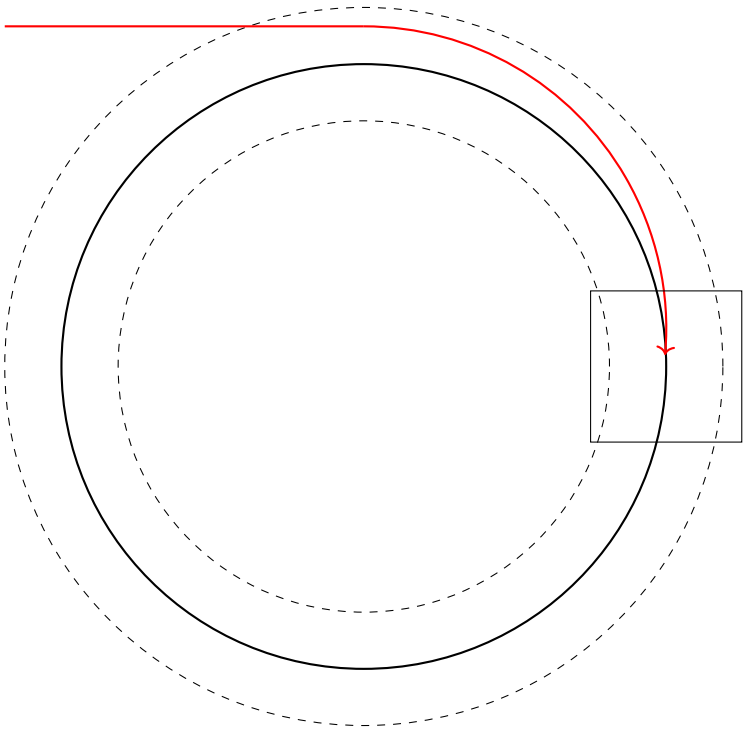

Figure 3.7: A diagram of the kicker magnet. The kicker (the square) provides an impulse that redirects the muon momentum along the ideal orbit (black) when they cross over the ideal orbit from injection (red).

As the muons exit the inflector and enter the storage region, they are displaced outwards radially 7.7 cm from the ideal orbit. However, the acceptance regions of the storage region is only 4.5 cm. The fast kicker is a pulsed magnet that provides an impulse to push the muons onto the ideal orbit. The kicker fires as the muons cross the ideal orbit, and redirects their momentum to be in a sustainable closed orbit. Ideally, the kick is fast enough that the muons only experience the field on their first trip through the kicker region and any tails to the magnetic field are negligible after 20 μs [40].

3.3 Measuring the Anomaly Frequency

The measurement of ω_a is accomplished by measuring the projection of the muons spin along their momentum as a function of time, per fill. The muons' spin state is detected indirectly by the momentum of the decay positrons, possible due to the parity-violation of the weak force. The decay positron momentum is integrated over many muon lifetimes per fill, and over many fills, and is then analyzed to extract the precession rate of the muon spin relative to its momentum.

3.3.1 Muon Decay and Parity Violation

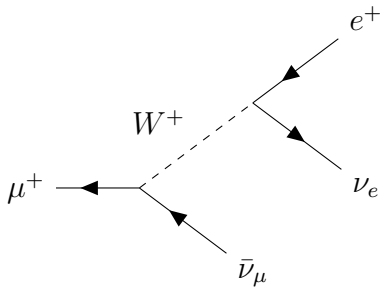

Figure 3.8: The dominant muon decay channel.

The dominant muon decay mode $\mu^+ \to e^+\nu_e\bar{\nu}_\mu$ (see Figure 3.8) is mediated by the weak force. The weak interaction violates parity symmetry, so this decay has a non-zero correlation between the spin of the muon and the momentum of the decay positron. Consider the muon in its rest frame with spin oriented to the right, as in Figure 3.9. The highest momentum decay positron will correspond to the emission of both decay neutrinos opposite it. Because the weak force only interacts with left-handed particles and right-handed anti-particles and the neutrinos are effectively massless, any neutrinos emitted along the same axis will have opposite spins. To conserve angular momentum, this means that the decay positron's spin will be in the same direction as the muon's spin. Again because of the parity violation of the weak force, the preferred direction for the emission of the decay positrons will be along the spin of the muon, so that the resulting positron is emitted with right-handed helicity. This implies that, in the muon's rest frame, there is a correlation between the direction of the decay positron and the spin of the muon at the time of the decay. A measurement of the positron's energy and direction is correlated with the spin of the muon at the time of decay.

3.3.2 Calorimetry

In the muon rest frame, the highest energy decay positrons are emitted in the direction of the muon's spin. When boosted to the lab frame, the highest-energy decay positrons are emitted in the same direction as the muon's travel when the spin and momentum of the muon are aligned. Likewise, there is a lack of highest-energy decay positrons when the momentum and spin are anti-aligned. If one measures the number of highest-energy decay positrons as a function of time, there will be an oscillation that corresponds to the muon's spin precessing relative to its momentum. This precession is exactly the precession from Equation 2.7. A precise measurement of the modulation in the number of highest-energy decay positrons is a measurement of ω_a.

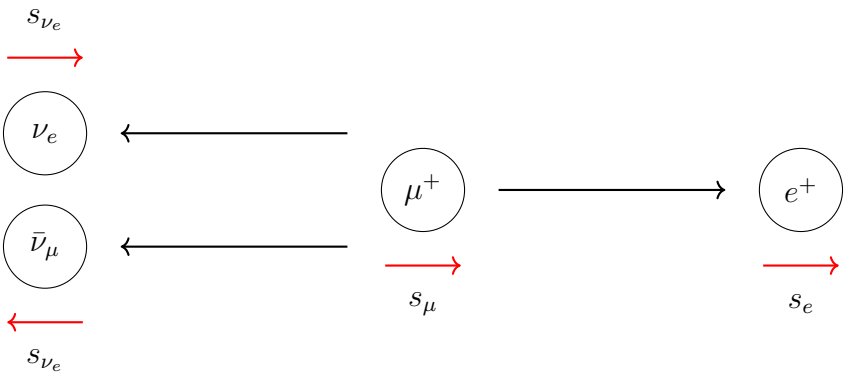

Figure 3.9: The preferred helicity for a decay positron is right-handed. Therefore, in order to conserve angular momentum, the highest momentum positrons (in the muon rest frame) must be emitted along the muon's spin.

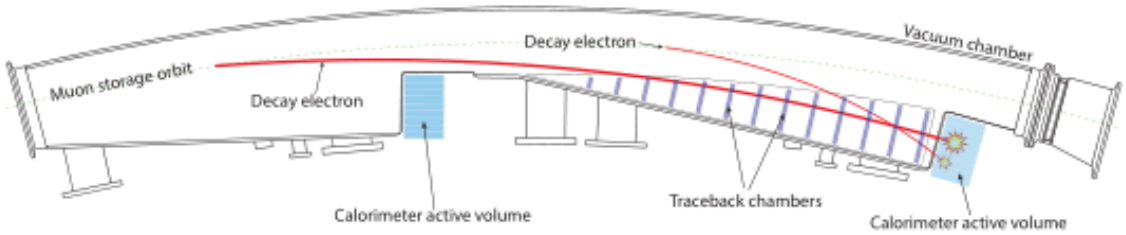

Figure 3.10: A top-down view of the calorimeter positions relative to the vacuum chamber and muon orbit, reproduced from [40]. The red lines show example decay positron paths that terminate at the calorimeter (light blue box). The "'traceback chambers"' are populated by the straw trackers, which are used the reconstruct the muon decay vertex and measure the beam profile.

When a muon decays, the decay positron is deflected inward by the magnetic field relative to the muon's path because it is lighter than the muon, as shown in Figure 3.10. There are 24 calorimeters positioned along the inner radius of the vacuum chamber to measure the decay positrons from the stored muon decays. The acceptance of the calorimeter array — the probability that a decay positron is detected — is about 80% for the highest-energy positrons that are used in the calculation of ω_a.

3.3.3 Anomaly Frequency Extraction

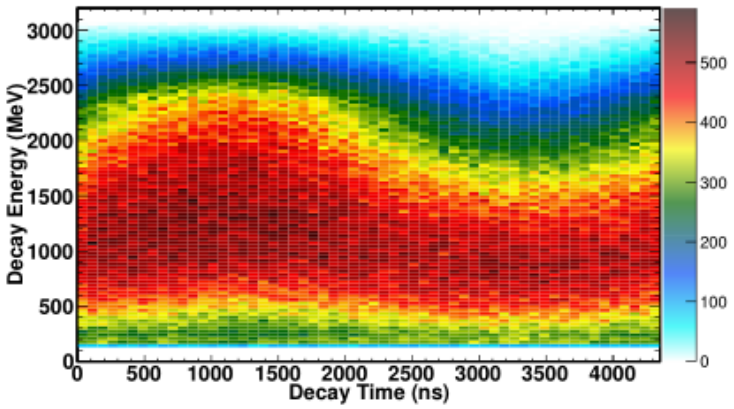

Figure 3.11: The decay positron spectrum as a function of time and decay energy, reproduced from [40]. The time is modulo a complete period of the anomaly frequency. One can see there is an abundance of higher energy positrons at time 1090 ns, corresponding to the muon spin and momentum being aligned, and a deficit at time 3270, corresponding to the muon spin and momentum being anti-aligned. Therefore, tracking the abundance of high energy decay positrons over time is a measurement of the frequency of dephasing between the muon spin and momentum — the anomaly frequency.

The data collected by the calorimeters include the time the positron is detected (relative to the initial muon injection), its energy, and where on the calorimeter it hit. A straightforward way to measure ω_a from the calorimeter data is to bin the detected positrons by decay time and energy over many fills. Because the highest-energy positrons carry information about the spin of the muons (see Figure 3.11), a cut is applied on positron energy such that only positrons with energy above the threshold are used in the analysis. The resulting histogram is high energy positron detections as a function of time. A general expression for the counts as a function of time is

$$N(t) = N_0 \exp(t/\tau) \left(1 + A \cos(\omega_a t + \phi)\right), \tag{3.6}$$

where N_0 is an overall normalization, τ is the muon lifetime in the lab frame, A is the

asymmetry in the muon decay, and ϕ is the initial phase of the oscillation. This function can be fit to the data, and the value of ω_a can be extracted.

3.4 Measuring the Muon Spatial Distribution

As the muons circle in the storage ring, they experience many external fields that are designed to keep them contained. The net effect of these fields fall under the category of "beam dynamics," which is the study of how the beam behaves as it travels around the ring. Many of these effects, such as the coherent betatron oscillations and pitch correction, are important to the final measurement of ω_a and are introduced as systematic corrections to the measurement described in Section 3.3. However, beam dynamics are combined the the time-dependent magnetic field map to calculate the average magnetic field, $\tilde{B}$, during the ω_a measurements.

3.4.1 Straw Trackers

The straw tracker system is used to measure the decay positions of the muons in the storage ring. The time averaged number of decay positrons coming from a unit volume in the ring is proportional to the time averaged number of muons in that same unit volume. Essentially, the number of positrons tracked back to a given voxel (volume element) is proportional to the likelihood of finding a muon in that voxel. This allows for a real-time, indirect measurement of the profile of the stored muon beam. A tracker station is an array of "straws" filled with gas that lives in the vacuum chamber, just before a calorimeter. As a decay positron travels through these straws, it ionizes the gas and is detected by charged wires in each straw. The location of each hit in each straw can be determined, which means that a positron's trajectory through the tracker station, before it hits the calorimeter, can be traced (see Figure 3.10). Using the trajectory and a map of the fringe magnetic field in the tracker region, the positron's path can be extrapolated backwards to determine where in the storage ring it originated. Collecting these positions over the full data set, the trackers can determine the beam profile.

There are two such tracker stations in the ring, at 180 deg and 270 deg. Each one can only sample the beam profile from a relatively narrow azimuthal window upstream of it, so the system only provides beam profile measurements from a single azimuthal position in the ring. These measurements can be combined with data from the calorimeters and simulations that use the electric and magnetic fields as inputs to approximate the muon distribution as a function of azimuth in the ring.

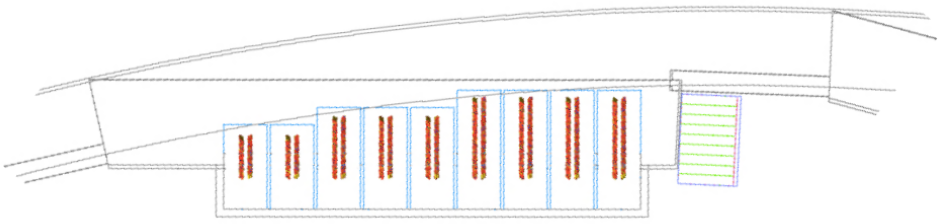

(a) Top-down view of the straw tracker placement in the vacuum chamber. The blue boxes outline the modules and the red lines represent the actual rows of straws.

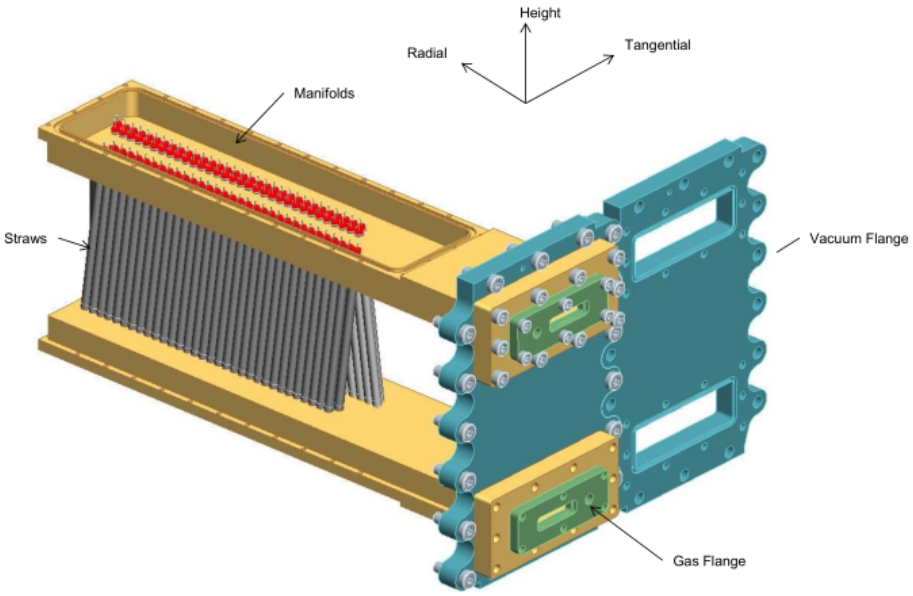

(b) A single straw tracker module.

Figure 3.12: The straw tracker system can trace the path of decay positrons and use them to reconstruct the muon decay vertex, providing an indirect measurement of the muon beam profile. Figures reproduced from [40].

3.4.2 Relationship to the Magnetic Field

The most important effects for the muon-weighted field average, $\tilde{B}$, are: the total number of muons per fill; the deviations of the center of the muon distribution from the ideal orbit, called the closed orbit distortion; and the 2D distribution of the muons as a function of azimuth, called the beam profile. All three of these are discussed more in depth in Chapter VII, but are presented here for sake of overview.

The first of these important effects is the distribution in time. This effect accounts for fills with more or fewer muons, and naturally takes into account times where there were no muons. It is measured by counting the total number of decay positrons detected within a unit time. This count is the CTAG count (Calorimeter TAGged count).

The second effect is the closed orbit distortion, which parameterizes how the center of the muon distribution deviates from the ideal radius. As the muons circulate for hundreds of turns, only effects that are coherent with the path length won't average into the 2D distribution. Therefore, it is convenient to think of the closed-orbit distortion as a Fourier series expansion of beam center radius as a function of azimuth

$$R(\theta) = R_0 + \sum_{n=1} A_n \cos(2\pi\theta + \theta_n). \tag{3.7}$$

In this expansion, R_0 is the ideal radius, set by the choices of the magnetic field strength and muon momentum. The higher-order terms make distortions around this ideal. For example, the first-order correction is a shift of the circular orbit in the $r - \theta$ plane and the second-order correction is the distortion of the circular orbit into an elliptical orbit. This obviously couples to the azimuthal magnetic field variations.

The third effect is the 2D beam profile. This is a snapshot of the beam in the $r - y$ plane at a given azimuthal position. This couples to the 2D map of the magnetic field at the same azimuthal position, and directly influences how important higher order gradients are in the determination of the average field. The beam profile is generally a function of azimuthal position.

3.5 Measuring the Field

A more in-depth discussion of the systems used to measure the magnetic field can be found in Chapter IV, and the analysis of the data gathered by these systems are the focus of this dissertation. This section provides a brief overview of those systems and the associated data analysis in order to lay out the big picture for the reader, before diving into the nuances of the field.

3.5.1 The Field Measurement Systems

This experiment uses NMR probes as the primary field measurement devices. NMR probes only measure the magnitude of the magnetic field, not its direction. Suppose, however, that the field is large and predominantly constant in a given direction, and that one was interested in measuring the local deviations. The magnitude of such a field is

$$B = \sqrt{(\mathbf{B}_0 + \boldsymbol{\delta}\mathbf{B})^2}, \tag{3.8}$$

where $\mathbf{B}_0$ is the constant portion of the field and $\boldsymbol{\delta}\mathbf{B}$ are the small deviations around it. Allow that $\mathbf{B}_0$ is directed in the y-direction. Then

$$B = \sqrt{B_0^2 + \delta B^2 + 2B_{0y}\delta B_y} \approx B_0 + \delta B_y. \tag{3.9}$$

$\mathbf{B}_0$ is much larger than the deviations $\boldsymbol{\delta}\mathbf{B}$, with $\frac{\delta B_y}{B_0} < 10^{-4}$, then one can drop the higher-order terms proportional to $\delta B/B_0$ with a relative error of less than 10^{-8}, and the result is that the NMR probes measure the large offset field plus the y-component of the deviations. This is important for two reasons. First, it can simplify later calculations to assume that the field is primarily oriented in the y direction and that B_y is equal to the measurements from the NMR probes. Second, and more importantly, it means that the analysis is largely insensitive to the radial and azimuthal components of the magnetic field.

There are two primary systems for measuring the magnetic field in the storage ring: the trolley and the fixed probes. A simple way to think about the two different systems is that the trolley measures the field densely in space but sparsely in time, while the fixed probes measure the field sparsely in space but densely in time. The trolley has an array of 17 fixed probes arranged in concentric circles. It physically lives in the vacuum chamber, and can be pulled around the ring in the storage region of the muons, taking measurements at thousands of azimuthal locations as it travels (hence, "densely in space"). However, because it blocks the muons' path, it must be withdrawn into a garage during production runs. So as not to conflict with achieving the statistical precision requirements, the trolley is run approximately once every three days ("sparsely in time").

The fixed probe system — an array of 378 NMR probes — serves to fill in the gaps in time between the trolley runs while muons are present in the ring. The fixed probes live in grooves on the outside of the vacuum chamber, close to the magnetic pole faces, not in the actual muon storage region. They are arranged into 72 stations, some with four probes and some with six, around the ring, roughly spaced at 5 degree intervals ("sparsely in space"). They continue to take measurements while muons are stored, with each probe taking a measurement approximately every 1.5 seconds ("densely in time"). Even though

they do not measure in the muon storage region and do not measure field gradients as well as the trolley due to higher field gradients near the pole faces, they still provide valuable information about the field the muons experience while in the storage region.

3.5.2 Measuring a Field Map

Data from the two probe systems must be combined to create a field map, the magnetic field as a function of time and space in the storage ring. The trolley runs essentially provide snapshots of the field map at single times. Without the fixed probe system, one could just interpolate the field between each trolley run. However, due to field drift, which tends to follow a diurnal cycle, such interpolation would lose accuracy quickly, requiring frequent trolley runs to stay relevant. The measurements from the fixed probes are used to inform the shape of the field interpolation between trolley runs. In very broad terms, the time-dependent field map is constructed by setting the field map equal to the trolley maps at the trolley run times, and then using the field drift measured by the fixed probes to predict the field the trolley would have measured if it was there constantly, forming "virtual trolley measurements" (VTMs). One can think of this process as synchronizing the fixed probe measurements to the trolley measurements.

The VTMs can only be made at each of the 72 fixed probe stations, with an azimuthal resolution much less than an actual trolley run. Therefore, they are unable to completely replace the need for trolley runs, as each fixed probe station will slowly drift out of calibration due to differential drift around the ring, and drift in higher-order gradients that cannot be estimated from the fixed probe measurements. From this point of view, each trolley run is a recalibration of the VTMs.

3.5.3 The Muon-Weighted Average

As explained in Section 3.1, the important number to calculate the anomalous magnetic moment is not the field map as a function of time and space, but the average field experienced by the muons while they are in the storage ring. This means we must estimate the muon-weighted average of the field map over time. The muon-weighted average is expressed as

$$\widetilde{\omega}'_p = \frac{\int\int \mathrm{d}\mathbf{r}\ \mathrm{d}t\ \omega'_p(\mathbf{r},t) \times \rho_\mu(\mathbf{r},t)}{\int\int \mathrm{d}\mathbf{r}\ \mathrm{d}t\ \rho_\mu(\mathbf{r},t)}. \tag{3.10}$$

and is discussed in detail in Chapter VII.

CHAPTER IV

Magnetic Field Measurement Systems

4.1 Magnetic Field Shimming

The magnetic field's spatial uniformity is adjusted by its shimming kit. The shimming kit is a set of hardware controls that change the magnetic field locally in an area, and is used to create a more uniform magnetic field around the ring. The shimming can be broken down into two categories: the active shims and passive shims. The active shims are the power supply feedback and surface correction coils, which are covered later. The passive shims all consist of ways to change the distribution of ferromagnetic material near the storage region. These shims cannot be adjusted in real time — they require the field to be off to safely change. Therefore, they are changed rarely, generally only at the beginning of production data runs. The most important shims are discussed below, in order from coarsest to finest control of the field, and are shown in Figure 4.1.

Top Hats The top hats are steel plates that rest on the top and bottom of each magnet yoke. There are two on each the top and bottom per yoke, giving each a 15° azimuthal extent. Spacers are used to adjust the distance between the top hat and the surface of the yoke. The larger the gap between the top hat and yoke, the more magnetic flux can escape from the magnet, reducing the dipole field in that region of azimuth.

Pole Pieces The pole pieces are placed in the gap of the yokes, and are used to focus the field into the vacuum chambers inserted between the pole pieces. Each pole is 10° wide, with three on both the top and bottom of each yoke. The width of the air gap between the top and bottom poles greatly affects the dipole strength in that region. The poles can be adjusted vertically by inserting spacers between them and the yoke. Additionally, by tightening the pole down onto different spacer sizes, the pole itself can be bowed lengthwise a small amount to help correct for non-uniformities in the pole faces.

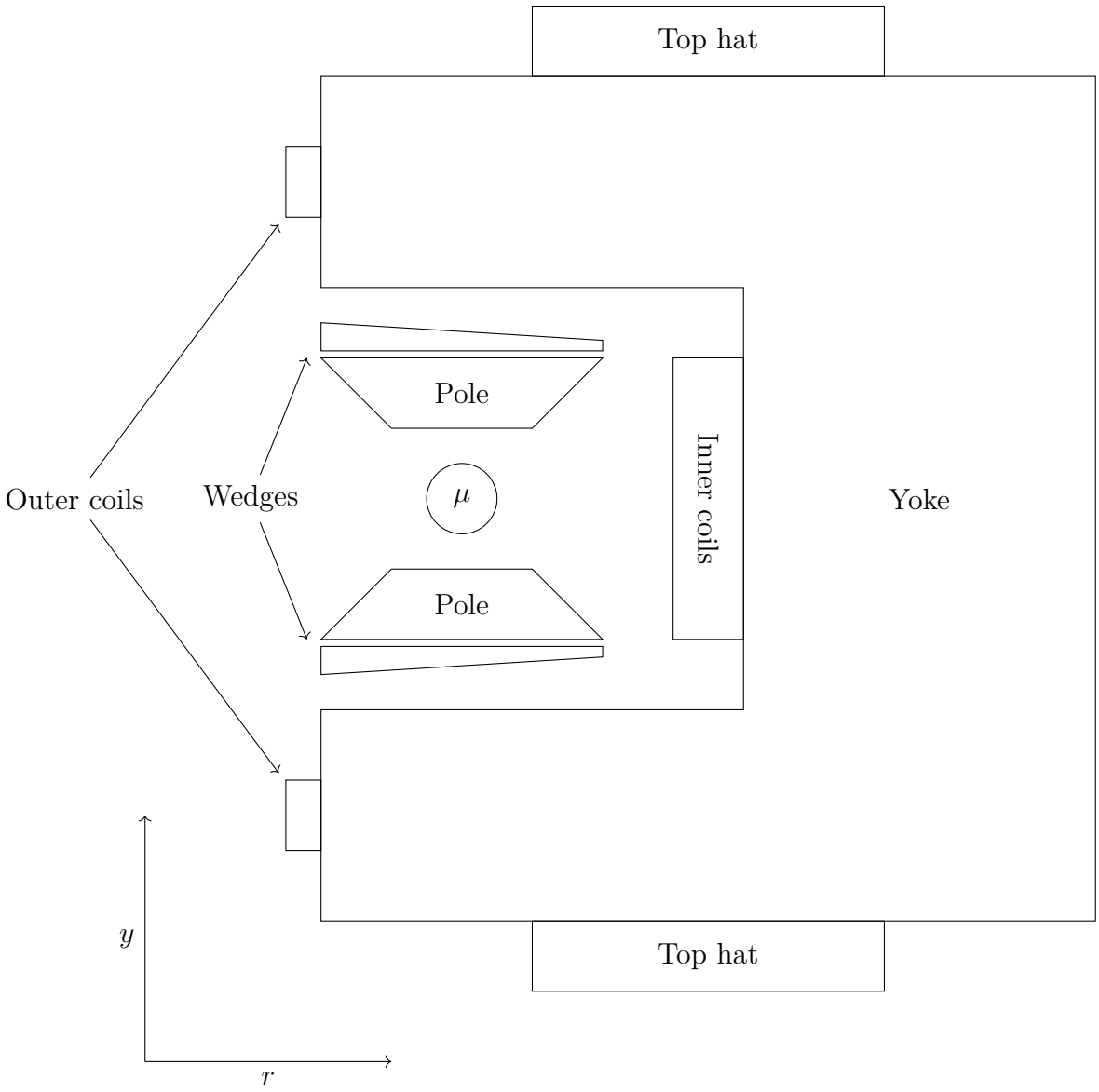

Figure 4.1: A cross section of the magnet (not to scale). The various components of the shimming kit are labeled, except the foil laminations that are applied directly to the face of the pole pieces.

Wedge Shims The wedge shims cover drastically less azimuth with 12 wedges per pole piece (864 wedges total, 0.83° each). They are shaped with more steel at lower radius, and can be slid in and out of the gap between the yokes and pole pieces. The further in the wedge is slid, the more magnetic material in the magnetic circuit, and the greater the field in that area. They are radially asymmetric to help offset the asymmetry of the yoke itself, which is open to air at lower radius, but have large amount of magnetic material at higher radius. This also gives the wedges some amount of control over the radial gradient of the field, and can be used to smooth its azimuthal variations.

Thin Foil Laminations The foil laminations are the finest control on the field. They consist of small strips of steel foil placed directly onto the pole surface and fixed with G10 fiberglass laminate [41]. They are placed every 0.24° on the top and bottom pole, at three radial locations. The three different radii allow for the shims to correct higher order radial gradients, like the normal quadrupole and sextupole. Each of the foils was individually weighed and selected for each position around the ring. Fixed probes are placed near the the foil laminations, and the local field gradients from the foil can reduce the T_2^* time of the probes, drastically reducing their precision. To address this, in locations near fixed probes, the foil strip are replaced by "picket fence" laminations, which have similar effects on the field but don't create problems with the fixed probe measurements [41].

4.2 The NMR Probes

The magnetic field in the storage ring is measured using pulsed NMR probes. The protons used for the measurement in the NMR probes, however, are not free. They are in hydrocarbons in petroleum jelly and are surrounded by the other materials of the probe. Each of these material effects causes a perturbation in the external field at the proton: there is diamagnetic shielding from the molecular structure of the hydrocarbons (the chemical shift), and there is the perturbations to the field from the magnetization of the material used to construct the probe. For each probe, then, the perturbations must be measured and corrected in order to get an accurate magnetic field measurement. The perturbations to the field are measured and corrected in the trolley NMR probes by calibration with the "plunging probe."

NMR probes measure the magnetic field by measuring the rate of precision of the proton magnetic moment in a magnetic field, as described in Chapter II. The protons are prepared by applying an RF pulse to the sample through a solenoid in each probe. This pulse takes spins that are aligned with the magnetic field and aligns them orthogonally to the field,

giving it the name a $\pi/2$ pulse. When the spins are orthogonal to the field, they precess. The changing magnetic flux this precession creates can be detected through the same coils used to create the $\pi/2$ pulse, now being used as a pickup coil. The resulting signal is called a *free induction decay* (FID).

The FID can be broadly thought of in two pieces: the carrier wave and the envelope. The carrier wave is at the frequency of the precession that is the measurement of the field strength. The envelope is a complicated function of the magnetic environment of the sample. In general, it is a decaying function, although it can have small rebounds as protons precessing at slightly different rates go in and out of phase with each other. The decay can be further broken into three effects with different time constants called T_1, T_2, and T_2^*. T_1 is the rate at which the spins realign with the external magnetic field, returning to their equilibrium distribution. It is important that T_1 be shorter than the time between sequential NMR measurements to allow the spins time to realign before being excited with another $\pi/2$ pulse. T_2 and T_2^* both relate to the decoherence of the spins as they precess. T_2^* is shorter than T_2, and includes decoherence caused by inhomogeneous magnetic field effects, whereas T_2 only includes the properties of the sample itself. T_2^* is the limiting factor in the analysis of the FID, as a short T_2^* causes a short FID with a low number of oscillations of the carrier wave. This manifests as a larger uncertainty on the extracted frequency and a higher shot-to-shot variations from the NMR probe.

4.3 Calibration Chain

The precision field measurement requires careful calibration of all of its pieces. A calibration chain through several systems accomplishes this task. Each system is described in more detail below, but it is helpful to establish a big-picture view before going into details. The calibration is referenced back to a precise MRI magnet at Argonne National Labs. The plunging probe, a very precise NMR probe, is studied in the MRI magnet to determine the perturbations to its measurement, and to create an absolute reference. It is then moved into the storage ring at Fermilab, where it is moved by a translation stage in the storage region. The translation stage lets it move into the storage region of the storage ring and sample different points, while retracting during normal operation.

The plunging probe is used to calibrate each of the 17 trolley NMR probes. While the trolley is out of the way, the translation stage moves the plunging probe to the XY location of a trolley probe, and takes a measurement. The plunging probe is retracted and trolley then moves forward to position its probe in the same location. This is repeated for each of the 17 probes, transferring the plunging probe calibration from the plunging probe to the

trolley. During each trolley run, the calibrated trolley is used to measure the correlation between the field moments measured by the trolley and those measured by the fixed probes. This process is called "synchronization."

4.4 Absolute Calibration

The absolute calibration system consists of two primary parts: an NMR probe whose perturbations and material effects are very well know, called the absolute probe, and an NMR probe attached to a translation stage that can place its active volume in specific locations, called the plunging probe. There are two primary absolute probes based on different samples. The first is a water sample that used the magnetic moment of the protons in the water to measure the magnetic field. The other probe used the magnetic moment of the helium-3 nucleus to measure the magnetic field, using the same principles. The two separate absolute probes provide independent measurements of the field with different systematic effects, and can be used to cross-check each other. Both absolute probes are crafted with minimizing the perturbations to the measured frequency in mind. They are also characterized precisely to understand the remaining perturbations and to allow corrections on the measurement to calculate the true field to high precision [42].

The plunging probe is also stringently characterized and corrected. It is used to transfer the calibration from the absolute probe to each of the 17 trolley probes. It is attached to a translation stage that inserts in into the storage region at the x-y position of a given trolley probe. It takes a measurement, and then is backed out of the storage region while the trolley is moved up to position the given probe at the same azimuthal location to take a measurement. Then the trolley backs out and the plunging probe is reinserted. This procedure (called an ABA measurement) is repeated several times in order to correct for field drifts during the calibration procedure. Then the same ABA measurement procedure is used on the remaining 16 probes to find the calibration constants for each one relative to the plunging probe, shown in Table 4.1. The calibration program takes several days without muons, so it is only done between production data runs.

4.5 Trolley

The trolley is the primary system used for making field maps as a function of spacial coordinates. It is a self-contained unit that rides on rails inside the vacuum chamber, pulled by two lines to facilitate upstream and downstream motion. One of the cables is a nylon "fishing" line, but the other is the signal cable that carries power and the reference frequency

Trolley probe	Calibration relative to probe 1 (Hz)
1	0.00
2	-5.59
3	4.18
4	-1.84
5	2.62
6	15.17
7	29.25
8	-12.49
9	-5.87
10	-65.93
11	86.21
12	20.98
13	33.14
14	-12.36
15	-14.45
16	-69.84
17	80.06

Table 4.1: The calibration values for the trolley probes, relative to the center probe [43].

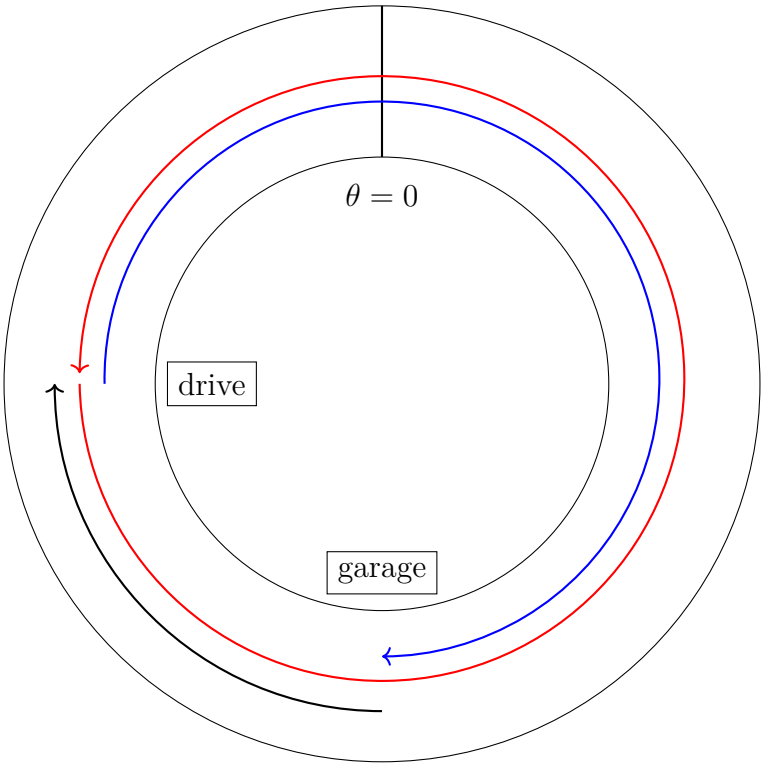

Figure 4.2: A top down view of the storage ring with the three steps of a standard trolley run. The first step is black (outer path), the second step is red (middle path), and the third step is blue (inner path). The second step is the step used for synchronization.

signal to the trolley, and provides a communication channel between the trolley microcontroller and the frontend computers. The cables pull the trolley around the ring during special trolley runs, during which there are no muons in the ring. A typical trolley run consists of three parts: a clockwise run downstream from the trolley garage to the trolley drive motors (about 90 deg), a counterclockwise run upstream from drive to drive (about 360 deg, includes some overlap to ensure closure), and a clockwise run from the drive back to the garage (about 270 deg). The trolley collects data from all three parts, but generally only the continuous data from the full cycle is used in the analysis.

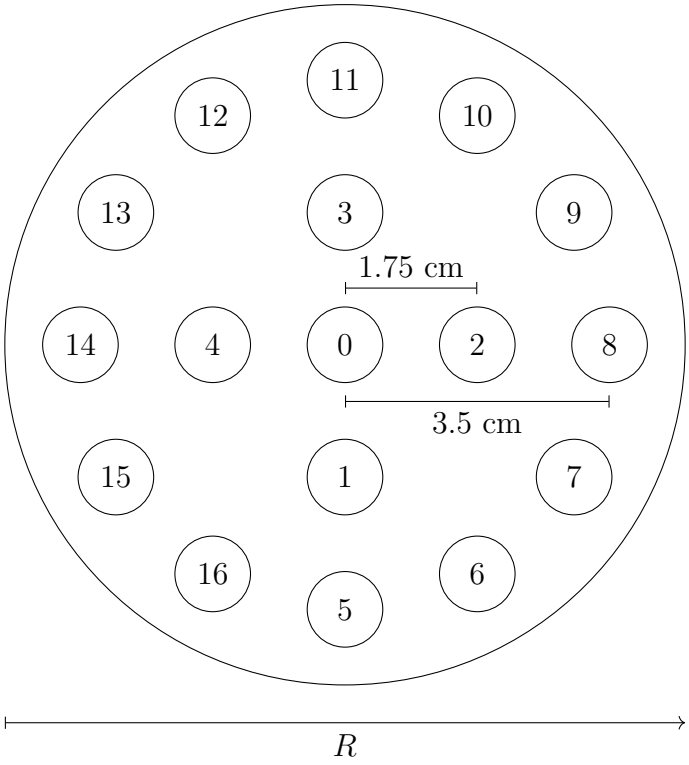

Figure 4.3: The trolley probe positions. The probe 0 is nominally on the muon ideal orbit.

The trolley collects data continuously while it is in operation. For the analysis, the most important data it collects are the field (frequency) measured by each of its 17 NMR probes, and its azimuthal position in the ring. The 17 probes are arranged in concentric circles, with one probe in the middle at nominally the muon ideal orbit, 4 probes at 1.75 cm radius, and 12 probes at 3.5 cm radius. The probes are read out sequentially, with the full measurement from all 17 probes taking just under a second to collect. This means that the trolley probes each take slightly more than one measurement per second, but they do so at different positions.

The trolley measures its azimuthal location in two ways. The simpler way is by using encoders on the drive motors to record how much the cables have been pulled. This method

creates a large uncertainty in the trolley position because of the elasticity and length of the cables. However, the trolley is also equipped with optical barcode readers. The bottom of the interior of the vacuum chamber is marked with two different barcodes: the absolute barcode and the reference barcode. The absolute barcode encodes positions every 20 cm and are used to locate the trolley in the ring, while the reference barcode has a mark every 2.5 mm and is used to interpolate positions between the absolute marks. The two azimuthal position measurements are combined, using the reliability of the encoder and the precision of the barcode to interpolate the trolley position at all times with an accuracy of 1 mm [44].

4.6 Fixed Probes

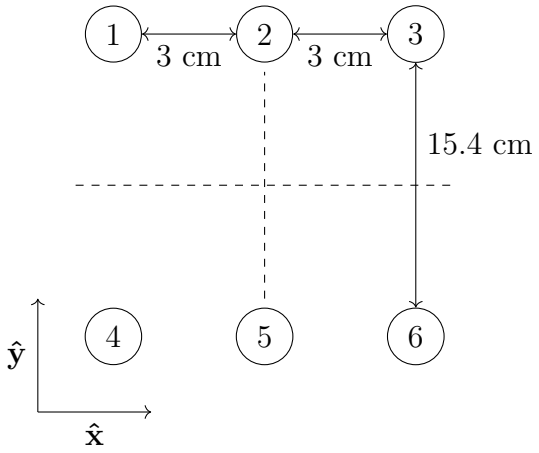

Figure 4.4: The standard geometry of a 6-probe station. In a standard 4-probe station, the probes numbered 1 and 4 are not present. There are non-standard 6-probes stations in the inflector chamber (stations 0-5) that have every probe shift radially inward by 1 cm, and non-standard 4-probe stations that are missing probes 1 and 6. See Chapter V for more details.

The fixed probe subsystem is an array of 378 NMR probes attached to the outside of the vacuum chambers. They are arranged into 72 stations of either 4 or 6 probes (see Figure 4.5 for a diagram of the stations' azimuthal distribution), evenly split between the top and bottom of the vacuum chamber. The probes are vertically displaced above and below the muons' ideal orbit by 7.7 cm. In most of the 6-probe stations, the probes are spread horizontally at $(-3\text{ cm}, 0\text{ cm}, 3\text{ cm})$ with respect to the muon ideal orbit, while most of the 4-probe stations are at $(0\text{ cm}, 3\text{ cm})$. Note that the 4-probe stations are not centered on the ideal orbit. There are six 6-probe stations, located near the inflector where muons enter the storage ring that are displaced 1 cm inward to $(-4\text{ cm}, -1\text{ cm}, 2\text{ cm})$. There are also three 4-probe stations where the top and bottom probes are not symmetric; the top

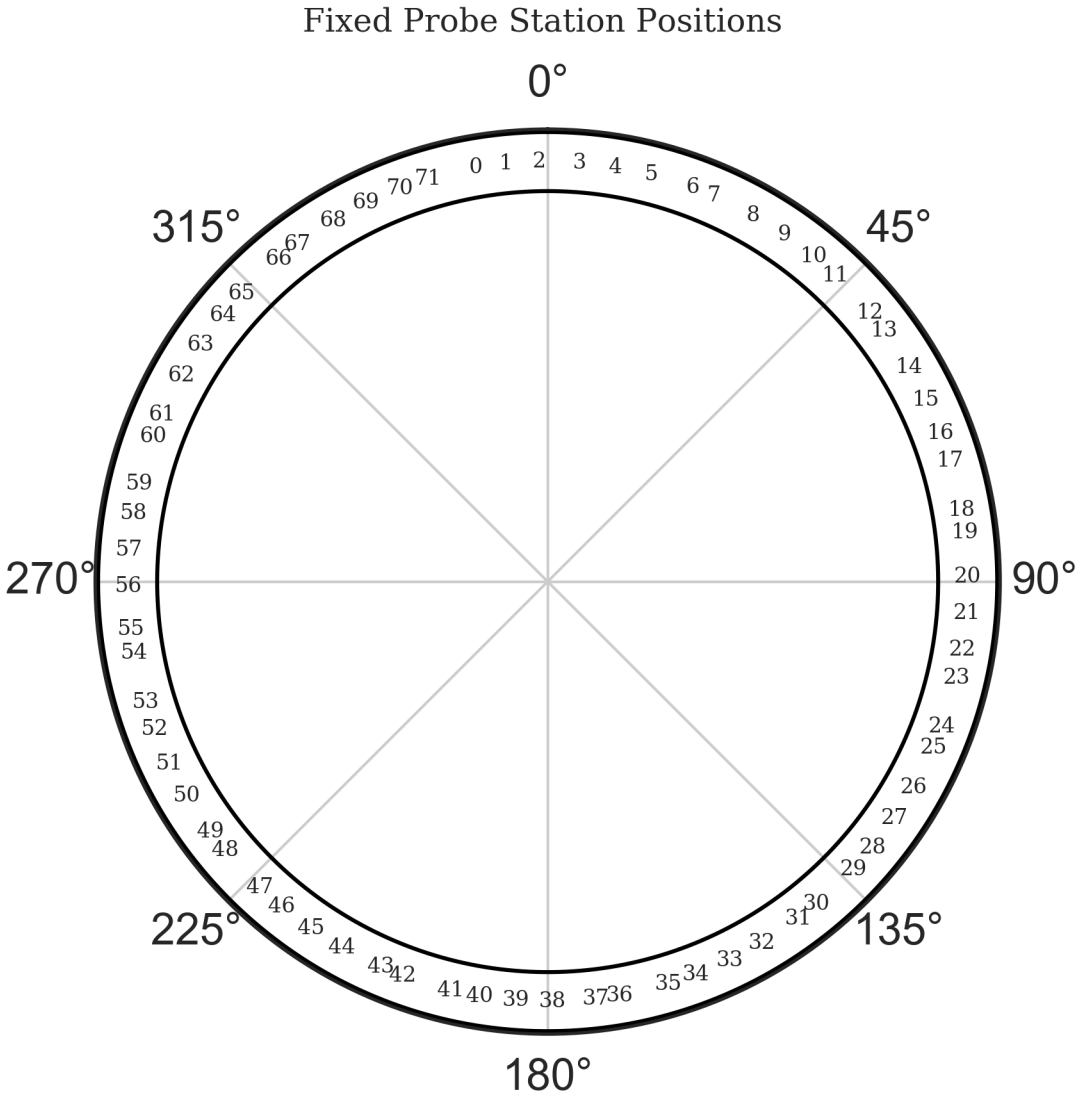

Figure 4.5: The azimuthal locations of the fixed probe stations, labeled by station number.

probes are at (0 cm, 3 cm) and the bottom probes are at (−3 cm, 0 cm).

Because the fixed probes are closer to the magnet's pole faces and the foil lamination shims, they experience higher field gradients than the trolley probes. This could cause some probes to be unreadable, with T_2^* times shorter than can be analyzed, which would make them them useless. An attempt was made during the shimming process to reduce the gradients caused by the laminations at the fixed probes by using a "picket fence" lamination near the fixed probes. This worked very well, but for three stations near the inflector (stations 1, 3, and 5), the picket fence was not properly aligned with the vacuum chamber. This misalignment causes the FIDs from the probes in those stations to be significantly shorter and the frequency extraction to be significantly noisier, but ultimately still readable when averaged over long times and many FIDs.

Also of special note is station 54. This station is located near the trolley drive, and is where the trolley starts and ends its full 360 deg runs. Even though there is overlap between the beginning and end of the trolley run, meaning that the trolley run covers the whole ring, the full extent of the station (the extent is defined by the halfway points to the nearest neighboring stations, about 5 deg of azimuth total) is not double-covered, meaning that the full station coverage is split between the beginning and end of the trolley run, separated in time by about an hour. As explained in Chapter VI, this separation requires special consideration during analysis, because, as opposed to other stations where the trolley covers the full extent in about 40 seconds, the long time to cover all of station 54 means that field drift over time becomes non-negligible.

4.7 Power Supply Feedback and Surface Correction Coils

The power supply feedback (PSFB) and surface correction coils (SCC) subsystems are active subsystems. Both supply currents to coils to create small corrections to the magnetic field. The PSFB changes the current in the main, superconducting magnet coils by small amounts to change the average (dipole) field. The SCC controls currents in 200 individual loops attached to the top and bottom pole faces (100 per face) to control the azimuthal average of the gradients of the field. The SCC can also correct the average radial field, which is useful for vertically centering the muons. The fixed probe system feeds back on the PSFB continually to combat global field drifts caused by environmental changes, but the SCC does not experience feedback because there is no continuously-monitoring system that can currently provide the level of precision necessary for feedback on the SCC settings. Instead, the SCCs are set to minimize the azimuthal average of the higher order moments.

4.8 Fluxgate Magnetometers

The fluxgate magnetometers are the only routinely-used non-NMR magnetometers. A fluxgate works by using the saturation experienced by ferromagnetic materials in an external magnetic field. A core of magnetic material is wrapped with two coils. One coil drives an alternating current in the core and the second picks up the resulting changing magnetic flux in the core. An external field offsets the AC field driven by the first coil causing saturation that is different for the positive and negative phases of the AC cycle. The voltage across the second coil is proportional to the rate of change of the core magnetization, which is zero when the core is saturated. By comparing the waveforms of the first and second coils, it is possible to calculate when the core reached saturation and therefore what the external magnetic field is. This also explains the main limitation of fluxgates: if the external field is too large, then the core will always be saturated, regardless of the alternating current. Therefore, fluxgates can only be used in low-field environment. The fluxgates used for this experiment have a maximum range of ± 10 Gauss, which prevents them from getting too close to the magnet. Instead, they live just outside the 5 G line, the region where the magnetic field is under 5 Gauss.

Despite this limitation, fluxgates have some distinct advantages over NMR probes for measuring magnetic fields. Most notably, a single fluxgate is most sensitive to the external field component aligned with its core's axis. By placing three of the cores mentioned above into one device, all mutually orthogonal, the fluxgate can measure all three components of the field, as opposed to NMR probes that can only measure the magnitude of the field. Fluxgates also have a larger bandwidth than NMR probes; whereas the NMR probes in this experiment only take a measurement approximately every one second, the fluxgates can take over 1000 samples per second. This makes the fluxgates sensitive to faster time-dependent transient such as the 60 Hz noise from the electronics, and to shorter duration transients. These two advantages make the fluxgates very useful for identifying sources of external field transients.

There were four Bartington Mag690-1000 fluxgates (see Figure 4.6 for reference picture) in use during Run 1. An additional four fluxgate magnetometers were installed before Run 2 in August 2018. They were positioned on the concrete floor beneath the false-floor in the center of the magnet, approximately 2 m towards the center of the ring from the storage region and positioned at roughly $\phi = 0,\ 90,\ 180,\ 270\,\text{deg}$ in azimuth, as shown in Figure 4.9.

The fluxgates are instrumented to a custom power supply/conditioning unit (PS/CU) that provides power and filters the signal from the fluxgates. The input is passed through a Sallen-Key low pass filter [45] with a roll-off frequency at 2.3 kHz (corresponding to a Nyquist

Figure 4.6: A Bartington Mag690-1000 fluxgate used in the experiment. Sharpie for scale.

frequency of 1.2 kHz). This frequency was chosen to align with the fluxgate's bandwidth of DC to >1kHz. The PS/CU also includes options for AC coupling the signals with high gain to observe higher frequency transients. The AC coupling is a Sallen-Key high pass filter with a roll-off frequency at 1.1 Hz. This frequency was chosen to remove the large (order 1 V) DC offsets from the fluxgate signal without attenuating the signals of interest, particularly at 60 Hz. See Figure 4.7 for the schematic and Figure 4.8 for the board layout of each circuit board. Each board supports two of the three-axis fluxgates and outputs 6 channels per fluxgate, a DC and an AC coupled signal for each of the three axes. The AC channels can have higher gain to increase the dynamic range for higher-frequency signals. The conditioned signals are digitized by a National Instruments PCIe-6259 ADC, with 32 AI channels with 16 bit resolution.

Not every channel is digitized. All the DC coupled channels are digitized, but only the y-axis (corresponding to the axis of the ring, vertically) AC coupled channel is saved. For each channel, data is acquired in 15 second events. For each event, two waveforms are saved. The first is a binned-and-averaged waveform with 1 second bins, to track the slow, DC behavior of the fluxgate. The second is an FFT in steps of 1 Hz from DC up to 1 kHz. This waveform is used to track the faster transients over time.

The analysis of the fluxgate data is largely done by eye. The digitized waveforms and their Fourier transforms can be monitored in close-to-real time as well as in later analysis. This allows for studies where other systems, such as the cryogenics or ring monitoring systems, are changed to observe the effect on the magnetic environment of the ring. One such program was performed in 2015 when both the fluxgates and the fixed probe systems detected a transient with a period of four minutes and an amplitude on the order of mG (10^{-7} T, about 100 ppb) in the ring (see Figure 4.10). The period and duty cycle closely matched the acquisition

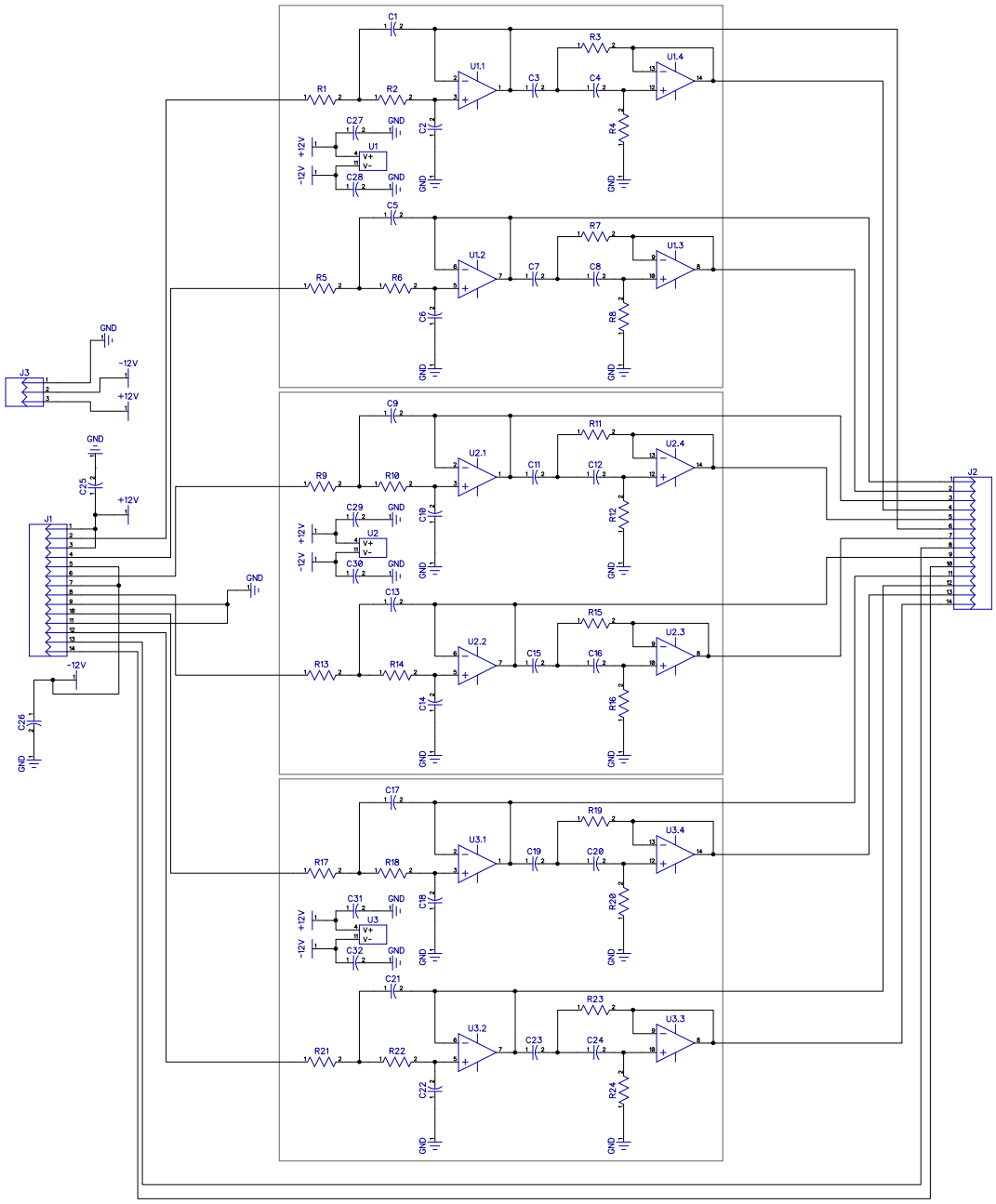

Figure 4.7: The circuit diagram for the fluxgate power supply and conditioning unit. Each board (shown) supports two fluxgates with 3 channels each. The boxed areas represent a single quad op amp IC.

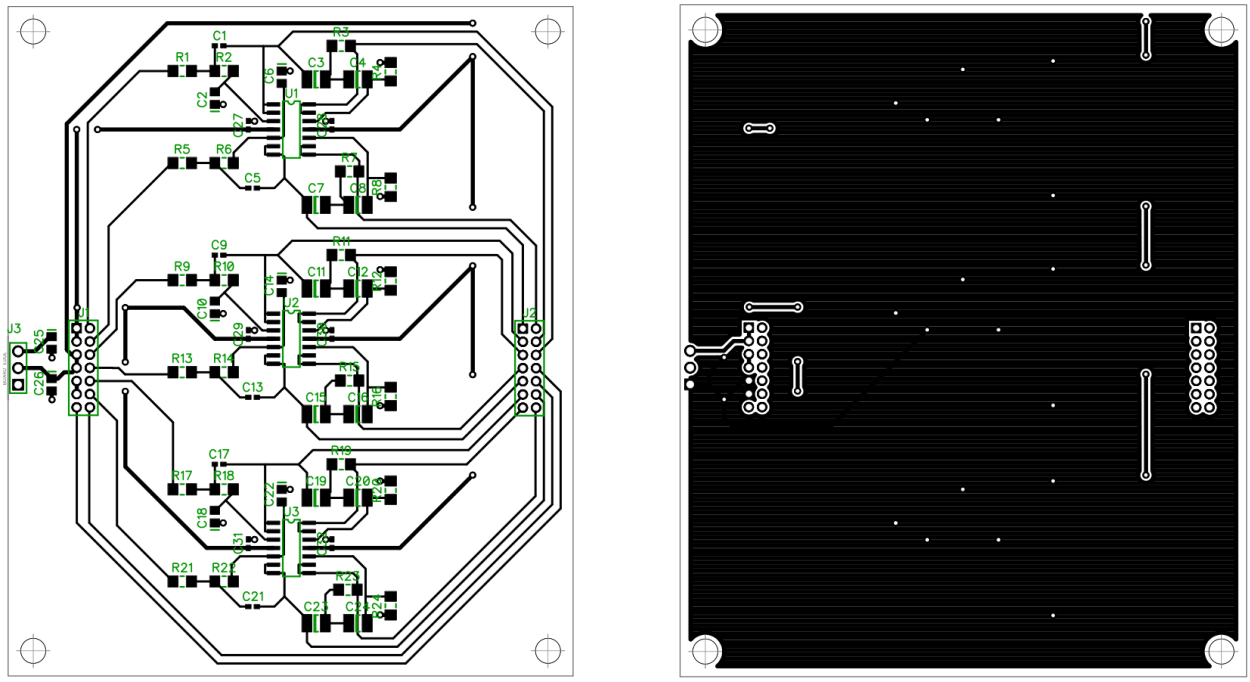

Figure 4.8: The circuit board for the fluxgate power supply and conditioning unit — top layer left, bottom layer right. Each board (shown) supports two fluxgates with 3 channels each.

rate for strain gauges that monitor forces on the coils. The strain gauges were changed to a three minute cycle, and the period detected by the fluxgate changed correspondingly. We started a program of turning off banks of strain gauges and monitoring the field detected by the fluxgates in real time. Doing so, were were able to isolate the strain gauges that were malfunctioning and creating the transient field so they could be fixed.

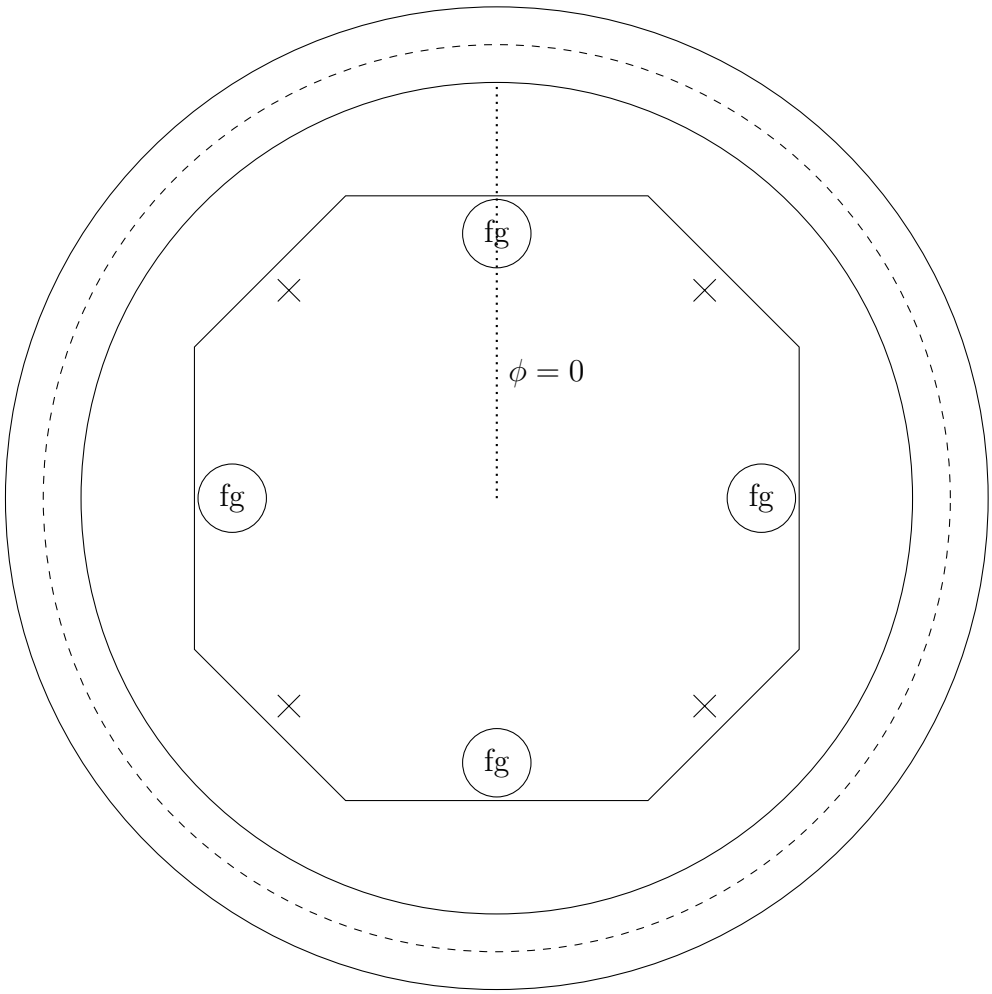

Figure 4.9: A top-down schematic of the positions of the fluxgates in the ring in Run 1. The Xs show where the additional fluxgates were added to the ring in Run 2.

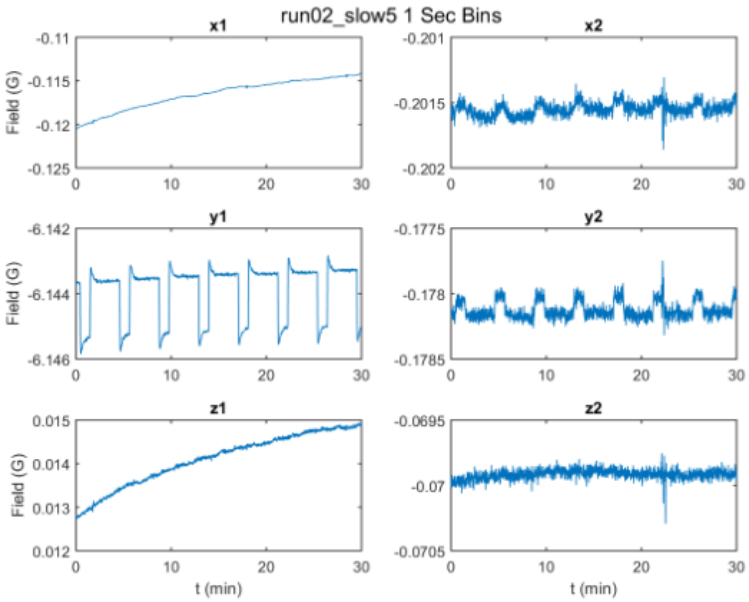

Figure 4.10: A July 2015 study with the fluxgates found a periodic signal of $T = 4$ min in the ring. This study demonstrated their ability to track down sources of stray fields.

CHAPTER V

Moments of the Magnetic Field

The raw field data from the trolley and fixed probes are sets of field data at known positions in the X-Y plane of an azimuthal slice. Therefore, we can measure the spatial dependence of the field in 2D slices. A simple, powerful way to do this is to consider *moments* of the field. The moments are an equivalent basis that encodes the spatial distribution of the field. They can also be thought of as the derivatives of the field. This chapter introduces two basis sets of field moments, the multipole moments for the trolley geometry and the Cartesian moments for the fixed probe geometries, and the relationship between the sets of moments.

5.1 Definition of Field Moments

The 2D multipole moments arise as solutions to the Laplace equation in cylindrical coordinates, assuming no dependence on the z-axis. Assume a magnetic scalar potential $V(r, \theta)$ that does not depend on the z coordinate. In this case, we are considering a single slice of azimuth. Note that, in this case, the r coordinate is not the radial coordinate of the storage ring, but the radial displacement from the muon ideal orbit. Likewise, θ is the polar coordinate about the ideal orbit. Laplace's equation for this potential is

$$\frac{1}{r}\frac{\partial}{\partial r}\left(r\frac{\partial V}{\partial r}\right) + \frac{1}{r^2}\frac{\partial^2 V}{\partial \theta^2} = 0. \tag{5.1}$$

One must consider three constraints on the solution to this equation: first, the solution must be well-defined at $r = 0$ to be physical; second, constant offsets do not matter in the potential; and third, the solution must be periodic in theta. The general solution that satisfies these restrictions is

$$V(r, \theta) = c\theta + \sum_{n=1} r^n (a_n \cos(n\theta) + b_n \sin(n\theta)). \tag{5.2}$$

The magnetic field is defined as the gradient of the scalar potential. In polar coordinates, they are

$$B_r = -\frac{\partial V}{\partial r} \quad = -\sum_{n=1} n r^{n-1}(a_n \cos(n\theta) + b_n \sin(n\theta)) \tag{5.3}$$

$$B_\theta = -\frac{1}{r}\frac{\partial V}{\partial \theta} \quad = -\tfrac{c}{r} - \sum_{n=1} n r^{n-1}(-a_n \sin(n\theta) + b_n \cos(n\theta)). \tag{5.4}$$

c must be zero in order for the field to be well-defined at the origin. It is convenient at this point to calculate the field components along the x and y directions (radial and vertical in the storage ring basis). The final results for the field components are

$$B_y \quad = A_0 + \sum_{n=1} \left(\tfrac{r}{r_0}\right)^n (A_n \cos(n\theta) + B_n \sin(n\theta)) \tag{5.5}$$

$$B_x \quad = -B_0 + \sum_{n=1} \left(\tfrac{r}{r_0}\right)^n (A_n \sin(n\theta) - B_n \cos(n\theta)) \tag{5.6}$$

where we have taken the liberty of introducing a radial normalization term (4.5 cm for E989) and absorbing constants into the A_n and B_n parameters, called the "multipole strengths." The A_n parameters are called the *normal* multipole strengths and the B_n parameters are the *skew* multipole strengths. These are often written as "normal/skew (2n+2)-pole," like the "normal 2-pole (dipole)," "skew 6-pole (sextupole)," or "skew 14-pole." See Figure 5.1 for visualizations of the first several multipole moments.

5.1.1 Measuring Multipole Moments

Because the NMR probes used to make field measurements only measure the scalar field and the deviations in the field ride on a large offset field in the y-direction, the NMR probes predominantly measure only the B_y component, shown in Figure 5.2.

$$B_y = A_0 + \sum_{n=1} \left(\frac{r}{r_0}\right)^n (A_n \cos(n\theta) + B_n \sin(n\theta)) \tag{5.7}$$

All of the probes are mixed down with a 61.74 MHz reference signal (the field is nominally 61.79 MHz), meaning the the readout frequency is about 50 kHz for each probe. The relatively small variations around this value can then be fit to the multipole expansion, essentially causing a change of basis from the probe basis to the multipole moment basis. This procedure is especially well suited to measurements made by the trolley where the NMR probes are arranged optimally to measured the radial and angular dependence of the field in

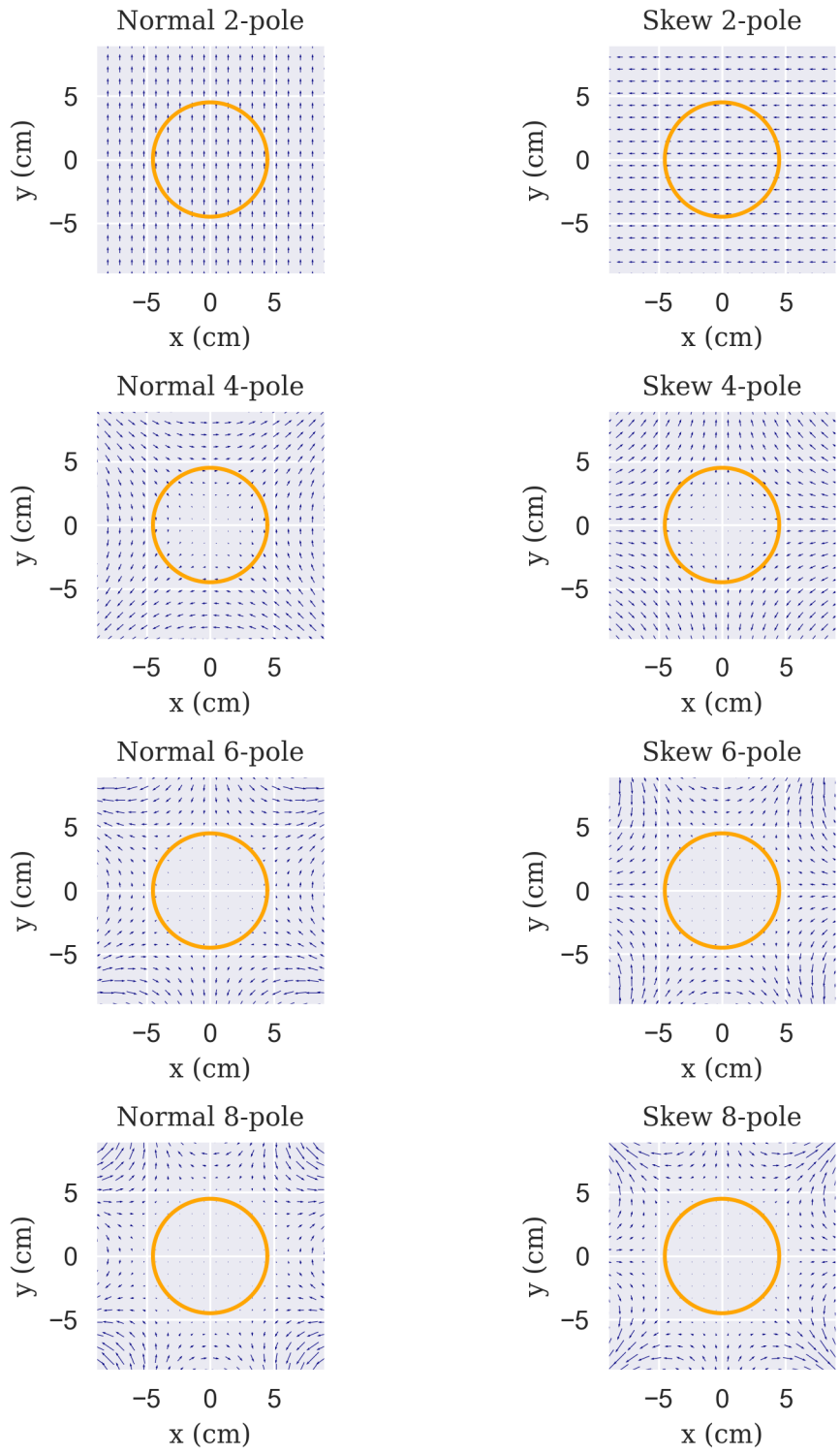

Figure 5.1: The first four multipole moments, both normal and skew (arbitrary units).

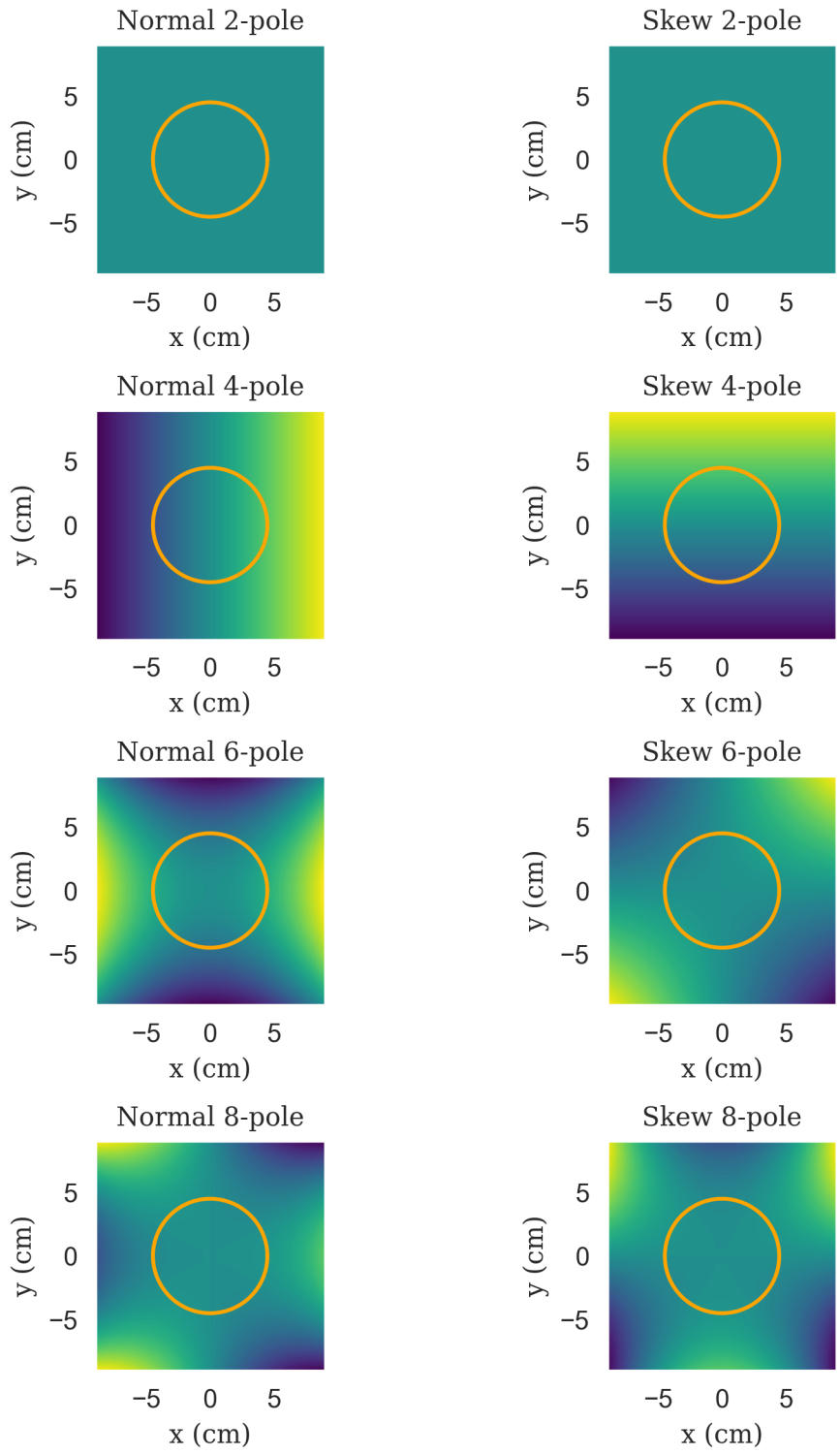

Figure 5.2: The B_y component of first four multipole moments, both normal and skew (arbitrary units).

an azimuthal slice. The fixed probes are not well-arranged to measure in the 2D multipole moment basis, and require a different treatment.

A simple way to calculate the multipole strengths for a measurement consisting of a frequency from each of the trolley's 17 probes would be to simply fit the measurements to the analytic form for B_y above, with some cutoff on n. However, another way is realized by considering the set of trolley probe measurements and the set of multipole moments as two separate bases, and determining a change-of-basis matrix between the two. The change-of-basis matrix from the multipole basis to the probe basis is easy to determine — it simply requires the evaluation of Equation 5.7 at each probe's (r, θ) coordinate.

Because there are 17 trolley probes, a naive assumption would be that the trolley is sensitive to the first 17 multipoles. However, this is not true. Because the probes measure a discrete set of points, there is a spatial Nyquist frequency associated with the measurement. For the most part, this isn't an issue because the inner and outer rings of 4 and 12 probes respectively have different Nyquist frequencies (the 6-pole and the 14-pole are the Nyquist frequencies, respectively), and the r^n dependence of the moments means that moments with similar polar profiles can be distinguished by their radial profile. However, there are two distinct cases where this is not true. The first is the skew 14-pole, which has nodes at each of the 17 trolley probes, corresponding to a column of zeros in the moment-to-probe change-of-basis matrix. This makes it essentially invisible to the trolley, and therefore unable to be fit (see Figure 5.3). The second case involves the skew 10-pole and skew 18-pole. Both of these probes have the same profile in the outer ring of trolley probes; the skew 18-pole aliases over the Nyquist frequency to appear as the skew 10-pole. In other cases where this occurs — for example, the 16- and 12-pole — the inner set of probes can measure the moment as well, so the r dependence can be used to determine both component uniquely. However, in the case of the 10- and 18-pole, the inner probes are all at nodes for both multipoles (see Figure 5.4). In the change-of-basis matrix, this corresponds to two columns that are multiples of each other. Luckily, the issue occur at relatively high n moments and their contribution to the measurement of $\widetilde{\omega}_p$ are suppressed in importance by the small size and symmetry of the muon profile.

If the 17 by 17 moment-to-probe change-of-basis matrix had all linearly independent columns, calculating the probe-to-moment change-of-basis matrix would just involve inverting it. Due to the two issues outlined above, we instead define a 17 by 15 matrix that takes the first 15 *linearly independent* moments to the 17 trolley probes. The inverse change-of-basis matrix can then be calculated by taking the pseudoinverse. The pseudoinverse of a matrix is the matrix $A^\dagger$ that best fits $\vec{a} = A^\dagger \vec{b}$ given $A\vec{a} = \vec{b}$. In this respect, the change-of-basis is still a fit. However, doing it this way provides significant computation time improvements,

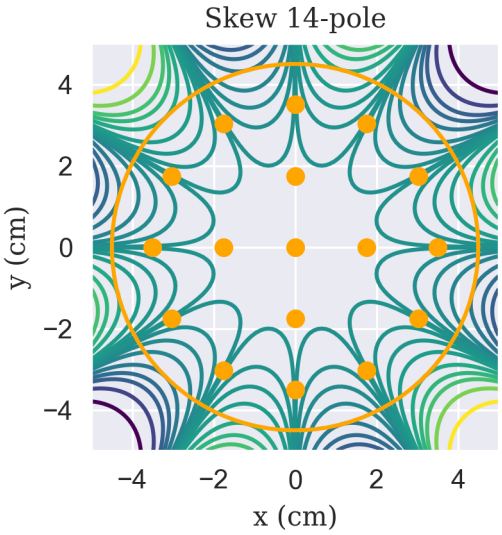

Figure 5.3: Every trolley probes sits at a node of the skew 14-pole, making it effectively invisible to the trolley.

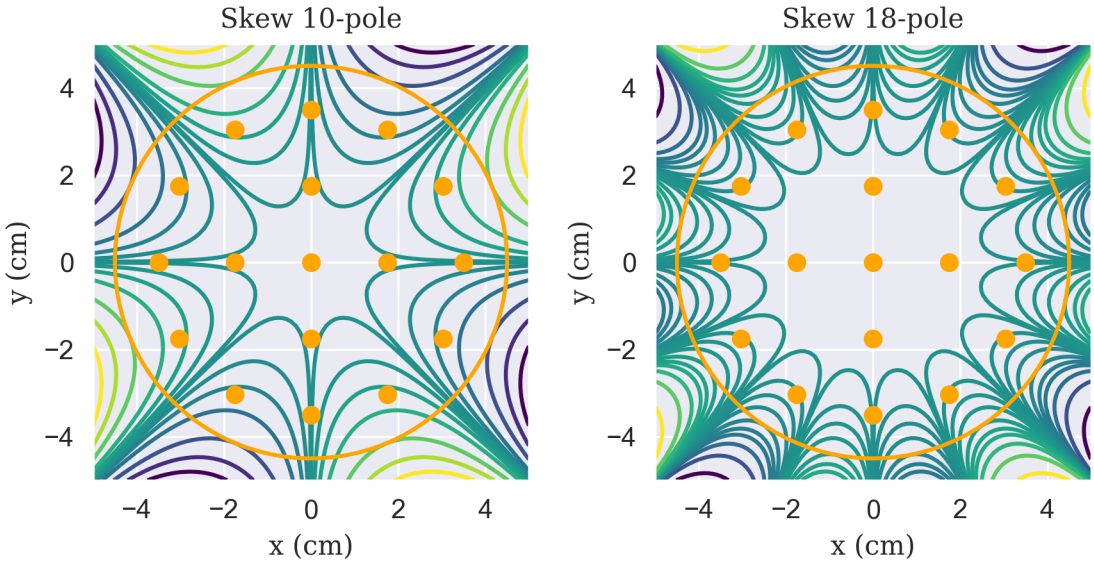

Figure 5.4: The inner five trolley probes sit at nodes of both the skew 10- and 18-poles. The outer rings measures a pattern with the same signature (zero, high, low, zero, high, low...). The two moments are indistinguishable to the trolley. Note: In the plot of the skew 18-pole, the multipole strength has the opposite sign of the skew 14-pole plot.

and standardization and transparency of the method, as well as respecting and highlighting the viewpoint that the probe measurements and multipole moments are just two different representations of the same physical object.

5.1.2 Cartesian Moments

The fixed probes are not arranged symmetrically in a polar coordinate system, but they do exhibit good symmetries in a Cartesian coordinate system. This is the inspiration for writing Cartesian field moments, which we will see are fairly analogous to the multipole moments. There are two equivalent ways of thinking about the Cartesian moments. They can be considered from the continuous perspective as the derivatives of the field, specifically as the x and y derivatives of B_y. Then one can use the fixed probes to make discrete estimates of the gradients. The moments can also be considered from the discrete perspective as just sum and difference modes of the fixed probes. Given the correct constants, these are identical treatments. Since the first method is easier to intuit physically, this treatment will follow it.

N		$r,\ \theta$	$x,\ y$
0	normal	A_0	A_0
1	normal	$A_1 \frac{r}{r_0} \cos(\theta)$	$A_1 \frac{1}{r_0} x$
1	skew	$B_1 \frac{r}{r_0} \sin(\theta)$	$B_1 \frac{1}{r_0} y$
2	normal	$A_2 \left(\frac{r}{r_0}\right)^2 \cos(2\theta)$	$A_2 \left(\frac{1}{r_0}\right)^2 (x^2 - y^2)$
2	skew	$B_2 \left(\frac{r}{r_0}\right)^2 \sin(2\theta)$	$2B_2 \left(\frac{1}{r_0}\right)^2 xy$
3	normal	$A_3 \left(\frac{r}{r_0}\right)^3 \cos(3\theta)$	$A_3 \left(\frac{1}{r_0}\right)^3 (x^3 - 3xy^2)$
3	skew	$B_3 \left(\frac{r}{r_0}\right)^3 \sin(3\theta)$	$B_3 \left(\frac{1}{r_0}\right)^3 y(3x^2 - y^2)$
...			

Table 5.1: The first several multipole moments written in Cartesian coordinates.

Consider Equation 5.7. It can be written as a function of x and y, instead of r and θ, by using the multiple angle formula and the relationships $x = r\cos(\theta)$ and $y = r\sin(\theta)$. The first several multipoles written in Cartesian coordinates, ignoring the skew dipole that

is unmeasurable due to only having a B_x component, are shown in Table 5.1. Written in terms of polynomials, it is easy to see that the Cartesian derivatives evaluated at $(0, 0)$ — the nominal center of the storage region — can recover the multipole strengths. Due to the geometry of the fixed probes at each station, only a few of the derivatives can be approximated. Table 5.2 shows the results of each of these derivatives evaluated at $(0, 0)$. Given the discrete positions of the fixed probes, it is possible to estimate the values for these derivatives at the center.

Derivative	Value @ $(0, 0)$	Note
B_y	A_0	
$\frac{\partial B_y}{\partial x}$	$\frac{A_1}{r_0}$	
$\frac{\partial B_y}{\partial y}$	$\frac{B_1}{r_0}$	
$\frac{\partial^2 B_y}{\partial x \partial y}$	$\frac{2B_2}{r_0^2}$	
$\frac{\partial^2 B_y}{\partial x^2}$	$\frac{2A_2}{r_0^2}$	6-probe stations only
$\frac{\partial^3 B_y}{\partial x^2 \partial y}$	$\frac{8B_3}{r_0^3}$	6-probe stations only

Table 5.2: The Cartesian derivatives measurable given the fixed probe geometry. Unless otherwise noted, both the 4- and 6-probe stations can measure these derivatives.

With the moments defined in both a convenient basis for the trolley measurements (the polar multipole moments) and a convenient basis for the fixed probe measurements (the Cartesian derivatives evaluated at $(0, 0)$), and the relationship between the two, it is convenient to define a vector of measured moments, $\mathbf{m}$. $\mathbf{m}$ has at most 17 elements in the trolley, and at most 6 (4) elements in a 6-probe (4-probe) station. In reality, we tend to only be concerned with the first 8 elements of $\mathbf{m}_{tr}$, and include the others to ensure proper fitting for the lower order moments. If we define the elements of each size vector well, then there will be a correspondence between the elements of each. The proper definition is shown in Table 5.3.

The full equations and resulting change-of-basis matrix for a standard 4-probe station, with the geometry seen in Figure 5.5, is worked out here. The change-of-basis matrices for the other geometries are listed, but not explicitly worked out. Note that the 4-probe station is not symmetric around $(0, 0)$. This requires a correction after the calculation to account for the shift to center. The first term, m_1 is already centered in this treatment, however.

	Name	Trolley	6-Probe Station	4-Probe Station
m_1	Dipole	A_0	$B_y\|_{\mathbf{0}}$	$B_y\|_{\mathbf{0}}$
m_2	Normal Quadrupole	A_1	$r_0 \left.\frac{\partial B_y}{\partial x}\right\|_{\mathbf{0}}$	$r_0 \left.\frac{\partial B_y}{\partial x}\right\|_{\mathbf{0}}$
m_3	Skew Quadrupole	B_1	$r_0 \left.\frac{\partial B_y}{\partial y}\right\|_{\mathbf{0}}$	$r_0 \left.\frac{\partial B_y}{\partial y}\right\|_{\mathbf{0}}$
m_4	Skew Sextupole	B_2	$\frac{r_0^2}{2} \left.\frac{\partial^2 B_y}{\partial x \partial y}\right\|_{\mathbf{0}}$	$\frac{r_0^2}{2} \left.\frac{\partial^2 B_y}{\partial x \partial y}\right\|_{\mathbf{0}}$
m_5	Normal Sextupole	A_2	$\frac{r_0^2}{2} \left.\frac{\partial^2 B_y}{\partial x^2}\right\|_{\mathbf{0}}$	
m_6	Skew Octupole	B_3	$\frac{r_0^3}{8} \left.\frac{\partial^3 B_y}{\partial x^2 \partial y}\right\|_{\mathbf{0}}$	
m_7	Normal Octupole	A_3		
m_8	Normal Decupole	A_4		
m_9	Skew Decupole	B_4		
m_{10}...	...			

Table 5.3: The moment ms, and their corresponding definitions for the trolley and both 4- and 6-probe stations. Note that the (normal, skew) pattern is reversed (skew, normal) $for n = 2,\ 3$, the sextupoles and octupoles. This switch takes into account the moments that are measurable by the fixed probe stations and preserves the mapping between different $\mathbf{m}$ vectors.

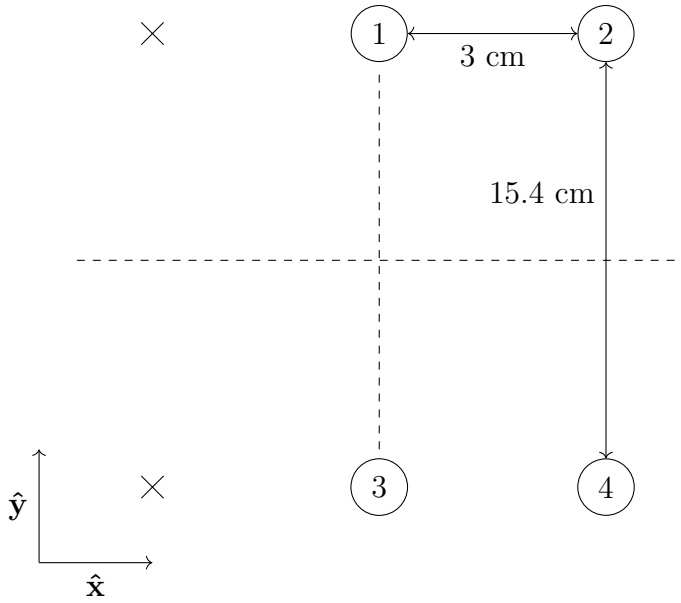

Figure 5.5: The geometry of a 4-probe station. Not drawn to scale.

$$m_1 = \frac{1}{2}(\omega_1 + \omega_2) \tag{5.8}$$

$$m_2 = \frac{1}{2}\left(\frac{\omega_2 - \omega_1}{3\text{ cm}} + \frac{\omega_4 - \omega_3}{3\text{ cm}}\right) \times 4.5\text{ cm} \tag{5.9}$$

$$m_3 = \frac{1}{2}\left(\frac{\omega_2 - \omega_4}{15.4\text{ cm}} + \frac{\omega_1 - \omega_3}{15.4\text{ cm}}\right) \times 4.5\text{ cm} \tag{5.10}$$

$$m_4 = \frac{1}{15.4\text{ cm}}\left(\frac{\omega_2 - \omega_1}{3\text{ cm}} - \frac{\omega_4 - \omega_3}{3\text{ cm}}\right) \times (4.5\text{ cm})^2 \tag{5.11}$$

$$\mathbf{m} = \boldsymbol{\Theta}\boldsymbol{\omega} \tag{5.12}$$

$$\boldsymbol{\Theta}_4 = \begin{pmatrix} 0.5 & 0 & 0.5 & 0 \\ -0.75 & 0.75 & -0.75 & 0.75 \\ 0.146 & 0.146 & -0.146 & -0.146 \\ -0.219 & 0.219 & 0.219 & -0.219 \end{pmatrix} \tag{5.13}$$

The other change-of-basis matrices are calculated similarly (see Figures 5.6, 5.7, 5.8, 5.9). Figure 5.10 shows the trolley change-of-basis matrix.

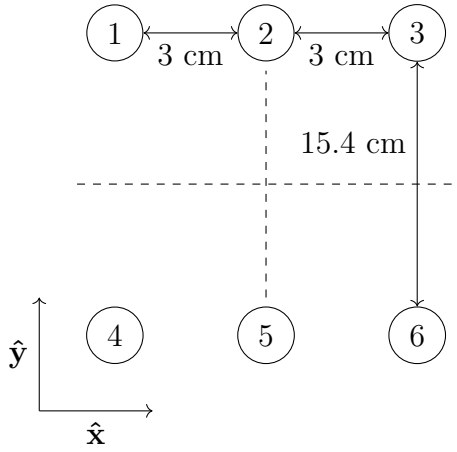

$$\boldsymbol{\Theta}_6 = \begin{pmatrix} 0.1667 & 0.1667 & 0.1667 & 0.1667 & 0.1667 & 0.1667 \\ -0.375 & -0.0 & 0.375 & -0.375 & -0.0 & 0.375 \\ 0.0974 & 0.0974 & 0.0974 & -0.0974 & -0.0974 & -0.0974 \\ -0.1096 & -0.0 & 0.1096 & 0.1096 & -0.0 & -0.1096 \\ 0.5625 & -1.125 & 0.5625 & 0.5625 & -1.125 & 0.5625 \\ -0.6575 & 1.3149 & -0.6575 & 0.6575 & -1.3149 & 0.6575 \end{pmatrix}$$

Figure 5.6: The geometry of a 6-probe station, and the corresponding change-of-basis matrix for measurements-to-moments.

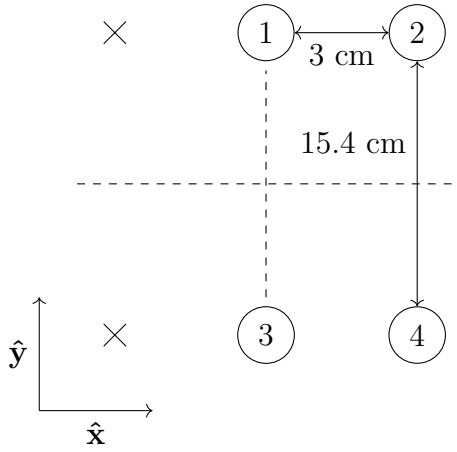

$$\boldsymbol{\Theta}_4 = \begin{pmatrix} 0.5 & 0.0 & 0.5 & 0.0 \\ -0.75 & 0.75 & -0.75 & 0.75 \\ 0.146 & 0.146 & -0.146 & -0.146 \\ -0.219 & 0.219 & 0.219 & -0.219 \end{pmatrix}$$

Figure 5.7: The geometry of a standard 4-probe station, and the corresponding change-of-basis matrix for measurements-to-moments.

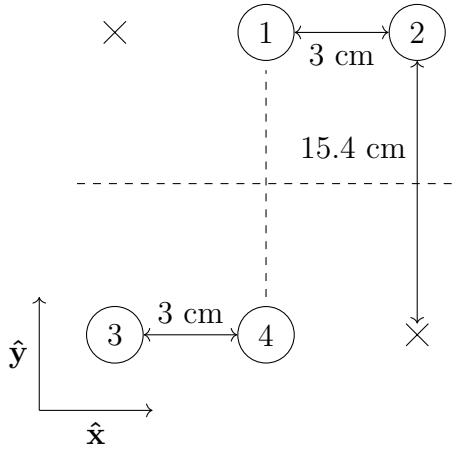

$$\boldsymbol{\Theta}_4^* = \begin{pmatrix} 0.5 & 0.0 & 0.0 & 0.5 \\ -0.75 & 0.75 & -0.75 & 0.75 \\ 0.146 & 0.146 & -0.146 & -0.146 \\ -0.219 & 0.219 & 0.219 & -0.219 \end{pmatrix}$$

Figure 5.8: The geometry of stations 37 and 39 (4-probe stations), and the corresponding change-of-basis matrix for measurements-to-moments.

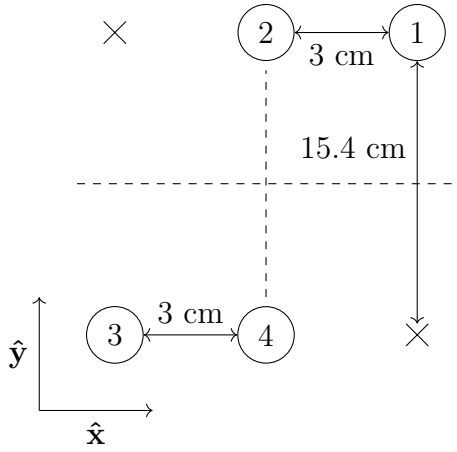

$$\mathbf{\Theta}_4^{**} = \begin{pmatrix} 0.0 & 0.5 & 0.0 & 0.5 \\ 0.75 & -0.75 & -0.75 & 0.75 \\ 0.146 & 0.146 & -0.146 & -0.146 \\ 0.219 & -0.219 & 0.219 & -0.219 \end{pmatrix}$$

Figure 5.9: The geometry of station 41 (4-probe station), and the corresponding change-of-basis matrix for measurements-to-moments.

$$\boldsymbol{\Theta}_{\mathrm{tr}} = \begin{pmatrix}
0.06 & 0.06 & 0.06 & 0.06 & 0.06 & 0.06 & 0.06 & 0.06 & 0.06 & 0.06 & 0.06 & 0.06 & 0.06 & 0.06 & 0.06 & 0.06 & 0.06 \\
0 & 0 & 0 & 0 & 0 & 0 & 0.11 & 0.19 & 0.21 & 0.19 & 0.11 & 0 & -0.11 & -0.19 & -0.21 & -0.19 & -0.11 \\
0 & 0 & 0 & 0 & 0 & -0.21 & -0.19 & -0.11 & 0 & 0.11 & 0.19 & 0.21 & 0.19 & 0.11 & 0 & -0.11 & -0.19 \\
0 & 0 & 0 & 0 & 0 & 0 & -0.24 & -0.24 & 0 & 0.24 & 0.24 & 0 & -0.24 & -0.24 & 0 & 0.24 & 0.24 \\
0 & -0.07 & 0.07 & -0.07 & 0.07 & -0.26 & -0.13 & 0.13 & 0.26 & 0.13 & -0.13 & -0.26 & -0.13 & 0.13 & 0.26 & 0.13 & -0.13 \\
0 & 0 & 0 & 0 & 0 & 0 & -0.35 & 0 & 0.35 & 0 & -0.35 & 0 & 0.35 & 0 & -0.35 & 0 & 0.35 \\
0 & 0 & 0 & 0 & 0 & 0.35 & 0 & -0.35 & 0 & 0.35 & 0 & -0.35 & 0 & 0.35 & 0 & -0.35 & 0 \\
-0.01 & 0.02 & 0.02 & 0.02 & 0.02 & 0.45 & -0.23 & -0.23 & 0.45 & -0.23 & -0.23 & 0.45 & -0.23 & -0.23 & 0.45 & -0.23 & -0.23 \\
0 & 0 & 0 & 0 & 0 & 0 & 0.39 & -0.39 & 0 & 0.39 & -0.39 & 0 & 0.39 & -0.39 & 0 & 0.39 & -0.39 \\
0 & 0 & 74.95 & 0 & -74.95 & 0 & -3.22 & -10.65 & -15.81 & -10.65 & -3.22 & 0 & 3.22 & 10.65 & 15.81 & 10.65 & 3.22 \\
0 & -74.95 & 0 & 74.95 & 0 & 15.81 & 10.65 & 3.22 & 0 & -3.22 & -10.65 & -15.81 & -10.65 & -3.22 & 0 & 3.22 & 10.65 \\
0 & -0.01 & 0.01 & -0.01 & 0.01 & -0.38 & 0.38 & -0.38 & 0.38 & -0.38 & 0.38 & -0.38 & 0.38 & -0.38 & 0.38 & -0.38 & 0.38 \\
0 & 0 & 0 & 0 & 0 & 0 & 0 & 0 & 0 & 0 & 0 & 0 & 0 & 0 & 0 & 0 & 0 \\
0 & 0 & -123.9 & 0 & 123.9 & 0 & 5.81 & 16.77 & 27.1 & 16.77 & 5.81 & 0 & -5.81 & -16.77 & -27.1 & -16.77 & -5.81 \\
0 & -123.9 & 0 & 123.9 & 0 & 27.1 & 16.77 & 5.81 & 0 & -5.81 & -16.77 & -27.1 & -16.77 & -5.81 & 0 & 5.81 & 16.77 \\
0 & 0 & 0 & 0 & 0 & 0 & 0 & 0 & 0 & 0 & 0 & 0 & 0 & 0 & 0 & 0 & 0 \\
0 & 0 & 0 & 0 & 0 & 0 & 0 & 0 & 0 & 0 & 0 & 0 & 0 & 0 & 0 & 0 & 0
\end{pmatrix}$$

Figure 5.10: The change-of-basis matrix for the trolley measurements to multipole moments. Notice the rows of zeros, which correspond to the skew 14-pole (unmeasurable), the skew 18-pole (indistinguishable from the skew 10-pole), and the normal 18-pole (omitted due to minor aliasing issues with the dipole and normal 10-pole).

5.2 The Jacobian Matrix

As covered in Section 5.1, the trolley and fixed probe systems measure moments of the B_y field in different bases, respecting the different symmetry of the geometry of each set of probes. The prescribed treatment shows that the two different sets of moments are equivalent if the moments can be calculated perfectly. However, because they are calculated as discrete approximations, the two sets are not identical and one must take steps to convert between one set and the other. We write the linear part of a Taylor expansion of trolley moments as a function of the fixed probe moments,

$$\mathbf{m}^{\mathrm{tr}}(t) \approx \mathbf{m}_0^{\mathrm{tr}} + \frac{\partial \mathbf{m}^{\mathrm{tr}}}{\partial \mathbf{m}^{\mathrm{fp}}} \cdot \left(\mathbf{m}^{\mathrm{fp}}(t) - \mathbf{m}_0^{\mathrm{fp}} \right). \tag{5.14}$$

The trolley measures 14 of the first 17 multipole moments well (as discussed in Section 5.1) and, as the best measurement of the field in the muon storage region we have, is taken to be the "gold standard." The above equation shows that, in order to understand how the (measured) multipole moments change as a function of the measured Cartesian moments changing, we must calculate the Jacobian matrix J_{ij} between the two,

$$J_{ij} = \frac{\partial m_i^{tr}}{\partial m_j^{fp}}. \tag{5.15}$$

5.2.1 Calculating the Jacobian Matrix

To calculate the Jacobian defined by Equation 5.15, two assumptions must be made. The first assumption is that the trolley accurately measures the multipole moments defined in Equation 5.7. This assumption breaks down when there are many higher-order moments present in the real field ($n = 10$ and above, corresponding to the 22-pole and higher), as the higher-order moments alias into the measurement of the lower-order moments as discussed for the skew 10- and 18-poles. However, these higher order moments are largely suppressed in this experiment by the symmetry of the magnet, which, to large degree, does not have the $n = 10$ and higher structures that would generate such multipoles. Additionally, these moments are further suppressed in the actual muon storage region by their r^n dependence. At higher radii, such as where the fixed probe sit, these moments can become non-negligible, leading to Concept 1.

The second assumption is that, because both sets of moments are calculated by linear combinations of the measured magnetic field that is itself a linear object, the dependence between the trolley and fixed probe moments must also be linear. This means that we only need to calculate the relationship between the basis vectors $m_1, m_2 ... m_5$ of the trolley and

fixed probes to fully characterize the transformation. Here $k = 5$ for both 4-probe stations and 6-probe stations. Even though the 6-probe measurements can approximately measure m_6, because of their low azimuthal extent around the storage region, they are sensitive to other higher-order moments and susceptible to noise. Because m_6 doesn't alias into the lower order moments anyway, it is omitted from the Jacobian calculation — it is not important to track over time using the fixed probes.

Tracking m_5 at a 4-probe station is tricky because the 4-probe station can't inherantly measure m_5. Instead, at each 4-probe station, the value of m_5 is interpolated from the neighboring two stations (always 6-probe stations). This approximation requires us to make the assumption that the differential drift of m_5, the difference in the drift between neighboring stations, is small, and therefore that the interpolated value is an appropriate substitution. Systematically, any incorrectness in this assumption gets absorbed into the sync offsets for the 4-probe stations, which gives us an easy method for tracking the uncertainty caused by this assumption.

To calculate $\mathbf{J}$, it is easier to calculate $\mathbf{J}^{-1}$ first. This is how the measured Cartesian moments change as a function of the multipole moments. Because the field is linear in the moment strength parameter, the derivative with respect to the multipole strength is simply the measured Cartesian moments given a multipole moment strength of 1. One must simply calculate the field at each fixed probe location given a pure multipole input field and calculate the Cartesian moments measured by the fixed probes. In the ideal case of perfect measurements, the Jacobian matrix would be the identity, with each set of probes measuring the same quantities. However, there are off-diagonal terms in the Jacobian cause by asymmetries in the fixed probe positions.

It is important to mention that there are two reasons that the two different bases are not identical. As mentioned above, the discrete nature of the fixed probes can cause higher order moments to alias into the lower ones. Perhaps the best example of this is that the normal sextupole caused a false dipole reading in the fixed probes. Because the fixed probes have a poor angular distribution around the storage region, they all sit in regions where the normal sextupole is greater than zero. When the average of all six probes is taken, it will be non-zero, creating a false dipole reading. The Jacobian treatment corrects for this by calculating how much the sextupole aliases into the dipole measured by the fixed probes this way, and then uses the fixed probe station's own measurement of the m_5 moment to make a correction.

The second reason that the two bases are not identical is that the geometry of the fixed probes in a given station are not always symmetric. For example, standard 4-probe stations are not centered around $(0, 0)$ but $(1.5 \text{ cm}, 0)$. This means, for example, that a straight

average of the four probes would be an approximation of the field at $(1.5\text{ cm}, 0)$, not $(0, 0)$. A correction would then have to be made that mixes the measured m_2 into the m_1, using the horizontal gradient to approximate the field on center. The result of this correction turns out to be to use the average of only the two centered probes, as preempted in Section 5.1. However, there are other examples of fixed probe stations with odd geometries that are not already corrected in the change-of-basis matrix. For example, all the fixed probes in the inflector vacuum chamber are shifted radially inward by 1 cm, and the four probe stations by the trolley garage are not symmetric across the x axis. These interesting geometries cause off-diagonal entries in the Jacobian.

5.2.2 Sample Jacobian Calculation

Multipole (strength 1)	Cartesian moment	Value
m_1	m_1	1
	m_2	0
	m_3	0
	m_4	0
	m_5	0
m_2	m_1	0
	m_2	1
	m_3	0
	m_4	0
	m_5	0
m_3	m_1	0
	m_2	0
	m_3	1
	m_4	0
	m_5	0
m_4	m_1	0
	m_2	0
	m_3	0
	m_4	1
	m_5	0
m_5	m_1	-2.632
	m_2	0
	m_3	0
	m_4	0
	m_5	1

Table 5.4: The Cartesian moments measured by a standard 6-probe station, given an input pure multipole field of multipole strength $m_i = 1$.

Here is a walk-through of the Jacobian calculation for a standard 6-probe station. Recall that since we are only interested in the first five moments, we only worry about those moments. The values of the Cartesian moment given a specific input multipole are shown in Table 5.4. They lead to

$$\mathbf{J}^{-1} = \begin{pmatrix} 1 & 0 & 0 & 0 & -2.632 \\ 0 & 1 & 0 & 0 & 0 \\ 0 & 0 & 1 & 0 & 0 \\ 0 & 0 & 0 & 1 & 0 \\ 0 & 0 & 0 & 0 & 1 \end{pmatrix}. \tag{5.16}$$

Taking the inverse of this matrix yields the Jacobian for a standard 6-probe station.

$$\mathbf{J} = \begin{pmatrix} 1.0 & 0 & 0 & 0 & 2.632 \\ 0 & 1.0 & 0 & 0 & 0 \\ 0 & 0 & 1.0 & 0 & 0 \\ 0 & 0 & 0 & 1.0 & 0 \\ 0 & 0 & 0 & 0 & 1.0 \end{pmatrix} \tag{5.17}$$

Note the off-diagonal term that corrects the measured Cartesian m_1 with the measured Cartesian m_5. All of the different station geometries and the Jacobians they generate are shown in Figures 5.11, 5.12, 5.13, and 5.14.

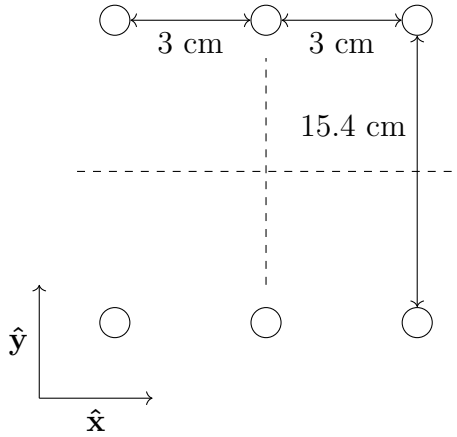

$$\mathbf{J} = \begin{pmatrix} 1.0 & 0 & 0 & 0 & 2.632 \\ 0 & 1.0 & 0 & 0 & 0 \\ 0 & 0 & 1.0 & 0 & 0 \\ 0 & 0 & 0 & 1.0 & 0 \\ 0 & 0 & 0 & 0 & 1.0 \end{pmatrix}$$

Figure 5.11: The geometry of a 6-probe station, and the corresponding Jacobian matrix.

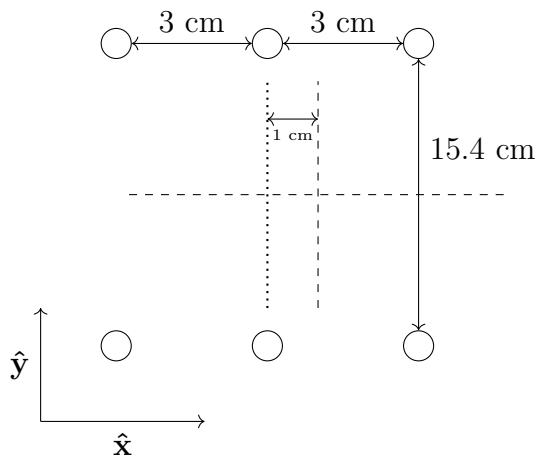

$$\mathbf{J} = \begin{pmatrix} 1.0 & 0.222 & 0 & 0 & 2.681 \\ 0 & 1.0 & 0 & 0 & 0.444 \\ 0 & 0 & 1.0 & 0.444 & 0 \\ 0 & 0 & 0 & 1.0 & 0 \\ 0 & 0 & 0 & 0 & 1.0 \end{pmatrix}$$

Figure 5.12: The geometry of an offset 6-probe station, and the corresponding Jacobian matrix. The change-of-basis matrix for offset stations are not corrected; instead, the correction for the offset is done with the Jacobian.

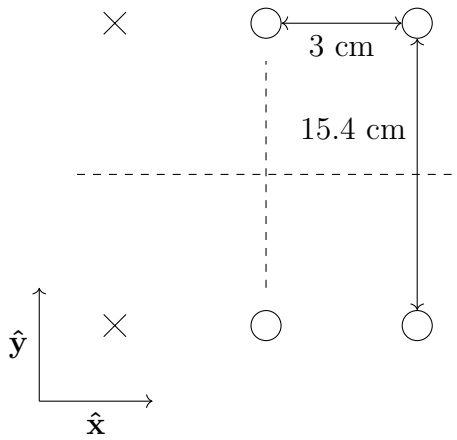

$$\mathbf{J} = \begin{pmatrix} 1.0 & 0 & 0 & 0 & 2.928 \\ 0 & 1.0 & 0 & 0 & -0.667 \\ 0 & 0 & 1.0 & -0.667 & 0 \\ 0 & 0 & 0 & 1.0 & 0 \\ 0 & 0 & 0 & 0 & 1.0 \end{pmatrix}$$

Figure 5.13: The geometry of a 4-probe station, and the corresponding Jacobian matrix.

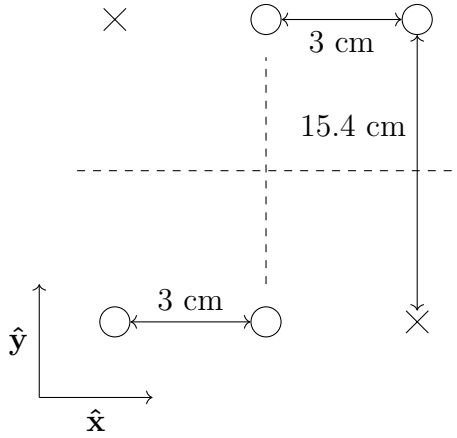

$$\mathbf{J} = \begin{pmatrix} 1.0 & 0 & 0 & 0 & 2.928 \\ 0 & 1.0 & 0 & 0 & 0 \\ 0 & -0.195 & 1.0 & 0 & 0 \\ 0 & 0 & 0 & 1.0 & -0.195 \\ 0 & 0 & 0 & 0 & 1.0 \end{pmatrix}$$

Figure 5.14: The geometry of a 4-probe station near the trolley garage, and the corresponding Jacobian matrix. It is important to note that, because the moments for these different 4-probe stations are defined by geomtery, and not by probe number, there is not a different Jacobian for stations 37 and 39 versus station 41, unlike with the change-of-basis matrices.

CHAPTER VI

Fixed Probe Interpolation

The general strategy for interpolating the magnetic field map from the data is to use two trolley runs to bracket an interval in time with a well-measured field map in the muon storage region at the endpoints. Between the trolley runs, the fixed probe measurements are used to estimate changes of the field, interpolate the tracked moments, and generate what we call "virtual trolley measurements" (VTMs). The VTMs and the trolley measurements are synchronized during trolley runs, and changes from the synchronized values are tracked using Jacobian-weighted fixed probe measurements. If only the lowest-order moments drifted between trolley runs, this method would always acurately reconstruct the field because the lowest-order moments are estimated by the fixed probes (see Table 5.3). However, because higher-order moments do drift, the VTMs do not perfectly track the field, leading to Concept 1.

Concept 1. *The fixed probes do not perfectly track the trolley moments predominantly due to changes in the higher-order magnetic field moments. This is called "higher-order gradient drift".*

The field measured by probes in an azimuthal slice, whether they are the fixed probes or the trolley probes, are highly correlated to each other due to the large average (dipole) field. It is easier to measure the field in a slice by considering sum and difference modes of the different probes. This leads us to consider moments of the field rather than individual probe measurements. The historical moments for trolley measurements are the 2D multipoles; these expansions are covered in depth in Chapter V.. The trolley is specifically designed to measure the field in the multipole expansion. The fixed probes don't have the proper spatial distribution to measure in the 2D multipole basis. The most symmetric moments to associate with sum and differences modes are approximations of the field gradients in the Cartesian coordinate system.

Going forward, we use the notation m_i^{tr} to denote the ith trolley moment, and m_j^{fp} to denote the jth fixed probe moment (see Table 5.3), both in a particular slice of azimuth. We will also occasionally use the notation $\mathbf{m}^{\text{tr}}$ and $\mathbf{m}^{\text{fp}}$ to denote the vector of all moments in the slice. Note that these vectors do not correspond to physical field vectors, but are elements of $\mathbb{R}^{17}$ (trolley), $\mathbb{R}^6$ (6-probe stations), or $\mathbb{R}^4$ (4-probe stations).

Both $\mathbf{m}^{\text{tr}}$ and $\mathbf{m}^{\text{fp}}$ are functions of the field and are therefore related to each other. The trolley is our standard for the field measurements, so we use the fixed probes to approximate the trolley measurements, writing the linear term of the Taylor expansion of the trolley moments as a function of the fixed probe moments. Higher order terms are related to the unmeasurable higher-order moments and are accounted for in the systematic error analysis.

$$\begin{aligned}\mathbf{m}^{\text{tr}}\left(\mathbf{m}^{\text{fp}}(t)\right) &\approx \mathbf{m}^{\text{tr}}\left(\mathbf{m}^{\text{fp}}(0)\right) + \frac{\partial \mathbf{m}^{\text{tr}}}{\partial \mathbf{m}^{\text{fp}}} \cdot \left(\mathbf{m}^{\text{fp}}(t) - \mathbf{m}^{\text{fp}}(0)\right) \\ \mathbf{m}^{\text{tr}}(t) &\approx \mathbf{m}_0^{\text{tr}} + \mathbf{J} \cdot \left(\mathbf{m}^{\text{fp}}(t) - \mathbf{m}_0^{\text{fp}}\right) \end{aligned} \tag{6.1}$$

Four quantities are required in order to calculate a virtual trolley measurement from a single fixed probe station: $\mathbf{m}_0^{\text{tr}}$, $\mathbf{m}_0^{\text{fp}}$, $\mathbf{m}^{\text{fp}}(t)$, and the Jacobian matrix $\mathbf{J} = \frac{\partial \mathbf{m}^{\text{tr}}}{\partial \mathbf{m}^{\text{fp}}}$. The first two are measured simultaneously during a trolley run while the trolley is near each fixed probe station, which sets the synchronization time $t_{st} = 0$ for each station indexed by st (the baseline time is different for each station due to the finite time it takes for the trolley to travel through a given region of azimuth), and resynchronizes the two sets of probes at that time. $\mathbf{m}^{\text{fp}}(t)$ is monitored continuously during the experiment by the fixed probes stations. That last required quantity, the Jacobian matrix, is determined analytically. Simulation or dedicated studies in the ring using applied magnetic field moments from the surface coils can also be used to determine the Jacobian. Combining these as shown in Equation 6.1 produces a linear approximation for the moments the trolley would have measured at that time. This is a virtual trolley measurement.

The best information about the field the muons average during storage comes from trolley runs. During these runs, we get information that is "dense in space but sparse in time." NMR data from these times "pin" the field, so we have a good idea of the nature of the field at particular times. In the following analysis, the baseline measurements $\mathbf{m}_{st}^{\text{tr}}(0)$ and $\mathbf{m}_{st}^{\text{fp}}(0)$ from each fixed probe station represent these pinned field numbers.

The fixed probe runs are the compliment to the trolley runs because they are "sparse in space but dense in time." "Sparse in space" here means three things. First, the fixed probes make only 72 azimuthal measurements (as opposed to the thousands of azimuthal positions from a trolley run). Second, there is a maximum of six fixed probes per station, which limits

the number field moments we can measure to, at most, six per station. Third, the fixed probes live outside the muon storage region. Despite these three limitations, the fixed probes provide value by measuring approximately every 1.5 seconds including during muon injections. They provide extra points for interpolating the field between trolley measurements.

The Jacobian that relates the fixed probe measurements to the trolley measurements encodes most of the geometry of the experiment. (Some geometry is represented by choice of moments, discussed in Section 5.1, but those choices were made to simplify the Jacobian.) It can be calculated in several ways. The current best calculation comes from simulation and will be discussed in Section 6.4, but efforts are also underway to extract it from a special surface coil study, and to calculate it analytically.

Matrix Method Algorithm

The steps comprising the matrix method algorithm are explained in detail in the rest of this chapter. They are listed here to provide an overview of the full process.

1. Read the trolley run and fixed probe run data from the tier 1 ROOT files. Apply the plunging probe calibrations to each trolley probe's raw frequencies. (The current data comes from the v09_20_00 production data.)

2. Interpolate all NMR probe frequencies and trolley positions onto a common time grid.

3. Convert all NMR measurements to moment measurements.

4. During trolley runs, while the trolley is near fixed probe station i, determine the average of the trolley and fixed probe station moments ($\mathbf{m}_{st}^{\mathrm{tr}}(0)$ and $\mathbf{m}_{st}^{\mathrm{fp}}(0)$, respectively).

5. Synchronize the trolley and fixed probe moment measurements during the trolley runs. Use the fixed probe runs to interpolate the fixed probe measurements between the trolley runs, interpolating both forward and backward. This interpolation produces virtual trolley measurements.

6. At this point, we have the full field map that will be weighted by the muon distribution and integrated as discussed in Chapter VII. However, it is also to determine unweighted field maps for discussions of the field independent of the muon weighting, so it can be useful to perform two more steps.

7. Bin the events into a longer time grid. The specific grid depends on the ω_a subrun times. (In this chapter, no additional time averaging is shown.)

8. Perform an average of the 72 fixed probe stations for each moment for each time bin. The average is weighted by the azimuthal extent of each station.

The outputs of this algorithm are azimuthally averaged moments, averaged over the specified time bins. In this chapter, I present an example of the matrix method algorithm by applying it to the "60 hour" data set. This data set consists of two trolley runs bracketing approximately 60 hours of production muon data. For this example, the average field (dipole field, m_1) is blinded by a small offset, because the absolute calibration is still blinded. The higher-order moments, however, are not blinded.

6.1 Time-Grid Interpolation

The input data to this analysis are measurements from the fixed probe runs and trolley runs. Notably, from the trolley, they contain the time, trolley position, and extracted FID frequency for each event. The trolley records all 17 probes consecutively approximately every half-second. The fixed probe data contain the time, FID frequency, and a data quality tag for each event. The fixed probe system records data from all 378 fixed probe approximately every 1.5 seconds (1.1 seconds in Run 2).

The measurements from the trolley and fixed NMR probes happen asynchronously. The trolley moves between each measurement within a single event, and each of the 17 probes records its frequency at a slightly different azimuthal position. The fixed probes face a similar issue where each of the probes connected to a single multiplexer records at a slightly different time, meaning that each measurement from an azimuthal station is at a different time. Additionally, the trolley and the fixed probe measurements are not synchronized, so a full event from the trolley is not guaranteed to have an associated event from the fixed probes.

The fixed probe measurement have associated data quality tags. The FIDs for the event are compared against templates generated for each individual probe. If the FID under scrutiny does not have a similar amplitude, length, or power, it is flagged. A common cause for these flags in Run 1 is electrical interference from other system causing false triggers in the NMR system. The cause of the interference was identified and shielded during Run 1, but many data runs still have the interference affecting the FIDs. Even in cases of extreme interference, fewer than 1% of FIDs are flagged for data quality problems.

To simplify the analysis and its interpretation, all the NMR data is synchronized by interpolating the individual fixed probe frequency onto a common *time grid*, used for both the trolley and fixed probe. The grid is centered every second on POSIX time (seconds since 00:00:00 UTC on 1 January 1970). The raw time and frequency data pairs for each

NMR probe define an interpolating function using a simple linear spline. This interpolating function is integrated in one second bins, centered on the time grid, to find the average field in that bin. This interpolation method has the benefit of making future time averaging steps easier. Summing consecutive interpolation points is equivalent to integrating the raw data over the same amount of time, which preserves the definition of time-averaged fields in a convenient way. This method also allows for fixed probe events flagged for a data quality cut to be dropped first without requiring a redefinition of the interpolation points. Note that this interpolation procedure is also applied to all the trolley position measurements, not just the NMR probe frequencies.

Before interpolation, each trolley event contains 17×3 numbers (the time, position, and frequency for each probe in the event) and each fixed probe event contains 378×3 numbers (the time, frequency, and data quality tag for each probe). After interpolation, each *combined* event contains $1 + 1 + 17 + 378$ quantities: the interpolation time from the grid, the interpolated trolley position at that time, and the interpolated NMR frequency from each of the trolley and fixed probes at the interpolation time. See Figure 6.1 for a sample output from frequency measurements from fixed probe 200.

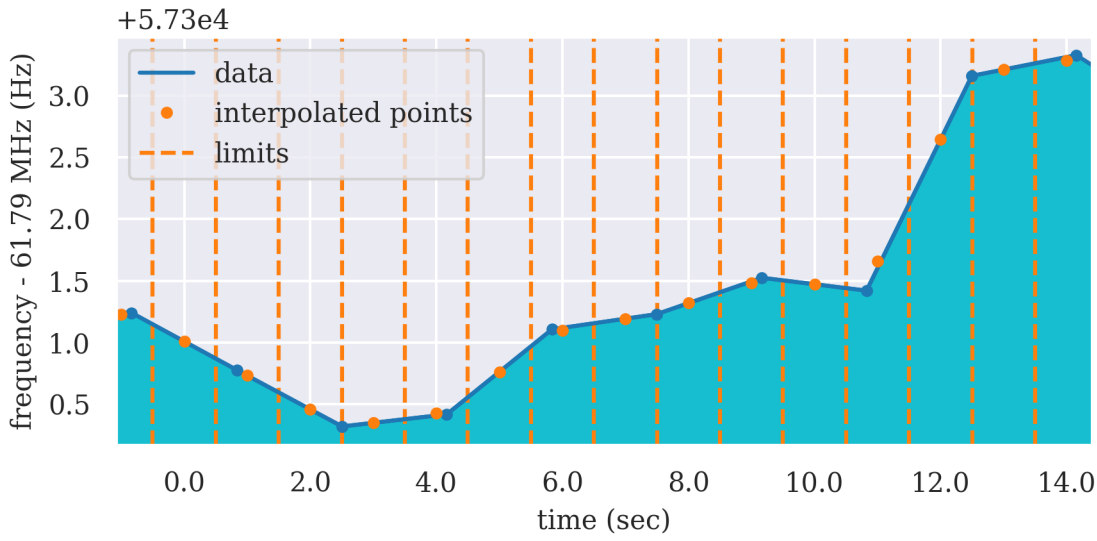

Figure 6.1: A sample of measurements from fixed probe 200 during the 60 hour data set before and after it is interpolated onto the new time grid. The dashed lines show the integration boundaries for each orange interpolated frequency.

This interpolation scheme comes with two related caveats due to over- and under-sampling. The time grid under-samples the trolley NMR data, which is taken at approximately 0.5 second intervals. The time grid acts as a low pass filter in this case; each interpolation point is a combination of several raw data points. This smooths the data, and

is especially useful in reducing the effect of spikes in FIDs caused by trolley motional effects. The one second time grid over-samples the fixed probe data, where there are sometimes two interpolated points between neighboring raw data points. This is not a problem, though, because further time averaging occurs at later stages in the analysis. This is where the mean-preserving definition of the interpolated points shines, allowing time bins to be chosen at later times in the analysis, without having to redefine the initial time grid.

As noted, the data consists of measurements from 378 fixed probes (plus 17 trolley probes and the trolley position if the run being considered is a trolley run), all interpolated onto a one-second time grid. At this point the change-of-basis matrices discussed in Chapter V are applied to the probes from each station to form 378 (+ 17) field moments. A further step is taken at this point: even though the 4-probe stations only measure the first four moments of the field, for reasons that are discussed in Section 5.2, it is useful to track an estimate of the fifth moment at the 4-probe stations. The estimate used at each 4-probe station is the average of the m_5 value from the adjacent 6-probe stations, weighted by their proximity to the 4-probe station. The nearest stations to any 4-probe station are always 6-probe stations; there are no instances of two 4-probe stations in a row.

6.2 Trolley Footprint Veto

As the trolley drives past a fixed probe station i, the trolley's magnetic image perturbs the fixed probes (Figure 6.2a). This perturbation needs to be removed from the fixed probe data before time averaging to calculate $\mathbf{m}_i^{\mathrm{fp}}(0)$. To remove the trolley image from a given fixed probe station, we veto all events from the fixed probe measurements during the time the trolley was close enough to influence them measurably (25 degrees of azimuth about the fixed probe location). The local drift in time is calculated by fitting a 5th-degree polynomial to the remaining non-vetoed data (Figure 6.2b). Meanwhile, data from the stations not being perturbed by the trolley (defined as all stations in the ring more than 3 stations away from the station in question and excluding the particularly noisy stations 0-5) is averaged to estimate the ring-wide transients and used as a replacement for the vetoed region. The global drift is calculated by fitting a 1st-degree polynomial to the replacement data (Figure 6.2c). The global drift is subtracted from the replacement data to estimate the short-term transient behavior, and then the local drift is added. Finally, the replacement data is inserted into the vetoed region (Figure 6.2d). The overall effect of this replacement method is that the average moment measured by the fixed probe station is dominated by the "local drift," the portions of the data measured when the trolley is not perturbing the station. However, it also allows for corrections from short-scale transients that are experienced around the ring,

which would otherwise be masked by the veto over the station.

6.3 Trolley-Fixed Probe Synchronization

Averaging occurs for each station while the trolley is "under" that station. Because the final goal of this analysis is an azimuthal average, we want to include all of the trolley measurements in the analysis. Therefore, the trolley is always "under" a station, which is defined to be the closest station. The fixed probe station moments are averaged over time while the trolley is under that station. Note that this means the average is over the replacement values from the trolley image removal.

The trolley moments are averaged over azimuth while the trolley is under that station. Recall that the trolley position is also interpolated onto the same time grid as the field measurements, so there is a definite time and position for each event. We weight the average by the azimuthal extent of that particular measurement (the distance between its nearest neighboring measurement in azimuth, divided by two) to account for the trolley's varying speed moving around the ring, approximating

$$\left\langle \mathbf{m}_{st}^{\mathrm{tr}} \right\rangle \Big|_{\phi_1}^{\phi_2} = \frac{\int_{\phi_1}^{\phi_2} \mathrm{d}\phi \; \mathbf{m}^{\mathrm{tr}}(\phi)}{\int_{\phi_1}^{\phi_2} \mathrm{d}\phi} \approx \frac{\sum_{\phi_1 \leq \phi_i < \phi_2} \mathbf{m}_i^{\mathrm{tr}} \Delta\phi_i}{\sum_{\phi_1 \leq \phi_i < \phi_2} \Delta\phi_i}, \tag{6.2}$$

where i indexes the measurements, $\Delta\phi_i$ is the azimuthal extent of the ith measurement, and $\mathbf{m}_i^{\mathrm{tr}}$ is the moment vector of the ith measurement.

For each moment m_i^{tr} of each station, the analysis yields three numbers: the central time of the averaging window (different for each station), the average values the fixed probes measured for the moments while the trolley was present, and the average value the trolley measured averaged over the same time (see Figure 6.3). These effectively set time zero for interpolation in that station, and the measurements of $\mathbf{m}^{\mathrm{tr}}(0)$ and $\mathbf{m}^{\mathrm{fp}}(0)$ in Equation 6.1.

6.4 Virtual Trolley Measurements and the Jacobian Matrix

We calculate virtual trolley measurements (VTMs) from each fixed probe station in each event, during both trolley runs and fixed probe runs. The form of equation 6.1 guarantees that the VTM is equal to the actual (average) trolley measurement at times when the trolley is near the fixed probe station, which is why we call this process "synchronization." The calculation of the virtual trolley measurement requires the synchronization baselines $\mathbf{m}^{\mathrm{tr}}()$ and $\mathbf{m}^{\mathrm{fp}}(0)$, the Jacobian for that station's geometry $\mathbf{J}$, and the station moments from that event $\mathbf{m}^{\mathrm{fp}}(t)$. In terms of these quantities, we can rearrange equation 6.1 into the form

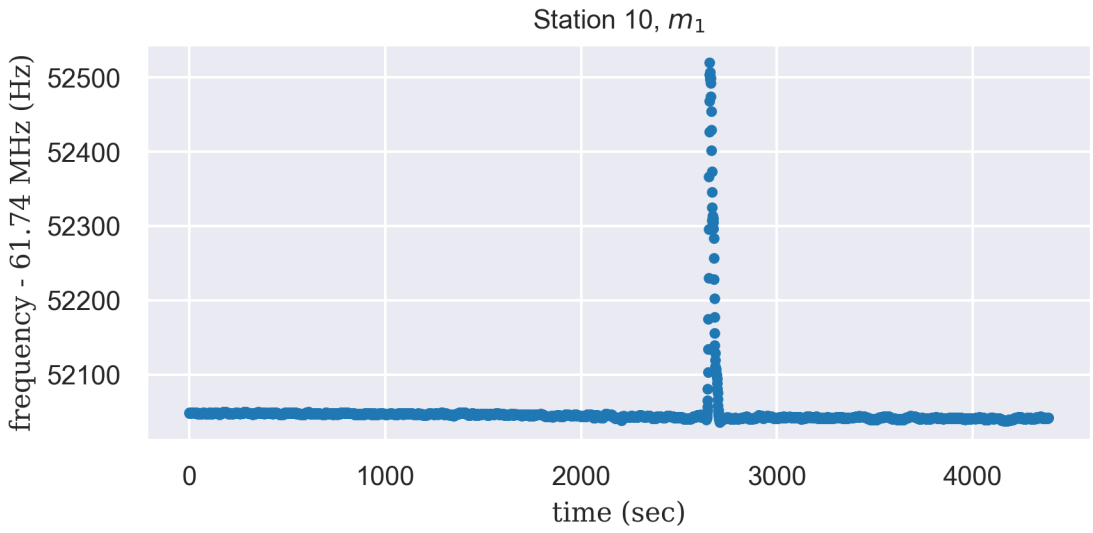

(a) The trolley footprint seen by station 10 as the trolley goes by.

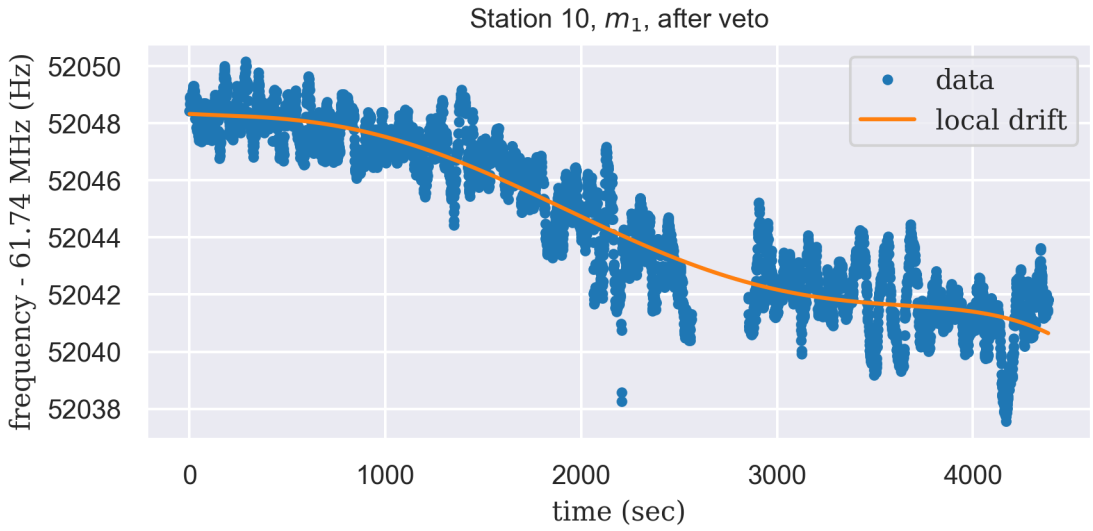

(b) The same measurements from station 10 with the trolley footprint vetoed. The local drift is fit by a fifth-order polynomial.

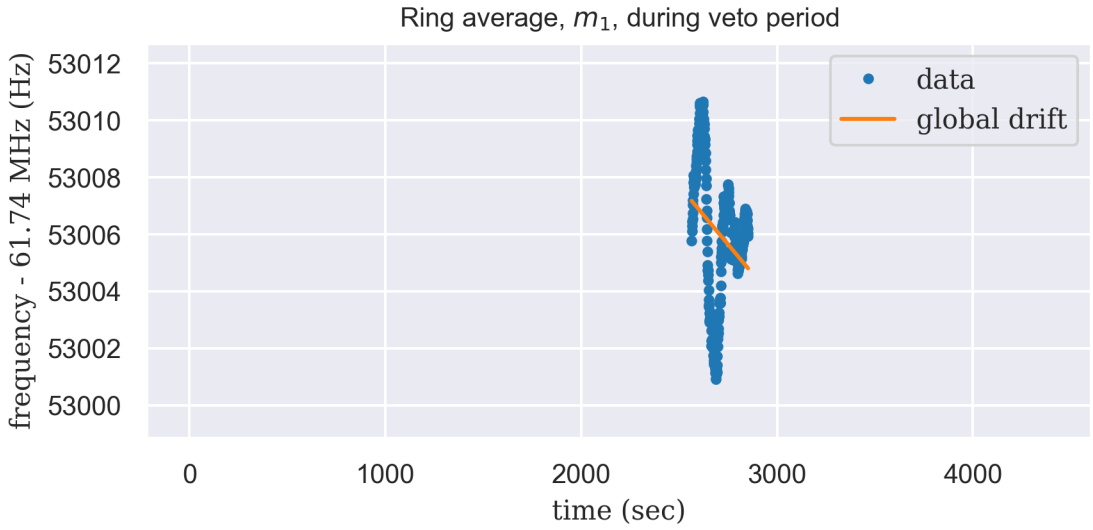

(c) The global field measurement during station 10's vetoed time, calculated from the rest of the ring, and the global drift in the same time.

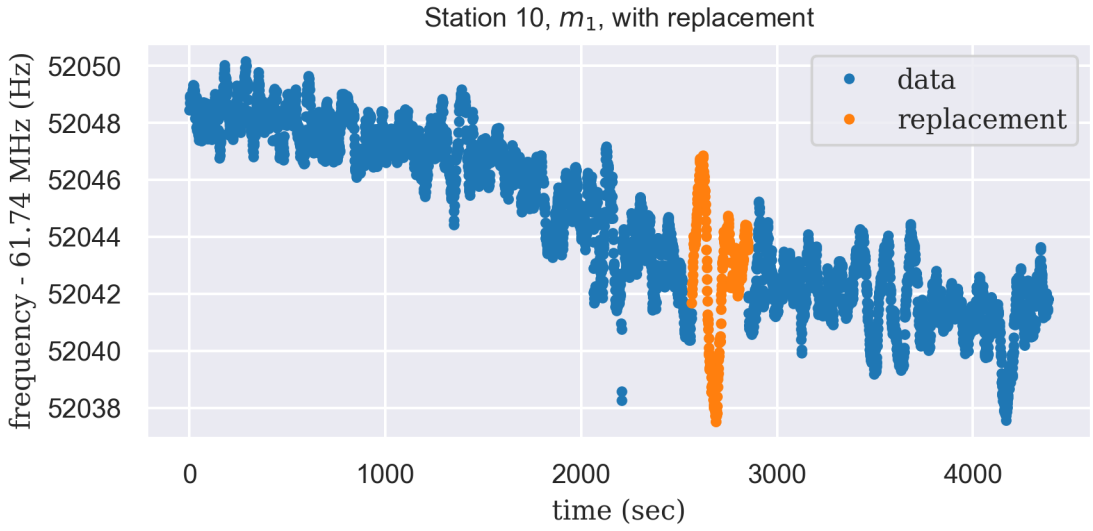

(d) The replacement data inserted into the station 10's vetoed time.

Figure 6.2: The step by step procedure for replacing vetoed fixed probe data by ring-average data, corrected for both local and global drifts.

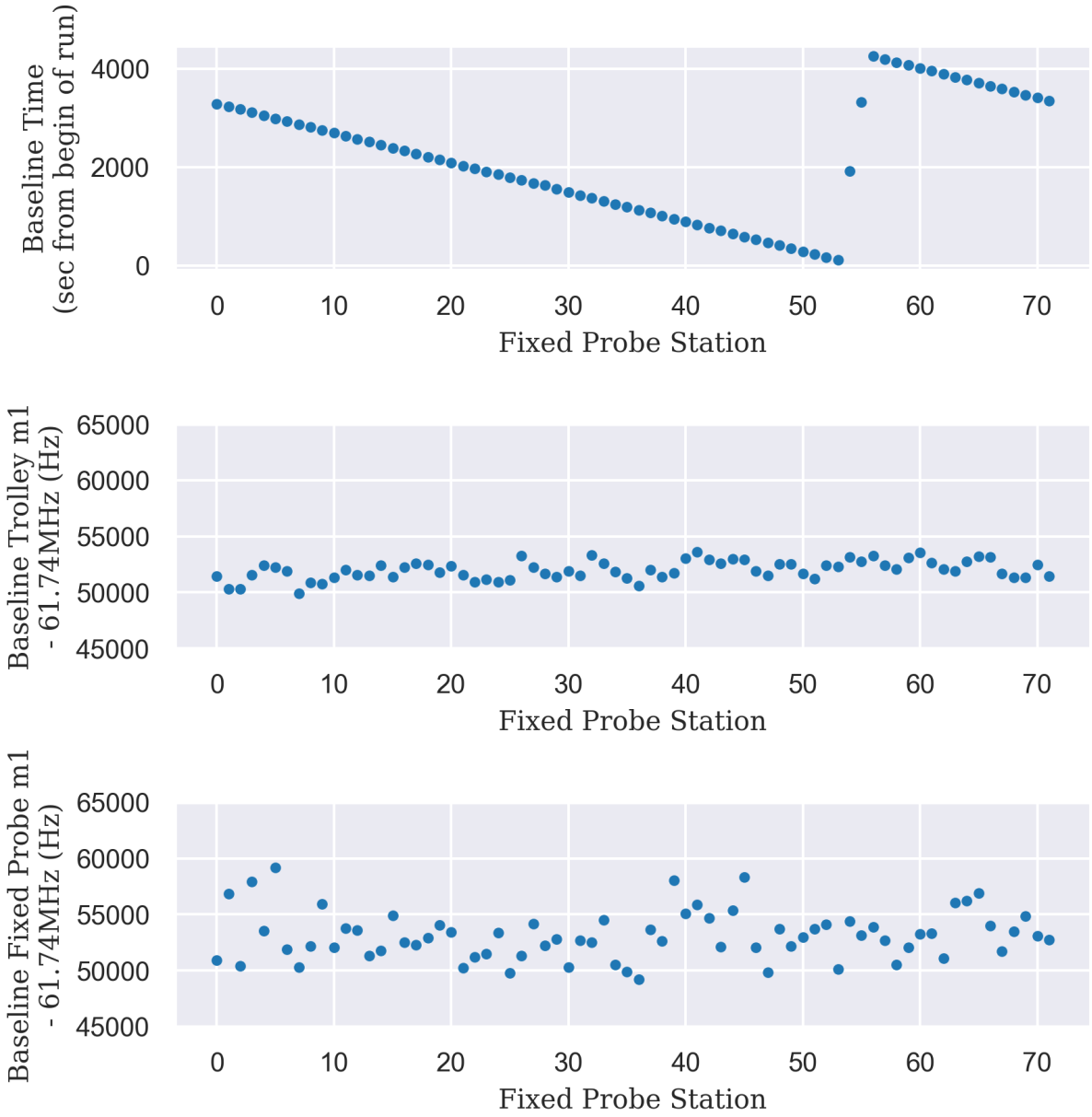

Figure 6.3: Top to bottom: The averaging time, trolley baseline moments $\mathbf{m}_{st}^{\mathrm{tr}}(0)$, and fixed probe baseline moments $\mathbf{m}_{st}^{\mathrm{fp}}(0)$ for each station in Run 3956.

$$\mathbf{m}_{\mathrm{vtr}}(t) = \mathbf{m}^{\mathrm{tr}}(0) + \mathbf{J} \times \left(\mathbf{m}^{\mathrm{fp}}(t) - \mathbf{m}^{\mathrm{fp}}(0)\right). \tag{6.3}$$

See Figure 6.4 for an example for fixed probe station 30, m_1.

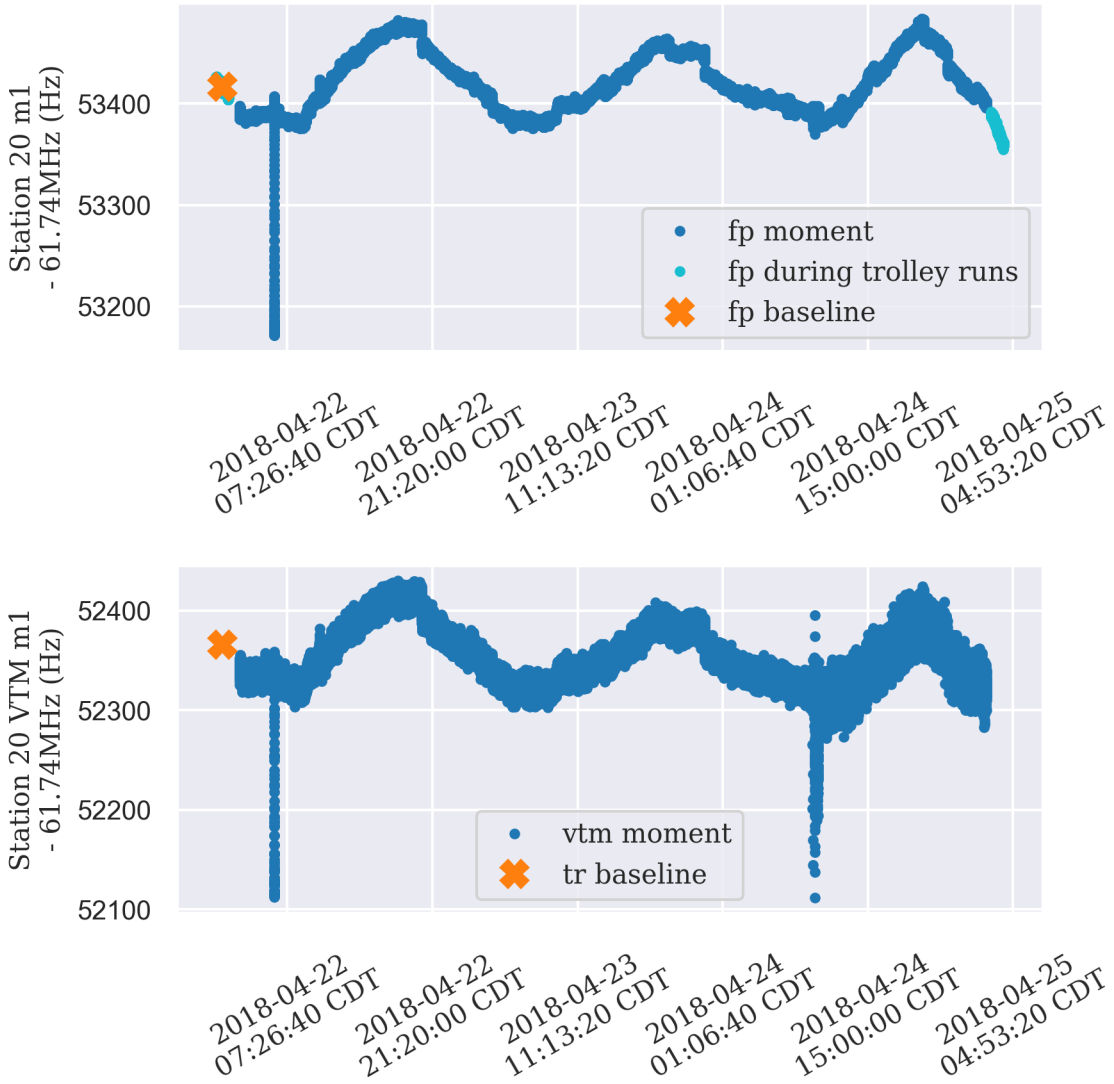

Figure 6.4: Top: The station 20 m_1 measurement from the 60hr data set, showing the baseline fixed probe measurement from the trolley run. Bottom: The station 20 m_1 VTMs, showing the baseline trolley measurement from the trolly run.

As mentioned before, it is useful to track an estimate of the the fifth moment even at 4-probe stations. This is because m_5 aliases into m_1, the average field and most important moment of the field for the analysis, in the fixed probe geometry (see Table 5.3 for moments definitions). This means that, if uncorrected, drift in m_5 will be incorrectly measured as drift

in m_1 in the 4-probe stations. By using the nearest 6-probe stations to estimate the drift, we can correct the measured m_1 from the 4-probe stations. This does introduce *differential drift* (difference in moment drift at different stations) as a systematic uncertainty to the 4-probe stations. However, this uncertainty is absorbed into the sync offset systematic uncertainty because the trolley can pin the m_5 value, even for the 4-probe stations. The approximated drift from the nearest neighbors just acts as a correction on the drift from the synchronized values from the trolley runs..

6.5 Synchronization Interpolation

Production runs include multiple trolley measurements at the beginning and end of the fixed probe runs that monitor the field during muon-data intervals. Having multiple trolley runs means that there are multiple opportunities to sync the virtual trolley measurements to the actual trolley measurements. We define the sync constant $\mathbf{c}$ from a single trolley run by rearranging equation 6.3 (recall that $t = 0$ is different for each station),

$$\mathbf{c} = \mathbf{m}^{\mathrm{tr}}(0) - \mathbf{J} \times \mathbf{m}^{\mathrm{fp}}(0), \tag{6.4}$$

so that

$$\mathbf{m}_{\mathrm{vtr}}(t) = \mathbf{J} \times \mathbf{m}^{\mathrm{fp}}(t) + \mathbf{c}. \tag{6.5}$$

Note that the sync constant is effectively a calibration constant. The trolley calibrates the fixed probe stations as it passes by each station during a trolley run. This is the last step of the calibration chain covered in Chapter IV.

Ideally, two trolley runs would have the same sync constant, which would imply that there would be no difference in the VTMs if we used the initial sync and propagated it forward in time, or if we used the next sync and propagated it backward in time. However, in practice the sync offset does change, as shown by Figure 6.5. The leading order cause of the differences is drifting higher-order moments that are untrackable by the fixed probe stations. Recall that the higher-order moments can be viewed as higher-order gradients of the field. These higher-order moments alias into the measured moments, so any drift in them leads to an error in the fixed probe's measurements. However, these higher-order moment drifts are small and slow compared to the drift of the lower-order moments, which allows us to correct them.

The difference between the sync constants of two trolley runs is essentially a measurement of the drift of these higher-order moments called the sync offset. Figure 6.7 shows the

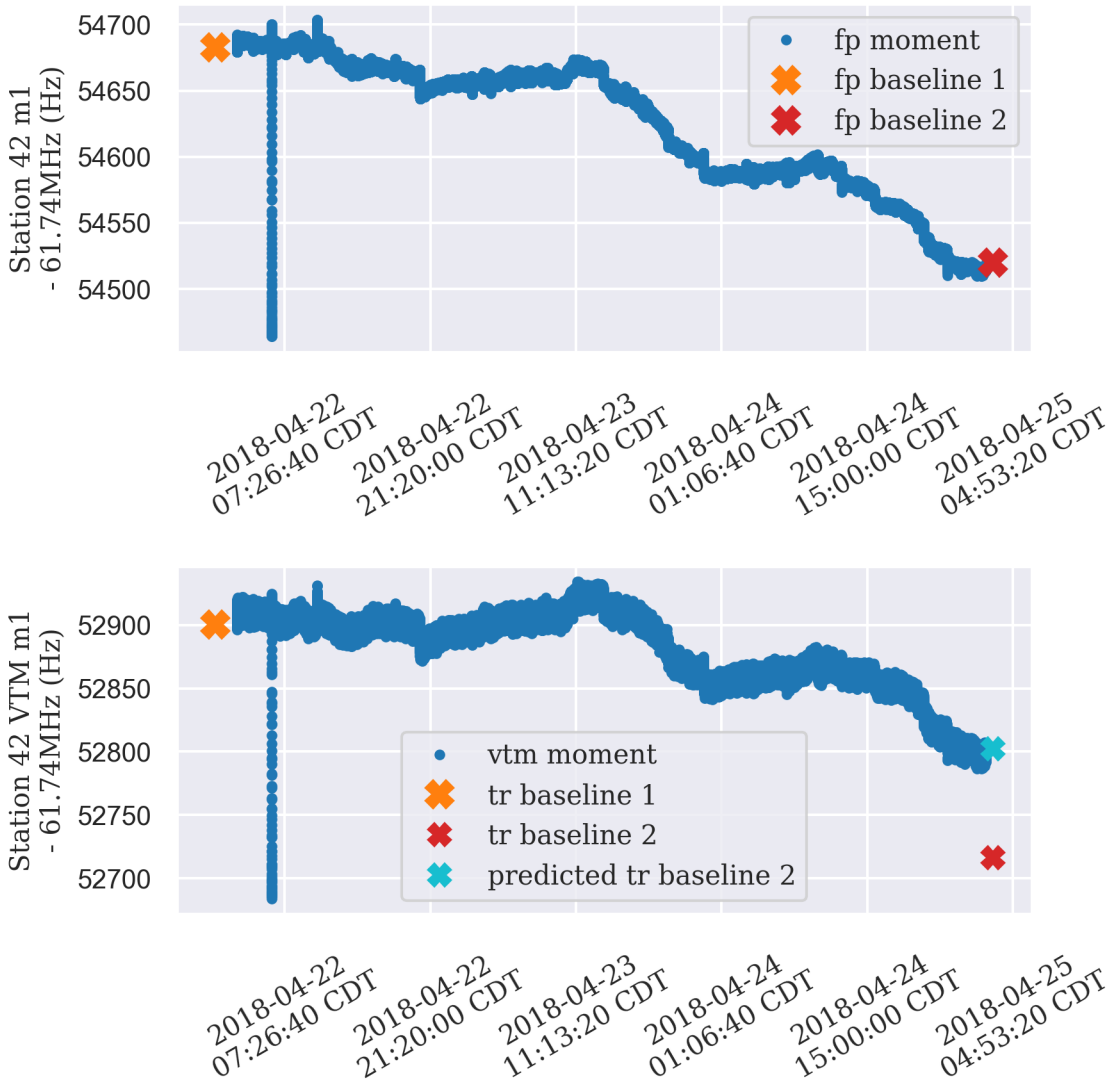

Figure 6.5: The VTM prediction from the fixed probes synced with the first trolley baseline does not match the second trolley baseline. The downward spike at about 2018-04-22 7:00:00 CDT is from a PSFB cycle.

distribution of sync offsets for all 72 stations. We can perform a correction by interpolating the sync constant for each event between the two nearest neighboring trolley runs. Each VTM event has a unique sync offset that is an average of the nearest sync offsets from trolley run, weighted by the proximity of each trolley run. We can define the interpolated sync offset

$$\mathbf{s}(t) = \frac{\mathbf{c}_2 - \mathbf{c}_1}{t_2 - t_1}(t - t_1) + \mathbf{c}_1, \tag{6.6}$$

where $\mathbf{c}_i$ and t_i are respectively the sync constant and sync time measured for the given station by trolley run i (the closest two trolley runs). A final form for each virtual trolley measurement in a given fixed probe station is

$$\mathbf{m}_{\text{vtr}}(t) = \mathbf{J} \times \mathbf{m}^{\text{fp}}(t) + \mathbf{s}(t). \tag{6.7}$$

Figure 6.6 shows the result of applying this "backwards correction" to the same station 2 m_1 shown in Figure 6.5. Between the two plots, the positions of the yellow 'X's do not change.

The backwards correction applies a linear correction to the time dependence of the higher-order moment drift of Concept 1. Any higher-order time dependence in these gradients still cause uncertainty in the fixed probe measurements. There are times when the sync constant can not be interpolated over the fixed probe data. These include times when the fixed probe runs are not bookended by trolley runs, and times when a significant change in the ring casts doubt about the synchronization, such as a major change to the SCC configuration that happens during a fixed probe run. In these cases, only one-way synchronization, forward or backward, can be used. The systematic uncertainties caused by both the two-way and one-way scenarios are discussed further in Chapter VIII.

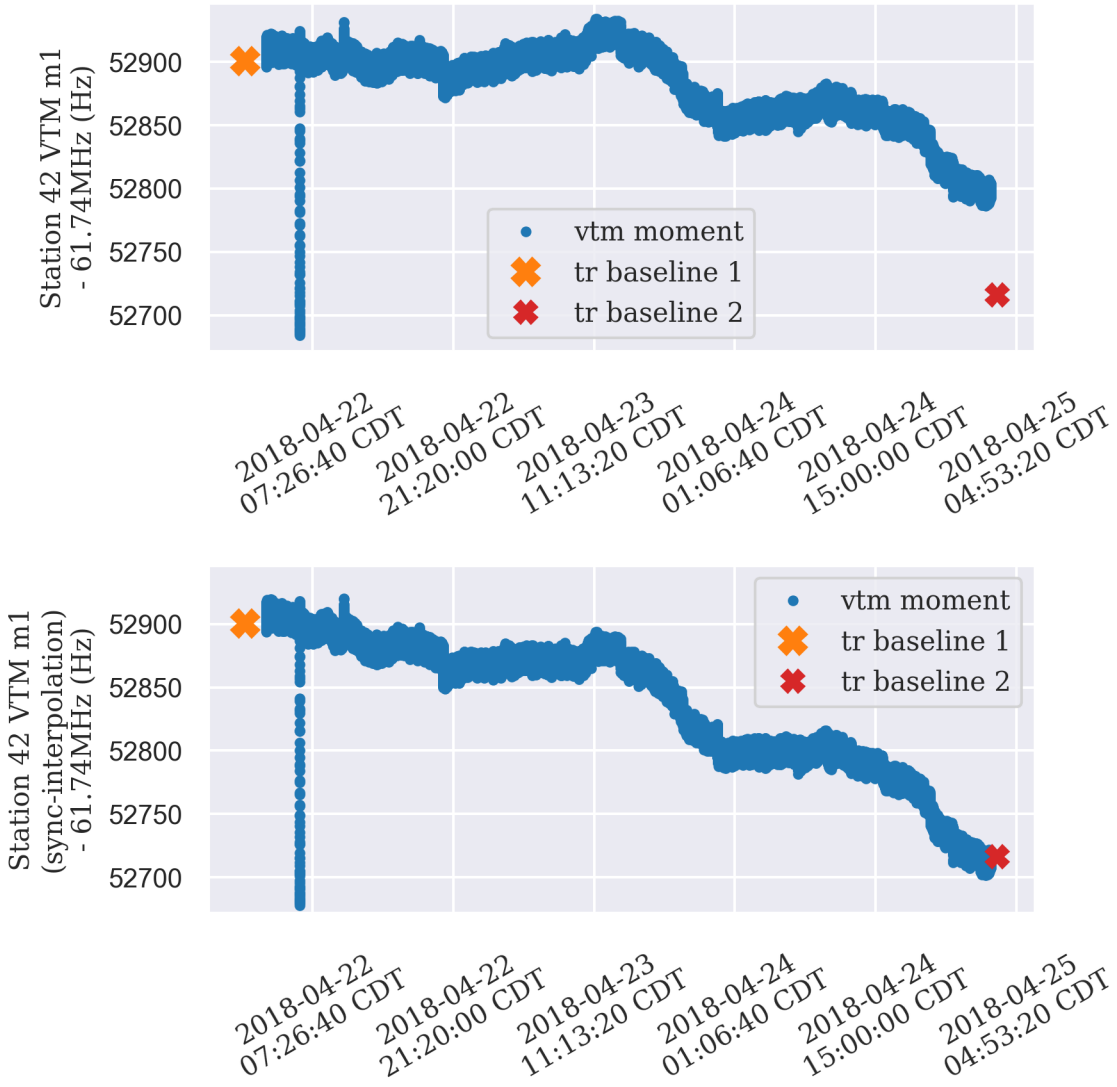

Figure 6.6: Sample virtual trolley measurements with the interpolated sync offset, along with sync values from both trolley runs.

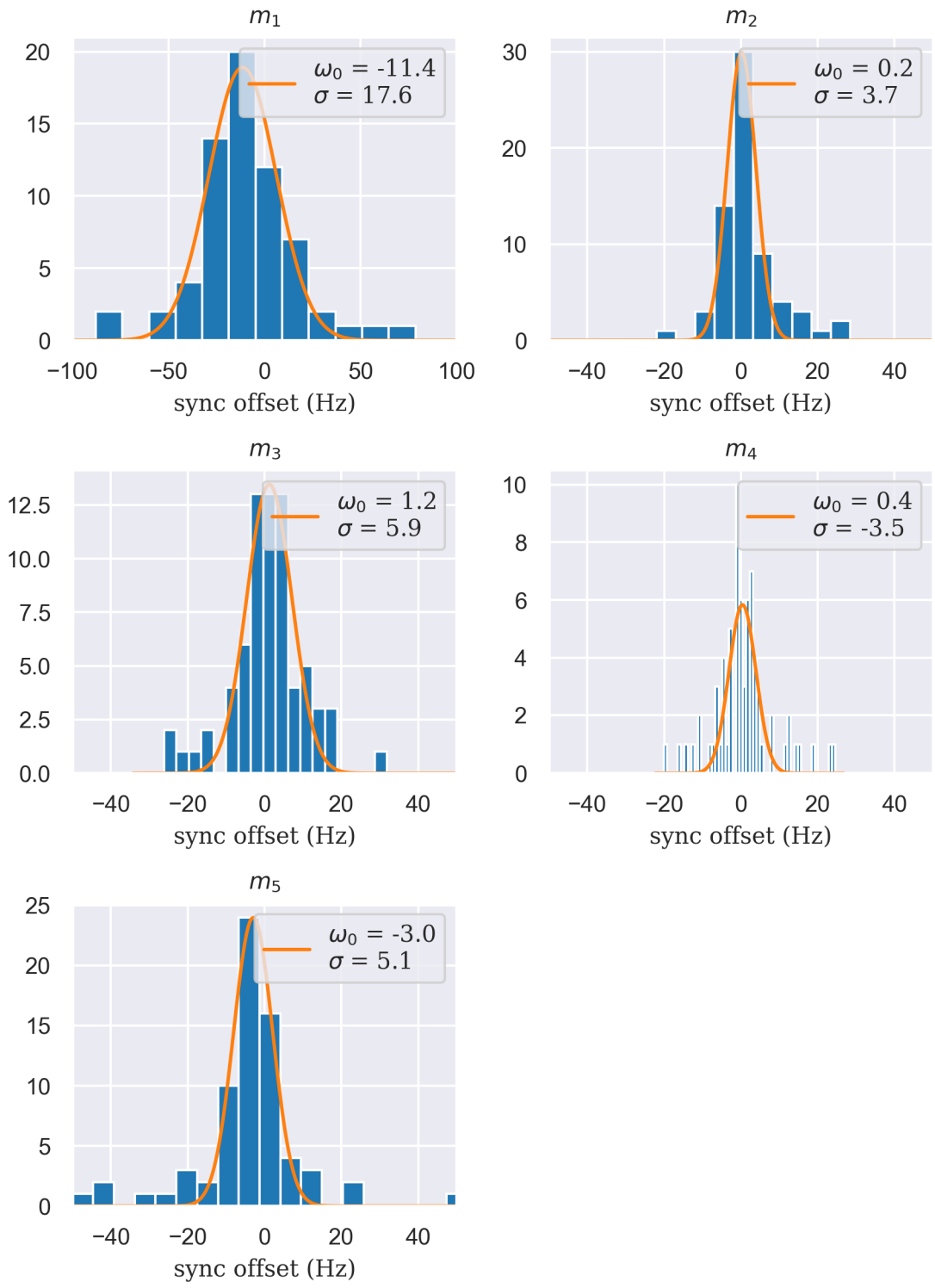

Figure 6.7: Histograms of the sync offset differences between the two trolley runs of the 60 hour data set.

CHAPTER VII

Muon-Weighted Averaging

An important question to ask before moving on with averaging the magnetic field is "How do the muons average the field?" To answer that, we begin with Equation 2.7 assuming that the term proportional to the electric field is zero (and assuming the field is entirely in the y-direction), so that

$$\omega_a = a_\mu \frac{e}{m} B. \tag{7.1}$$

A single muon will accumulate a phase as it travels around the ring until it decays at time T. The phase it has accumulated at this time is the integral of ω_a. Assuming that the field does not drift over the time T (a very good assumption with muon's mean lifetime of 64 us in the lab frame), the average frequency over its lifetime is

$$\langle \omega_a \rangle_k = a_\mu \frac{e}{m} \frac{1}{T} \int_0^T \mathrm{d}t \; B(\mathbf{r}_\mu(t)), \tag{7.2}$$

where $\mathbf{r}_\mu(t)$ is the muon's path as a function of time. The subscript k here indicates that this is a time average for the kth muon.

We want to convert this integral to being over azimuth instead of time, so we make a few substitutions, such that

$$\mathrm{d}t = \frac{\mathrm{d}l}{c} = \frac{r_\mu(\phi)\mathrm{d}\phi}{c} \implies T = \frac{R}{c}\Phi. \tag{7.3}$$

It is important to note that ϕ here is not bounded to $[0, 2\pi)$, and on average Φ will approach values of thousands of radians. We have introduced $r_\mu(\phi)$ as the radius of muon's path at a given azimuth, and then defined $R = \langle r_\mu \rangle$ as the radius averaged over ϕ. Making these substitutions, we can see

$$\langle \omega_a \rangle_1 = a_\mu \frac{e}{m} \frac{1}{R\Phi} \int_0^\Phi \mathrm{d}\phi \; B(\mathbf{r}_\mu(\phi)) r_\mu(\phi). \tag{7.4}$$

We can extend this integral to three dimensions by incorporating the muon path (in both the r and y axes) as delta functions, and integrating over r and $y$over the muon storage region. The exact limits of integration don't matter as long as they include the full path, so call the limits $y \in [-y_0, y_0]$ and $r \in [r_1, r_2]$.

$$\mathbf{r}_\mu(\phi) = \int_{r_1}^{r_2} \mathrm{d}r \int_{-y_0}^{y_0} \mathrm{d}y \delta(r - r_\mu(\phi)) \delta(y - y_\mu(\phi)). \tag{7.5}$$

These definitions allow us to rewrite the integral as

$$\langle \omega_a \rangle_k = a_\mu \frac{e}{m} \frac{1}{R\Phi} \int_0^\Phi \mathrm{d}\phi \int_{r_1}^{r_2} \mathrm{d}r \int_{-y_0}^{y_0} \mathrm{d}y \; rB(r, y, \phi) \delta(r - r_\mu(\phi)) \delta(y - y_\mu(\phi)). \tag{7.6}$$

Here all the information about the muon's path is encoded in the delta functions so the field map and volume element r can be integrated over 3D space. At this point, it becomes useful to split the integral over ϕ into a sum of integrals over single turns. These integrals are over $\phi \in [0, 2\pi)$ and are parametrized by n, the number of cycles the muon makes. The muon makes N total cycles, so we sum from $n = 0$ to $N - 1$.

$$\langle \omega_a \rangle_k = a_\mu \frac{e}{m} \sum_{n=0}^{N-1} \int_0^{2\pi} \mathrm{d}\phi \int_{r_1}^{r_2} \mathrm{d}r \int_{-y_0}^{y_0} \mathrm{d}y \; rB(r, y, \phi) \frac{1}{2\pi NR} \delta(r - r_\mu(2\pi n + \phi)) \delta(y - y_\mu(2\pi n + \phi)). \tag{7.7}$$

The only terms in the integral that depend on the parameter n are the delta functions, so we can pull the sum into the integral. This gives us

$$\langle \omega_a \rangle_k = a_\mu \frac{e}{m} \int_0^{2\pi} \mathrm{d}\phi \int_{r_1}^{r_2} \mathrm{d}r \int_{-y_0}^{y_0} \mathrm{d}y \; rB(r, y, \phi) \frac{1}{2\pi NR} \left(\sum_{n=0}^{N-1} \delta(r - r_\mu(2\pi n + \phi)) \delta(y - y_\mu(2\pi n + \phi)) \right). \tag{7.8}$$

This sum over delta functions is a distribution of the muon's position in the ring, so we write

$$\rho_k(r, y, \phi) = \frac{1}{2\pi NR} \left(\sum_{n=0}^{N-1} \delta(r - r_\mu(2\pi n + \phi)) \delta(y - y_\mu(2\pi n + \phi)) \right). \tag{7.9}$$

Note that this distribution is already normalized. It is a number density with units of inverse volume. Again, the subscript k indicates that this is the average distribution for the kth muon. However, it is easy to see how this generalizes to the case of an average over many muons. The field map is constant for all muons in a fill, so the only averaging in $\langle\omega_a\rangle_1 \rightarrow \langle\omega_a\rangle$ will be averaging the distributions ρ_k for each muon in the fill. It is useful here to only consider muons that will be included by the calorimeters (i.e., corrected for acceptance, cuts, etc.). Then, for a single fill, we have $\rho_k \rightarrow \rho_\mu$ and as the total number of muon-turns becomes very large, the distribution becomes continuous as the muons explore the storage region. The final result is an average over all of the muons in a fill, $\langle\omega_a\rangle$, where

$$\langle\omega_a\rangle = a_\mu \frac{e}{m} \int_0^{2\pi} \mathrm{d}\phi \int_{r_1}^{r_2} \mathrm{d}r \int_{-y_0}^{y_0} \mathrm{d}y \; r\rho_\mu(r, y, \phi) B(r, y, \phi). \tag{7.10}$$

Referencing Equation 7.10 as $\widetilde{\omega}'_p$, we can express the muon-weighed field average for a single fill at time t as

$$\tilde{B}(t) = \int_0^{2\pi} \mathrm{d}\phi \int_{r_1}^{r_2} \mathrm{d}r \int_{-y_0}^{y_0} \mathrm{d}y \; r\rho_\mu(r, y, \phi, t) B(r, y, \phi, t). \tag{7.11}$$

Note that $\rho_\mu(r, y, \phi, t)$ now has time dependence, and accordingly has units of inverse volume-time. We can then average over time for a full muon data set. Using the notation from Equation 3.5, we can rewrite B in terms of $\widetilde{\omega}_p$

$$\widetilde{\omega}'_p = \frac{\int \mathrm{d}\mathbf{r} \; \mathrm{d}t \; \omega'_p(\mathbf{r}, t)\rho_\mu(\mathbf{r}, t)}{\int \mathrm{d}\mathbf{r} \; \mathrm{d}t \; \rho_\mu(\mathbf{r}, t)} \tag{7.12}$$

where the integral is performed over the full storage volume and the time of a data set. This chapter lays out a framework for evaluating this integral. However, at the time of writing, the required inputs from the tracker calculations and from beam dynamics still works-in-progress by two other, separate teams within the collaboration, so only toy models have been used in the calculations so far.

Although it would be ideal to know $\rho_\mu(\mathbf{r}, t)$ exactly for all positions and times, the experiment is limited in how well it can measure the time and spatial evolution of the muon distribution. Because there are only two straw tracker stations installed in the ring, the azimuthal variation of the beam profile is difficult to study. Beam profiles from the straw tracker can be corroborated by simulations and beam dynamics calculations, which can provide a model for the azimuthal dependence of the muon beam. The time dependence of the muon distribution is drawn from the positrons counted by the calorimeters (CTAGs).

Periods that have high positron counts (and therefore higher statistical significance in the determination of ω_a) are weighted higher in the field average. The weights can also be set to zero for time periods that are cut from the data used in the ω_a analysis due to poor data quality, so $\widetilde{\omega}_p$ is only averaged over the same times that ω_a is averaged.

The muon distribution distribution time and spatial dependence can be factored and written as

$$\rho_\mu(\mathbf{r}, t) = T(t)\sigma(\theta, x, y), \tag{7.13}$$

factoring out the time dependence. Factored like this, σ is still a number density, while T is a prefactor normalizing σ to the number of detected decay positrons in a unit time with dimensions of inverse time. This form makes the assumption that the beam distribution is constant in time. This is a justified assumption to make because the time variation of the parameters of the beam vary slowly. Though not necessary, a generalization to the time-dependent case is discussed in Section 7.5. Splitting the muon distribution like this allows the time-dependent part of Equation 7.12 to be integrated first, then the spatial-dependence can be integrated.

7.1 Time Averaging

By assuming that the muon distribution can be factored as it is in Equation 7.13, the time integral in Equation 7.10 is relatively simple. Using the definition for ρ_μ in Equation 7.9

$$\widetilde{\omega}'_p = \int \mathrm{d}\mathbf{r} \frac{\int \mathrm{d}t\ \omega'_p(\mathbf{r}, t)T(t)}{\int \mathrm{d}t\ T(t)} \frac{\sigma(\theta, x, y)}{\int \mathrm{d}\mathbf{r}\ \sigma(\theta, x, y)}. \tag{7.14}$$

The first fraction in the above equation is the time-averaged field map weighted by the decay positron counts, which are binned by ω_a subruns generally about 10 seconds long.

$$\omega'^T_p(\mathbf{r}) = \frac{\int \mathrm{d}t\ \omega'_p(\mathbf{r}, t)T(t)}{\int \mathrm{d}t\ T(t)}. \tag{7.15}$$

Each station-wise field moment is binned into the same subrun time bins and then averaged. The subrun-average moments are weighted by the number of decay positron counts from the subrun, and averaged over the full data set (many subruns). The number of Counted TAGs (CTAGs) in a unit time $\frac{\mathrm{d}N}{\mathrm{d}t}$ is proportional to the number of muons present in the ring at that time. This method makes data quality cuts easy, as any subruns that are rejected from the ω_a analysis, including rejections due to field events, can be omitted from the field average by just not including those times in the binned moments. This is equivalent to setting the

weight $T(t)$ for those times to zero.

Using this definition of the time-averaged field map, Equation 7.10 is reduced to the purely-spatial integral

$$\widetilde{\omega}'_p = \frac{\int \mathrm{d}\mathbf{r}\, \omega'^T_p(\mathbf{r}) \times \sigma(\mathbf{r})}{\int \mathrm{d}\mathbf{r}\, \sigma(\mathbf{r})}. \tag{7.16}$$

7.2 Beam Profile Model

Much like the field moments, the beam profile can be considered 2D slices in azimuth. The 2D muon distributions can be simulated, analytically calculated, or measured by the straw trackers. Taking a cue from the field map, it is convenient to consider the muon distribution in terms of its moments. The first four moments are the x and y centroids, and the x and y widths. Higher order moments, such as the skew, kurtosis, and$x-y$ covariant parameters can also be considered, but in general are harder to calculate. Instead, we can use the first four moments in a fit to the distribution. Figure 7.1 shows the 2D profile measured by tracker station 12, the parametrized fit, and the residuals.

In Figure 7.1, the function used to fit the beam profile is

$$\begin{aligned}\sigma(x,y) = A\exp\left(-\frac{(y-y_0)^2}{2s_y^2}\right) \times \\ \left[A_1\exp\left(-\frac{(x-x_1)^2}{2s_{x1}^2}\right) + A_2\exp\left(-\frac{(x-x_2)^2}{2s_{x2}^2}\right) + A_3\exp\left(-\frac{(x-x_3)^2}{2s_{x3}^2}\right)\right].\end{aligned} \tag{7.17}$$

The relationship between many of the coefficients, such as the ratio $\frac{x_3-x_2}{x_2-x_1}$ (assuming $x_3 > x_2 > x_1$), are fixed by fitting the function to the measured beam profile. Only scale factors that control the overall x and positions, x and y widths, and total amplitude, while preserving the shape, are left as free parameters. These five free parameters roughly correspond to the moments of the beam mentioned above. The specific form of Equation 7.17 is not important. Further studies are required to determine the effect of any chosen parameterization on the averaging scheme. In general, the only important part is to define the function in such a way that the azimuthal dependence of the beam moment parameters can be estimated by beam dynamics studies and simulations. Then a generic parameterization could be written

$$\sigma(\phi, x, y) = \sigma(x, y, C_1(\phi), C_2(\phi), ...) \tag{7.18}$$

where the C_n are the beam moment parameters.

An important future step in the tracker analysis is to correct for the *acceptance* of the

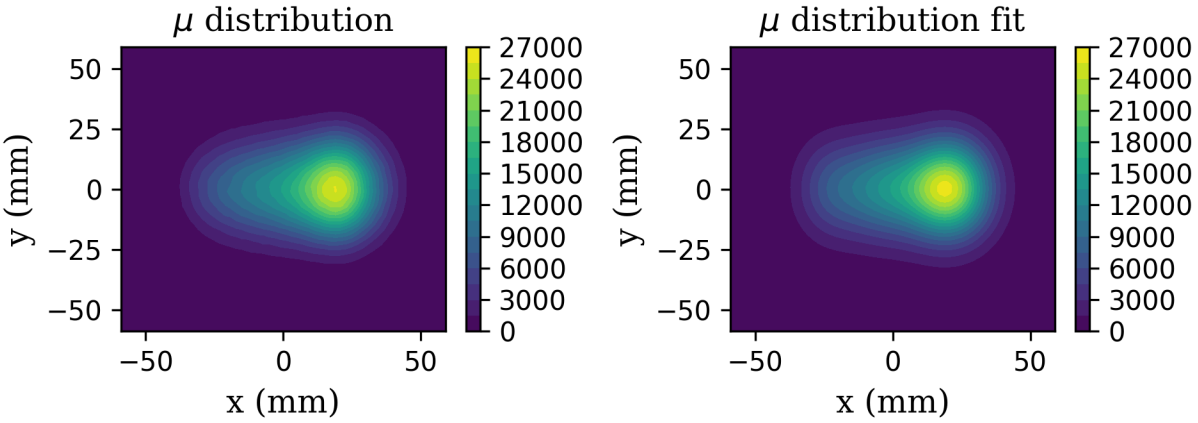

(a) Left: The beam profile from the trackers. Right: A four parameter fit to the profile. The underlying function is a gaussian in the y direction times a sum of three gaussians in the x direction. Many of the arguments to the x gaussian are constrained by training the fit parameters on the real distribution. This fitting function is only a sample, and subject to future change. The color scale shows detected decay positron counts.

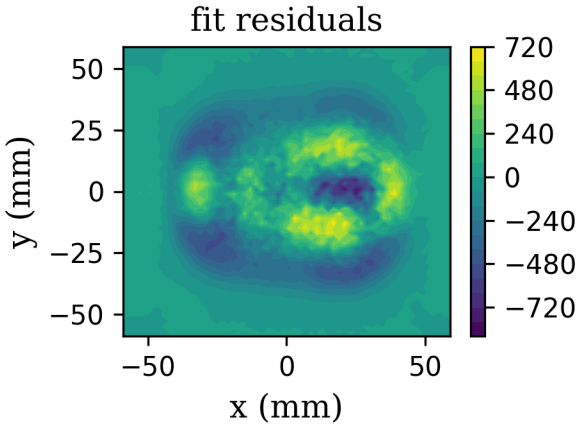

(b) The residuals of the four parameter fit.

Figure 7.1: The measured and fit beam profile. The fit takes four parameters, the x and y centroids, and the x and y widths. Note that the residual is less than 5% of the maximum.

calorimeters. Only decay positrons that both hit a calorimeter and meet the energy threshold are used in the ω_a analysis. Therefore, we only want to know about the distribution of the muons that produced those positrons. The acceptance correction for the tracker analysis is underway at the time of writing.

7.3 Azimuthal Dependence of the Muon Distribution

We can extend the 2D distribution into a 3D distribution by writing the beam moments as functions of azimuth, similar to the treatment of the magnetic field moments. The azimuthal dependence of the centroid and widths are both known beam dynamics phenomena called the closed orbit distortion and beta functions, respectively.

Closed Orbit Distortion

The ideal muon orbit is a 7.112 m circle centered at the center of the storage ring, so that the muon is always at the same radial position. Variations in the injected muon momentum and the various focusing fields cause the muons to "swim" around the central orbit, but most of these excursions are not in phase with the full path around the ring and average out over all the muons and all the revolutions. Excursions that do not average out over the muon distribution and lifetime create *closed orbit distortions*. These can be thought of as azimuthally-dependent variations in the centroid of the muon 2D profile. Because they are periodic, it is convenient to consider them as a Fourier series. Then, the $N = 0$ term is the mean radius of the orbits. The $N = 1$ term is the lowest-order distortion from the ideal orbit. It corresponds to a shift in the center of the circular orbit from the center of the ring while the radius (from the new center) remains constant in azimuth. Higher order terms in the Fourier expansion correspond to perturbations from the circular orbit (see Figure 7.2 for example closed orbits).

Beta Function Breathing

The beta functions encode information about the width of the beam as it travels around the ring, undergoing focusing by the magnetic and electric fields. The electrostatic quadrupoles focus the beam vertically and defocus it horizontally. The vertical distribution is narrowest between the quadrupoles and widest in their center. Conversely, the horizontal width is widest between the quads and narrowest in their center. There are four quad stations distributed evenly around the ring, which causes the widths to vary around the ring with

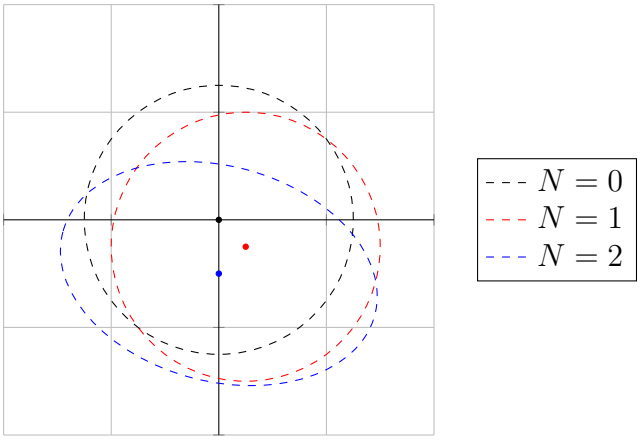

Figure 7.2: Example closed orbits, labeled by N, the highest-order non-zero Fourier term. Note that the $N = 1$ term is just a displacement of the circular orbit.

harmonics of the $N = 4$ period. Sample beta functions (which are proportional to the square of the width) are shown in Figure 7.3.

7.4 3D Integration

With analytical expression for both the 3D muon distribution and magnetic field map, we can solve the spatial integral of Equation 7.16. By defining analytic functions for the field and distribution over x, y, θ, standard N-dimensional quadrature techniques can be used. The definition of the field map uses the definition of the multipoles (see Section 5.1),

$$B_y = A_0 + \sum_{n=1} A_n \left(\frac{r}{r_0}\right)^n \cos(n\theta) + B_n \left(\frac{r}{r_0}\right)^n \sin(n\theta). \tag{7.19}$$

Making assumption that the higher order multipoles integrate to small values when weighted by the highly-symmetric 2D beam profile, the analytic equation for the field map is

$$\omega_p'^T(\phi, r, \theta) = m_1(\phi) + \left(\frac{r}{4.5\text{ cm}}\right)[m_2(\phi)\cos(\theta) + m_3(\phi)\sin(\theta)] + \left(\frac{r}{4.5\text{ cm}}\right)^2 [m_4(\phi)\sin(2\theta) + m_5(\phi)\cos(2\theta)]\,. \tag{7.20}$$

Here, we have considered the moments $m_1(\phi)$ through $m_5(\phi)$ to encode all the azimuthal dependence of the field, and the azimuthal dependence is evaluated from the 72 fixed probe stations distributed around the ring. The moments in this case are also given in units of Hz, corresponding to the calibrated frequencies of the NMR probes. Note that r and θ are the polar coordinates corresponding to x and y in a 2D slice.

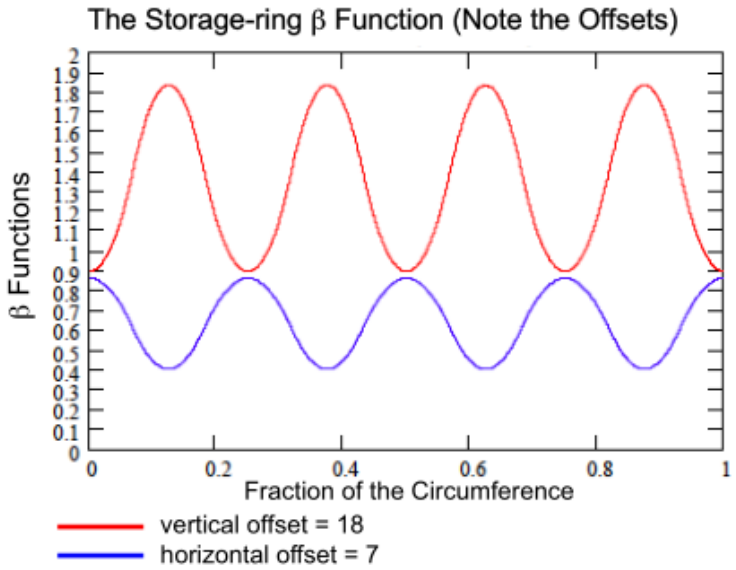

Figure 7.3: The beta functions from E821, reproduced from [40]. The beta functions show how the width of the beam profile varies around the ring.

The analytic function for the muon distribution is constructed by providing azimuthally dependent arguments to the fit shown in Figure 7.1. The arguments will be provided by beam dynamics and simulations. With both analytic functions defined, the integrals in Equation 7.16 are evaluated numerically, and is

$$\widetilde{\omega}'_p = \frac{\int_0^{2\pi} \mathrm{d}\phi \int_{r_1}^{r_2} \mathrm{d}r \int_{-y_0}^{y_0} \mathrm{d}y \; r\omega_p'^T(\phi, r, y)\sigma(\phi, r, y)}{\int_0^{2\pi} \mathrm{d}\phi \int_{r_1}^{r_2} \mathrm{d}r \int_{-y_0}^{y_0} \mathrm{d}y \; r\sigma(\phi, r, y)}, \tag{7.21}$$

where $\omega_p'^T$ is defined in terms of the magnetic field moments in Equation 7.20 and σ is defined in terms of beam shape parameters, such as in Equation 7.18.

7.5 Generalization to the Time-Dependent Beam Profile

The generalization to the case of significant know time dependence of the muon distribution could be performed similarly, beginning from Equation 7.10. Instead of the integration over time being done over the full data set, however, it would be done over time bins corresponding to known closed-orbit averages, or times over which the closed orbit does not drift considerably. This would modify Equation 7.14 into

$$\widetilde{\omega}'_p = \sum_{n=0}^{T_{max}} \int \mathrm{d}\mathbf{r} \frac{\int_{T_n}^{T_{n+1}} \mathrm{d}t \; \omega'_p(\mathbf{r}, t) T_n(t)}{\int_{T_n}^{T_{n+1}} \mathrm{d}t \; T_n(t)} \frac{\sigma_n(\theta, x, y)}{\int \mathrm{d}\mathbf{r} \; \sigma_n(\theta, x, y)}. \tag{7.22}$$

In each of these time bins, indexed by n, the beam profile σ_n would be different, but the method to calculate the integrals would be the same. We would calculate an $\widetilde{\omega}_p$ for each bin, which we would then average over time to calculate the value for the full data set.

Alternatively, the time dependence could be added to the analytic functions described in Section 7.4 and then the average could be calculated by 4-dimensional quadrature. This method would drastically increase the time required for computation, and require careful consideration to fold in the number of muons in the beam at any given time, determined by the CTAGs, but nevertheless provides a strong candidate for a high-precision calculation in the future.

CHAPTER VIII

Systematic Corrections and Uncertainties

The analysis approach presented in the dissertation can effectively estimate the first five moments of the field as a function of time, with an eye towards time averaging over full data sets in the future. This chapter covers the statistical and systematic uncertainties involved in these estimates. Unless otherwise noted, the uncertainties quoted are averaged over time for the full named data set.

It is useful to break the uncertainties into three types: Type A, Type B, and "Type A/B." Types A and B are commonly used terms, and roughly correspond to statistical and systematic uncertainties, respectively [46]. A better way to think of them is as uncertainties that improve with more measurements and those that don't. These definitions lead to our definition of "Type A/B," which are uncertainties that would improve with more trolley runs, but are limited by the rate trolley runs can be performed.

Type A uncertainties for the field analysis consist mainly of the single measurement uncertainties of the NMR probes. Even the noisiest probes (the ones in stations 1, 3, and 5) can produce useful data if they are averaged for long enough periods of time. The Type A/B uncertainties are mainly encoded in the measurement of the sync offset. This term includes uncertainties caused by higher-order gradient drift, probe position errors, and other time dependent drifts. Type B uncertainties consist of uncertainties in the trolley measurements, and measurements further up the calibration chain (in the plunging and absolute probes). They also include some analytic choices in the interpolation analysis like the trolley footprint removal.

8.1 Trolley Systematics

The trolley systematics fall into either Type B or Type A/B uncertainties because they are mostly caused by uncertainty in the trolley's position and the trolley's physical motion during data taking. All the uncertainties here are classified by their effect on the naive

Source	Uncertainty (Hz)	Uncertainty (ppb)
Frequency extraction	0.3	5
Trolley probe offset	0.74	12
Azimuthal position	0.3	5
xy position (m_1)	0.6	10
xy position ($m_2,\ m_5$)	1.5	26
xy position ($m_3,\ m_4$)	0.2	2
Trolley spikes	0.3	5
Other motional effects	<1.2	<20
Total (m_1)	1.6	26
Total ($m_2,\ m_5$)	2.9	47
Total ($m_3,\ m_4$)	1.5	25

Table 8.1: The trolley systematic uncertainties by source for Run 1.

azimuthal average of the field map. Table 8.1 summarizes the sources and their respective uncertainties. The entries are discussed in the following sections. Note that several sources of uncertainty are estimated based on a collaborator's work and are describe in internal documents as referenced.

8.1.1 Trolley Probe Offsets

Uncertainties in the plunging probe calibrations and trolley probe offsets are estimated to be about $\sigma_{\omega^{\mathrm{tr}}} = 2.5$ Hz (40 ppb) in each offset [47]. The uncertainties are averaged into the first three moments by the number of trolley probes used in each moment calculation, given by

$$\sigma_{m_1^{\mathrm{tr}}} = \frac{1}{\sqrt{13}}\sigma_{\omega^{\mathrm{tr}}} = 0.69 \text{ Hz} = 11.1 \text{ ppb}, \tag{8.1}$$

$$\sigma_{m_2^{\mathrm{tr}}} = \frac{1}{\sqrt{12}}\sigma_{\omega^{\mathrm{tr}}} = 0.71 \text{ Hz} = 11.5 \text{ ppb}, \tag{8.2}$$

$$\sigma_{m_3^{\mathrm{tr}}} = \frac{1}{\sqrt{12}}\sigma_{\omega^{\mathrm{tr}}} = 0.71 \text{ Hz} = 11.5 \text{ ppb}. \tag{8.3}$$

We therefore assign a conservative estimate of 0.74 Hz (12 ppb) to uncertainty from the plunging probe calibrations for m_1, m_2, and m_3. The goal for the plunging probe analysis is the achieve better than 30 ppb uncertainty per trolley probe [48], which would reduce the estimate of the uncertainty of the moments to under 10 ppb. It should be noted that there is an absolute offset blind, common to all the probes. This means that m_1 is blinded, but not the higher order moments. The scale of the blind is currently 100 ppb.

8.1.2 Trolley Azimuthal Position

There is an uncertainty in the position of the trolley recorded during each trolley NMR measurement. This causes an uncertainty in the azimuthal average of the field. The azimuthal average for non-uniform sampling is

$$\frac{\sum \omega_i \Delta\phi_i}{\sum \Delta\phi_i} = \frac{\sum \omega_i \Delta z_i}{\sum \Delta z_i}. \tag{8.4}$$

The systematic uncertainty arises because of the position uncertainty combined with the azimuthal gradient. Assuming an azimuthal gradient $\frac{dB_y}{dz} \leq 0.5$ ppm/mm, chosen from the RMS gradient calculated during a typical trolley run and the RMS azimuthal position uncertainty $\delta_{rms}\Delta z \approx 0.1$ mm, the azimuthal average uncertainty is 50 ppb (3 Hz).

A more detailed estimate based on Monte Carlo studies [44] has been built on this estimation technique. The estimate for the uncertainty in the azimuthal average caused by uncertainty in the trolley position is 0.3 Hz, or 5 ppb.

8.1.3 Trolley Spikes

Trolley spikes are rapid changes of the frequency related to trolley motion measured by trolley probes that are not due to azimuthal field variations. The current hypothesis is that they are due to eddy currents induced by changes in the trolley orientation and motion in the azimuthal gradient. This systematic is under continued study. A study that compare moving trolley runs to "start-stop" trolley runs is planned. Analysis of such a study is ongoing for motion over a quarter of the ring from the trolley garage to the trolley drive.

For current purposes, we estimate the error based on a study [49] that analyzes outlier frequencies defined by a variable threshold and compares clockwise (CW) and counterclockwise (CCW) trolley runs to separate spikes from azimuthal variations of the field. Figure 8.1 shows a sample of the appearance of the spikes as a function of azimuth, and figure 8.2 shows the effect on the azimuthal average of each trolley probe. Further Monte Carlo simulations based on analysis suggest a realistic estimate of the systematic uncertainty from the trolley spikes is 0.3 Hz (5 ppb) [44].

8.1.4 Frequency Extraction

The trolley frequency extraction is more precise than the fixed probes because the gradients in the center of the vacuum chamber are lower, resulting in longer T_2^*; however, the trolley spikes lead to larger gradients and shorter T_2^*. The statistical uncertainty per shot is less than 1 Hz, but estimates from initial simulations suggest that a ceiling on RMS varia-

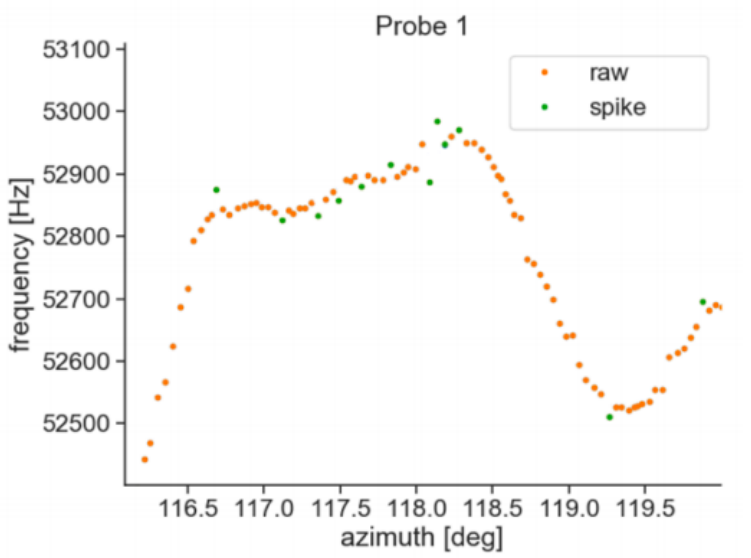

Figure 8.1: Sample spikes in trolley probe 1. Spikes are determined by being over a threshold compared to the value predicted by interpolating their nearest neighbors. Figure courtesy of S. Corrodi.

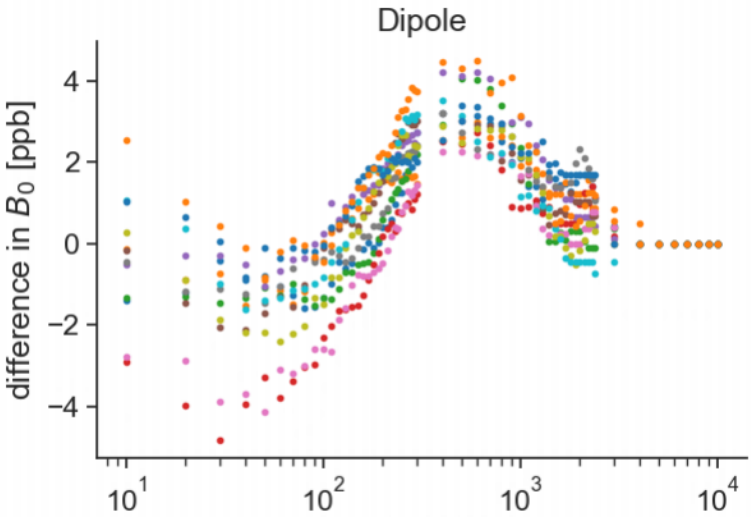

Figure 8.2: The azimuthally averaged (summed) error caused by trolley spikes, as a function of the threshold in the definition of a trolley spike. Each color represents a separate trolley NMR probe. Figure courtesy of S. Corrodi.

tions of 1 Hz (16 ppb) is reasonable [50]. Further work using the same method of simulated FIDs in gradient fields have corroborated this estimate, and found a reasonable average to be 0.3 Hz (5 ppb) [51]. Each fixed probe station is synchronized to trolley data from about 2.5 deg on each side of the station, which is approximately 80 independent measurements. This reduces the average value to less than 0.06 Hz (<1 ppb).

8.1.5 Trolley X-Y Displacement

The trolley's rails' radial and vertical positions depend on azimuth, an effect we call the "swimming trolley". As the trolley moves around the ring, the displacement of the trolley couples to the radial and vertical gradients of the field (the higher order moments) as

$$\frac{dB}{dx}\delta_{rms}(x) \tag{8.5}$$

and similarly for the y gradient. From Figure 8.3 and Figure 8.4, we estimate

$$\frac{dB}{dx} \leq 2 \text{ ppm}/4.5 \text{ cm} \tag{8.6}$$

and $\delta_{rms}x \approx 0.5$ mm resulting in a systematic error of 11 ppb or 0.7 Hz.

Further refinement of this method of analysis includes effects from higher-order moments aliasing into the lower-order moments, and the effects on the higher-order moment measurements themselves [44]. This study concludes that the uncertainty on the average field m_1 is 0.61 Hz (10 ppb). The uncertainty on m_2 through m_5, respectively, are 1.5 Hz, 0.1 Hz, 1.2 Hz, and 0.2 Hz. These uncertainties could be corrected with further surveys, but are small enough compared to the current uncertainties from other systematic effects that corrections would not significantly improve the final result.

8.1.6 Other Motional Effects

There are ongoing systematic studies into the effect on the trolley measurements caused by the trolley moving as it takes data. By comparing field maps generated during continuous-motion runs versus special "stepper" runs where the trolley is moved then stopped as it measures, we can estimate the uncertainty caused by any other effects included by trolley motion. Efforts are ongoing in the trolley analysis team to analyze and interpret these studies, but a conservative estimate is less than 20 ppb on the azimuthal average [44]. Further analysis is needed at this time, as this is the dominant source of uncertainty in the trolley systematic analysis.

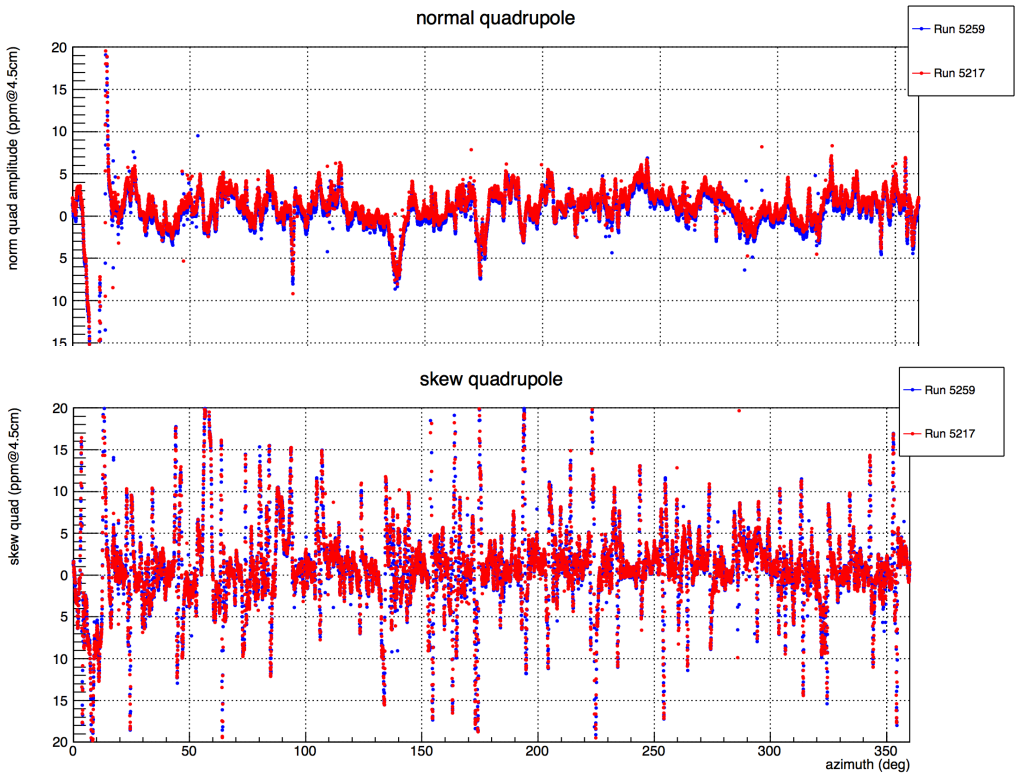

Figure 8.3: The radial and vertical gradients (normal and skew quadrupoles) couple with the trolley's xy position uncertainty. Figure courtesy of J. Grange.

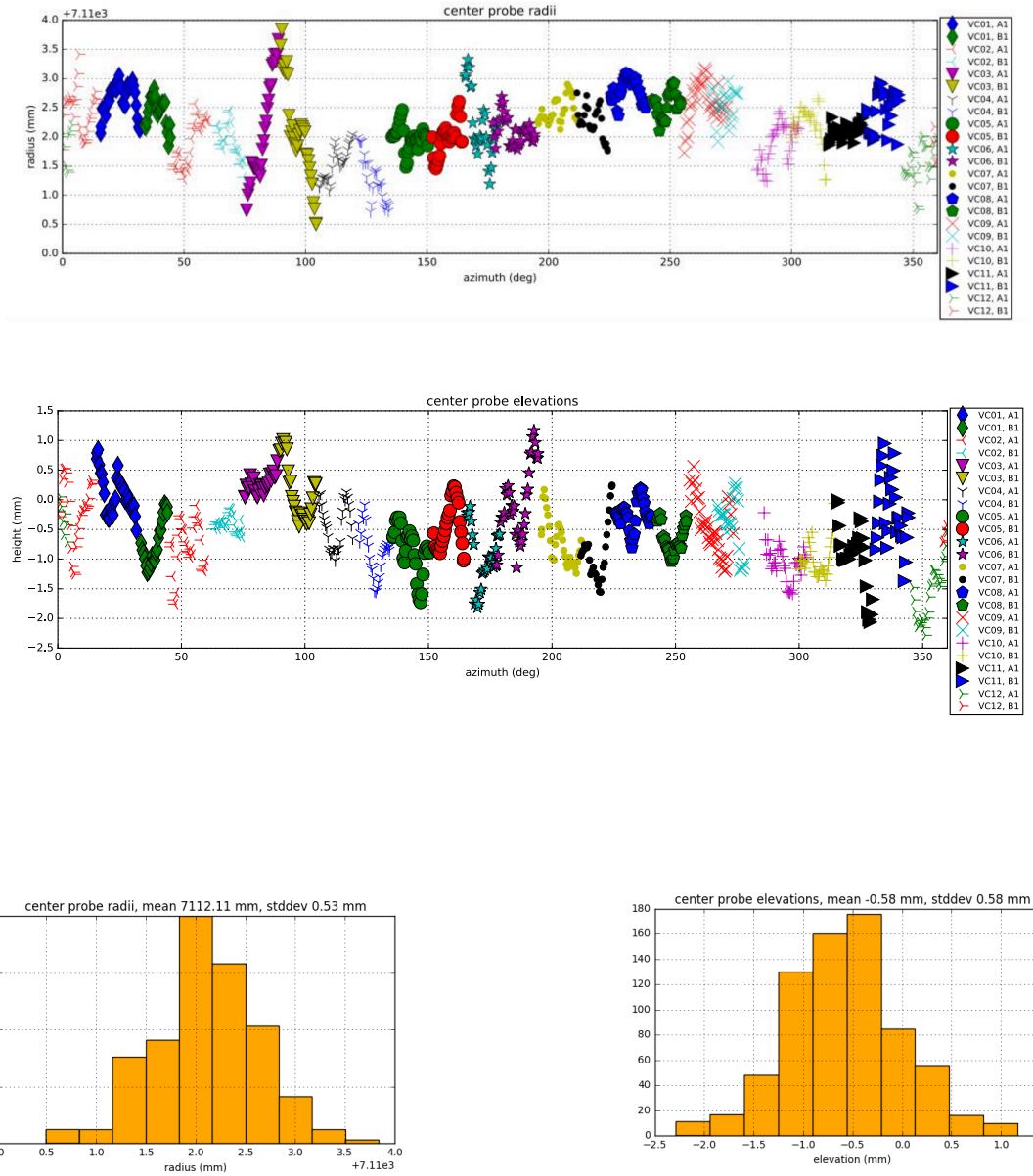

Figure 8.4: The surveyed excursions of the trolley from the muon ideal radius. Uncertainty caused by the "swimming trolley" couples with the vertical and horizontal gradients. Figures courtesy of J. Grange.

8.2 Fixed Probe Systematics

The uncertainty caused by the fixed probes is a Type A uncertainty, so it decreases as measurement time increases. The frequency noise (instability) was estimated from a time series of FIDs that was assumed to have drift accurately parameterized by a 2nd-order polynomial.The residuals from the fit were plotted as a histogram. The histogram was fit to a gaussian that was found to have a width of 60 ppb, which is taken as an estimate of the single shot noise from a single fixed probe. Assuming that the 378 probes have uncorrelated uncertainties and are azimuthally-averaged, it takes only 10 sequential measurements of each probe, or approximately 15 seconds, to reduce the uncertainty caused by the uncertainty on the average of the fixed probe measurements to less than 1 ppb. Considering that the shortest data sets are on the order of several days, this source of uncertainty is well below other systematic effects in Table 8.1 and can be neglected.

8.3 Interpolation Systematics

8.3.1 Interpolation to Time Grid

The time-grid interpolation step is not a significant source of uncertainty beyond the uncertainty from the fixed probe noise itself. This is because the time-grid interpolation step preserves averaging, as discussed in Chapter VI. Because the final result will always be averaged over time and the average of the interpolated points equals the average of the raw data over the same time (by construction), the uncertainty on the time-averaged interpolated point is the same as the uncertainty on time-averaged raw data points, which were discussed in Sections 8.1 and 8.2.

8.3.2 Trolley Footprint Replacement

The trolley's magnetic footprint must be removed from the fixed probe measurements during a trolley run before the fixed probe station can be averaged to find a baseline using the procedure is outlined in Chapter VI. To understand the systematic uncertainty caused by this procedure, a study was performed using measurements from a fixed probe run (no trolley present) and analyzed it as though it were a trolley run. The trolley footprint replacement procedure was performed on the fixed probe data, and the replacement data set was compared to the input data set, as in Figure 8.5.

By performing this study on every station in many input data sets with random simulated trolley positions, we can histogram the differences between the baseline values from the replacement data set and the baseline values from the actual data set. Results for the m_1

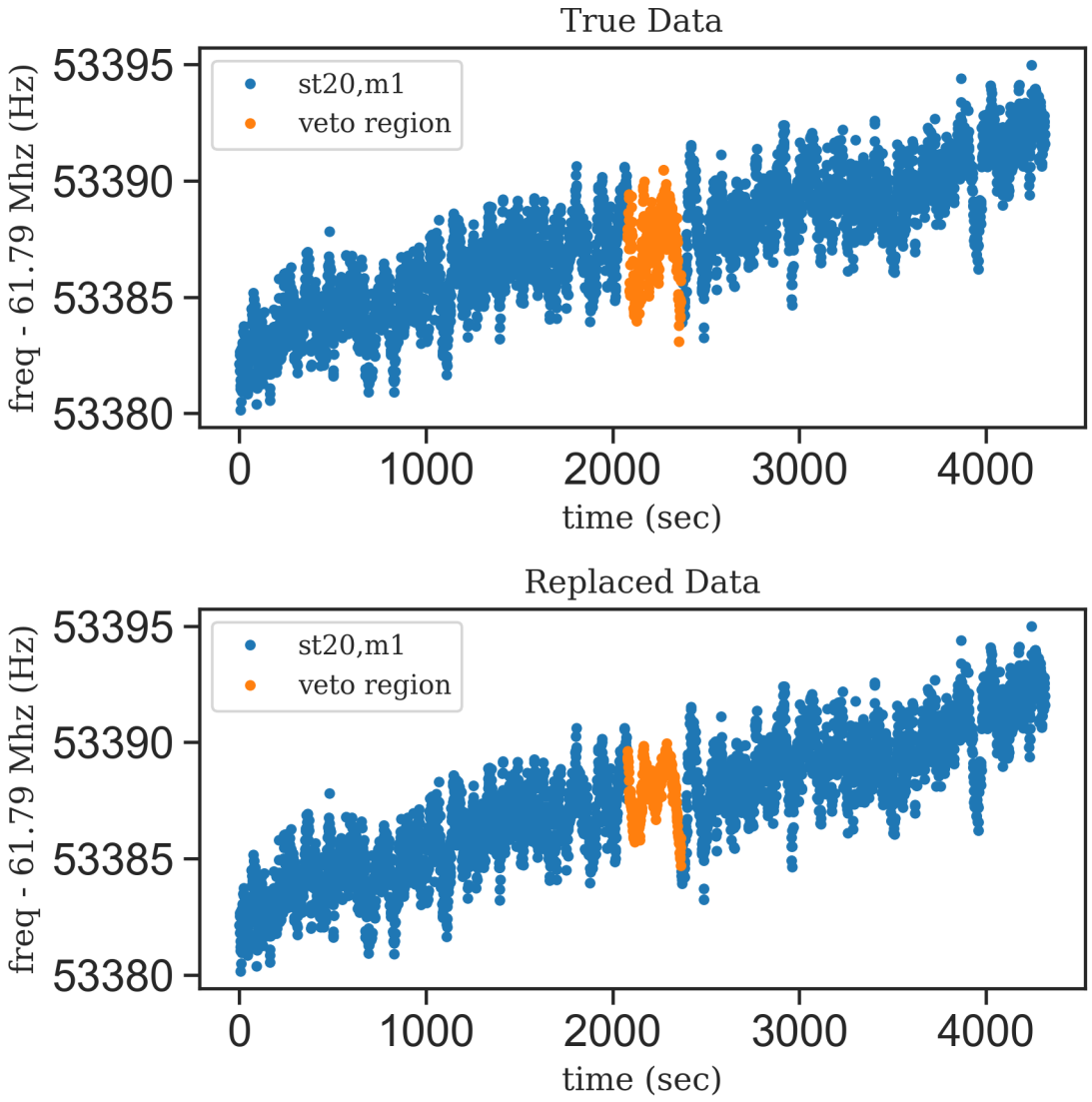

Figure 8.5: Top: Raw data taken from a fixed probe run and analyzed as a (fake) trolley run. The orange section shows the vetoed region. Bottom: The same data after running through the trolley footprint replacement algorithm. Note the similarities in the orange region.

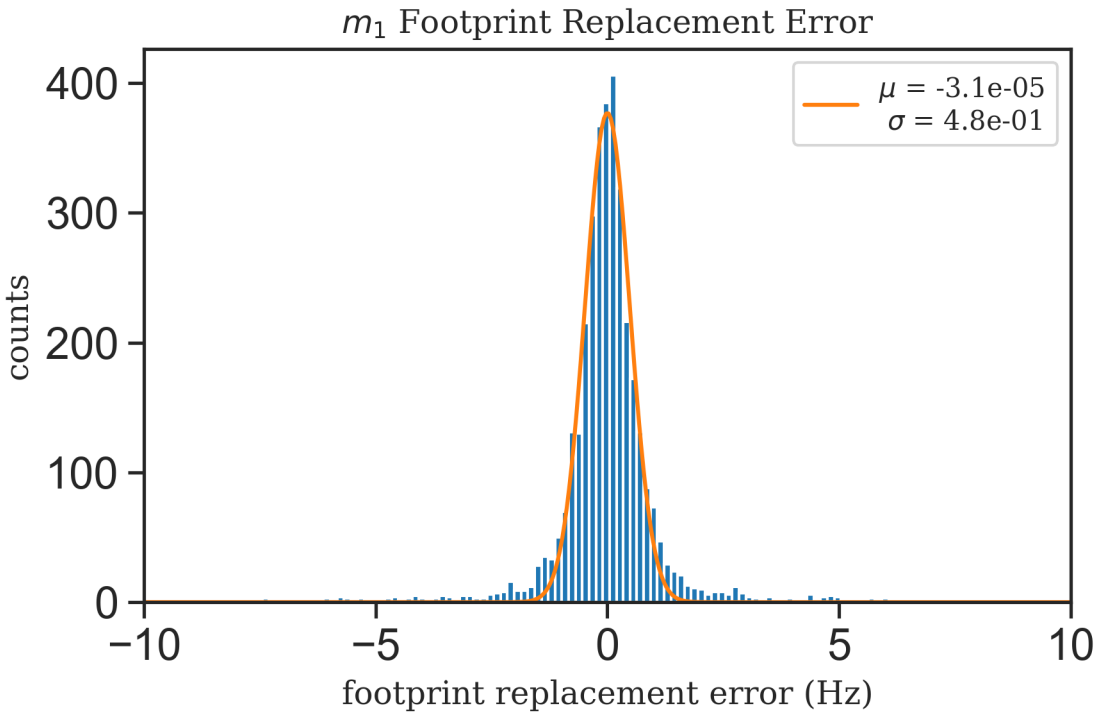

Figure 8.6: A histogram of the errors from averaging the m_1 trolley footprint replacement over 3600 differences. Note that the error of the mean is 0.48 Hz/$\sqrt{3600}$ = 0.008 Hz, so the mean of the distribution is consistent with zero.

baseline different for $N = 50$ (3600 points) are shown in Figure 8.6. The same systematic study can be performed on the higher order moments as well, as shown in Figure 8.7.

The centers of all five distributions are consistent with zero (see Figure 8.6), indicating that the footprint replacement algorithm does not bias the results in either direction when averaged over all 72 stations. We use the widths of the distributions as an estimate for the uncertainty on the trolley footprint replacement. See Table 8.2 for the values.

8.3.3 Higher-Order Drifts

Trolley probe and fixed probe moments are synchronized during a trolley run, but the magnetic field gradient drifts change the relationship between the synchronized $\mathbf{m}^{\mathrm{tr}}(0)$ and $\mathbf{m}^{\mathrm{fp}}(0)$ values due to aliasing of higher-order gradients into the tracked fixed probe moments. The amount that the trolley and fixed probes have drifted out of sync between two trolley runs is the *sync offset* described in Chapter VI. The sync offset is the value $\mathbf{c}_2 - \mathbf{c}_1$ in Equation 6.4. The distribution of the sync offsets from each station for each moment provides information about how the higher-order field gradients have changed over the course of the fixed probe run.

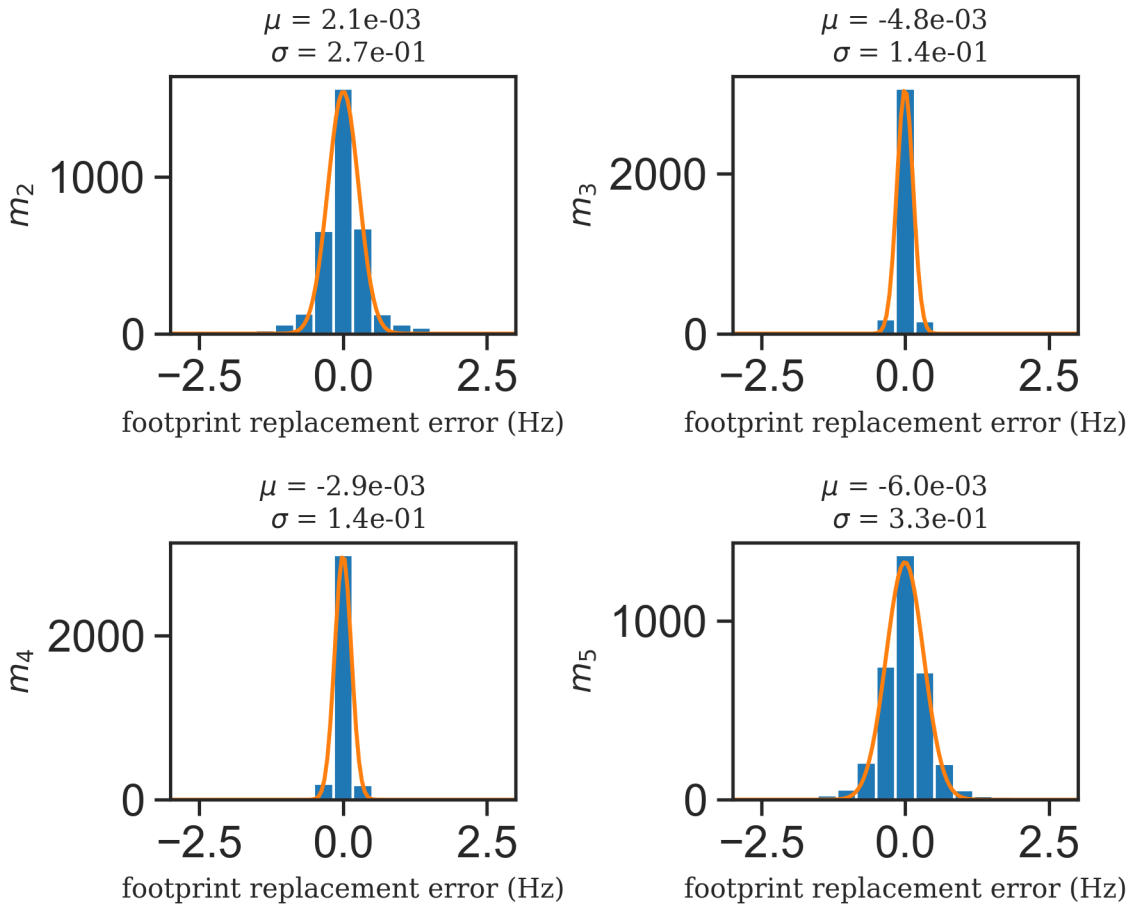

Figure 8.7: A histogram of the errors from averaging the m_2 through m_5 trolley footprint replacement over 3600 differences.

Moment	Uncertainty (Hz)	Uncertainty (ppb)
m_1	0.48	7.8
m_2	0.27	4.4
m_3	0.14	2.3
m_4	0.14	2.3
m_5	0.33	5.3

Table 8.2: The systematic uncertainty caused by the trolley footprint replacement procedure assigned to each of the first five moments. Note that this is a very conservative estimate for the uncertainty of this step because it does not include the expect factor of $\sqrt{72}$ from averaging the 72 stations. No assumption about the correlation (or lack thereof) of each station is made.

Since we do not know how the gradients are changing between trolley runs, we model the error by assuming the sync-offset results from a random walk, which is a conservative assumption regarding how the sync offset can change as a function of time between trolley runs. During a random walk, the variance increases linearly with time, leading to

$$d\sigma^2 = \Delta M^2 \left(\frac{t}{T}\right). \tag{8.7}$$

where ΔM^2 is the variance at the second trolley run at time T. Using the azimuthal average of the sync offsets from the second trolley run to estimate ΔM^2, the average uncertainty over the data run can be calculated.

$$\left\langle \sigma^2 \right\rangle = \frac{1}{T}\int_0^T \mathrm{d}t\ \Delta M^2 \frac{t}{T} = \frac{\Delta M^2}{2}. \tag{8.8}$$

The previous result assumes that the interpolation is only pinned to the first trolley run. However, ideally fixed probe runs are synced at both trolley runs, leading to nominally zero uncertainties near each trolley run and a larger uncertainty between them. This situation can be conservatively modeled as the uncertainties increasing linearly in time as the field performs a random walk forward in time from the first trolley run. However, it is also increasing in a similar fashion backwards in time from the second trolley run. The two walks meet at a maximum in the center of the fixed probe run with a maximum uncertainty $d\sigma^2 = \Delta M^2/2$. The average uncertainty for the interval T in this case is

$$\left\langle \sigma^2 \right\rangle = \frac{2}{T}\int_0^{T/2} \mathrm{d}t\ \Delta M^2 \frac{t}{T} = \frac{\Delta M^2}{4}. \tag{8.9}$$

The sync offsets from the 60 hour data set are shown in Figure 8.8. Using the mean of the sync offsets to estimate the azimuthally averaged ΔM^2 for m_1, we arrive at the uncertainty caused by the higher-order gradient drift. Using the formula for forwards-backwards interpolation, $\langle \sigma_{m_1} \rangle = \sqrt{\Delta M^2_{m_1}}/2 = 5.12$ Hz. A similar procedure is applied to each of the other moments tracked by the fixed probes. The result for the 60 hour data set are summarized in Table 8.3.

It is important to note that this systematic uncertainty includes the effects from many different sources. Because each fixed probe station is synchronized to an average from the trolley of approximately 5 deg, the sync offsets encode not just drift in vertical and radial gradients, but also azimuthal gradients. This includes uncertainty caused by differential drift around the ring. Consider the field map generated by a trolley run for the m_1 moment.

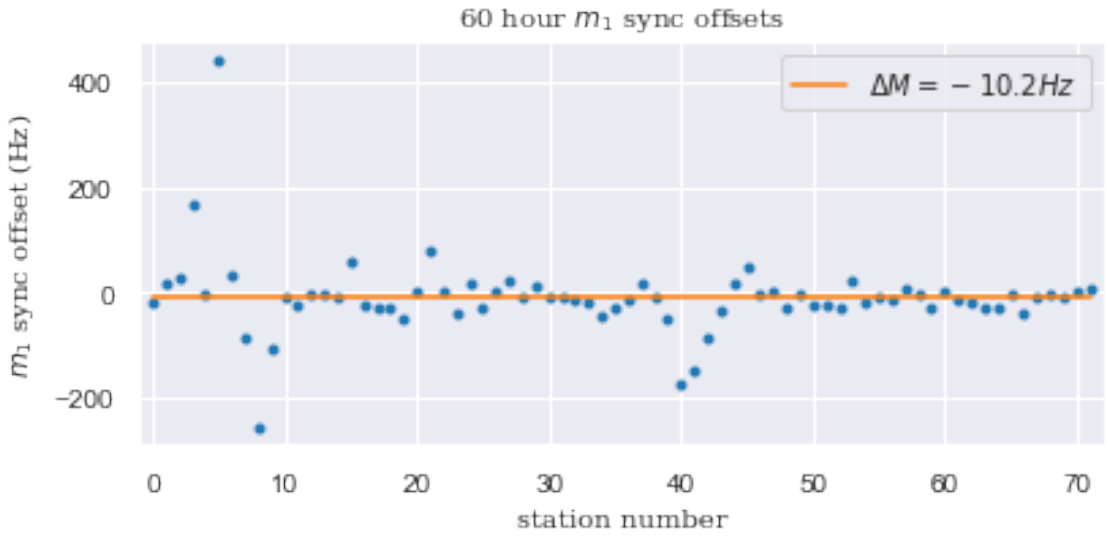

Figure 8.8: The sync offsets from the 60 hour data set for m_1, by station. The average of the sync offsets is used to estimate ΔM^2. In this case, $\Delta M^2 = (-10.2 \text{ Hz})^2$.

Moment	Uncertainty (Hz)	Uncertainty (ppb)
m_1	5.12	82.8
m_2	0.4222	6.83
m_3	1.55	25.1
m_4	0.354	5.72
m_5	1.37	22.2

Table 8.3: The uncertainty from higher-order gradient drifts for the azimuthally averaged moments in the 60 hour data set.

There are approximately 4000 measurements of field distributed in azimuth, which means that the trolley can track spatial Fourier components up to the Nyquist frequency $N = 2000$ term (see Figure 8.9). Compare this to the fixed probes. There are 72 stations roughly even distributed in azimuth, meaning they can only track up through the $N = 36$ spatial Fourier component. Any drift in higher Fourier components (specifically the harmonics of $N = 36$) during the fixed probe run can alias into the $N = 0$ term, meaning that any changes in the higher components will be incorrectly called a change in the azimuthal average [52]. In azimuthal space, this consists of field drifts that cause sharp features that are either between two fixed probe stations and therefore not observed, or at a fixed probe station and assumed to be larger in azimuth than they are.

Because the trolley measurements are sensitive to these higher order effects, they reveal any sharp features that have developed over the course of the fixed probe run, such as sharp gradients at magnetic pole cracks. The difference between two consecutive trolley runs is therefore a measurement of the influence of very high spatial frequency drift on the virtual trolley measurements, shown in Figure 8.10. Issues would arise if there were a sharp feature that developed between two fixed probe station, but vanished before another trolley run. However, no long stationary trolley runs or fixed probe have seen evidence of such events occurring. The sync offsets also include contributions from errors in fixed probe positions. Any error in a fixed probe position would correspond to higher-order gradients aliasing into the fixed probe moments in a way that is not accounted for by the change-of-basis matrix or Jacobian.

8.3.4 Super-long Stationary Run

Stationary runs are systematic studies where the trolley is parked under given fixed probe station for an extended period of time. These runs allow analyses of how the fixed probe measurements evolve directly compared to the trolley measurements. They allow for essentially continuous synchronization over long period of time, which reveals the evolution of the synchronized values relative to each other. In other terms, they allow for us to observe how the sync offsets evolve as a function of time. The super-long stationary run was a single such run that lasted for 72 hours. The trolley was parked under station 22, a well-behaved station with the standard 6-probe station geometry and a good signal-to-noise ratio for each of its probes, and allowed to collect data continuously. Station 22 was selected because it is in a region of the storage ring where every station has 6-probes, which would allow future studies of the correlations between neighboring stations. The m_1 measured by the trolley and the m_1 predicted by the fixed probe are shown in Figure 8.11.

We use this data to track how the sync offset evolves with respect to the averaging time.

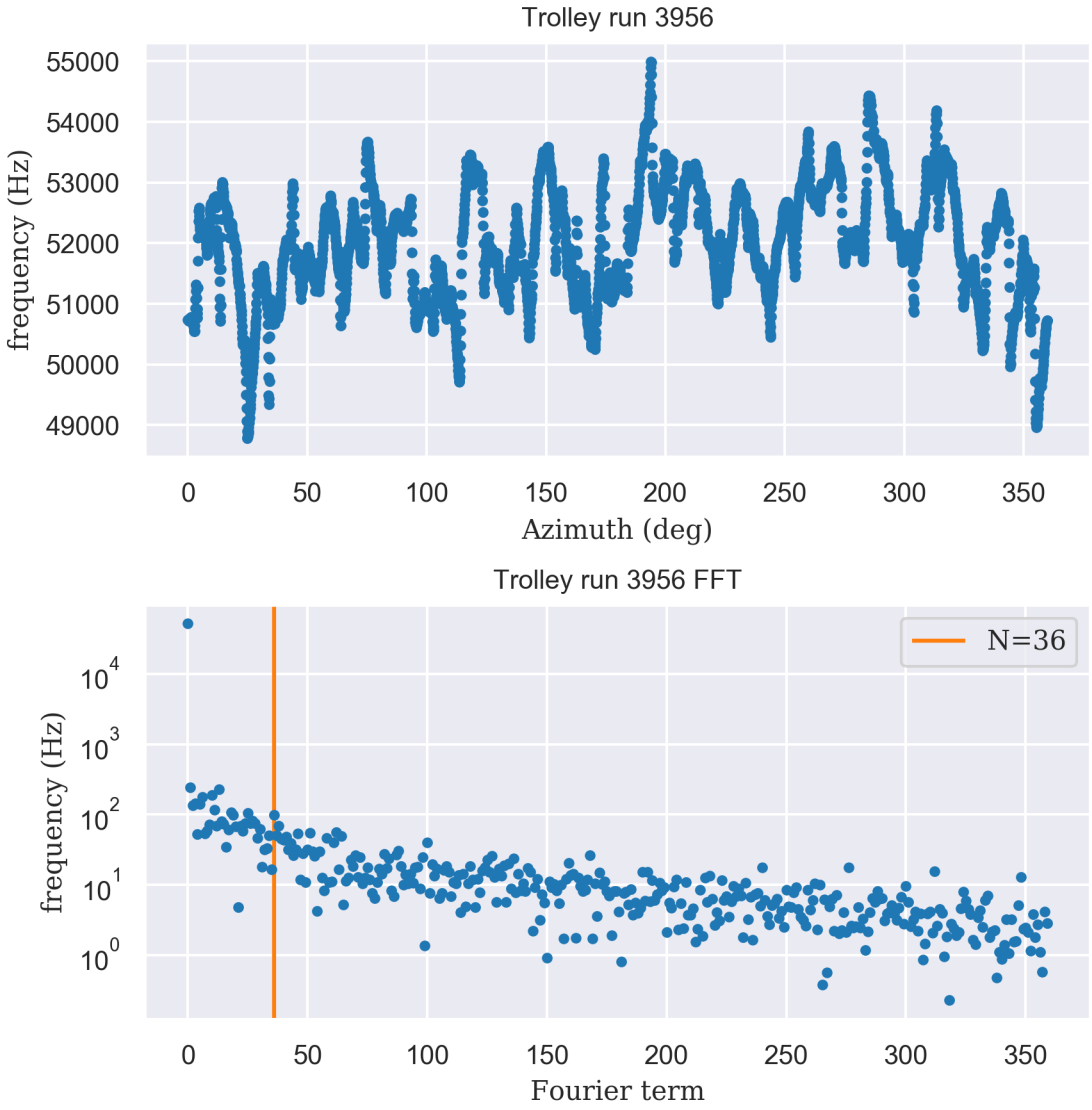

Figure 8.9: A single trolley run and its spatial FFT, showing the higher order spatial Fourier terms.

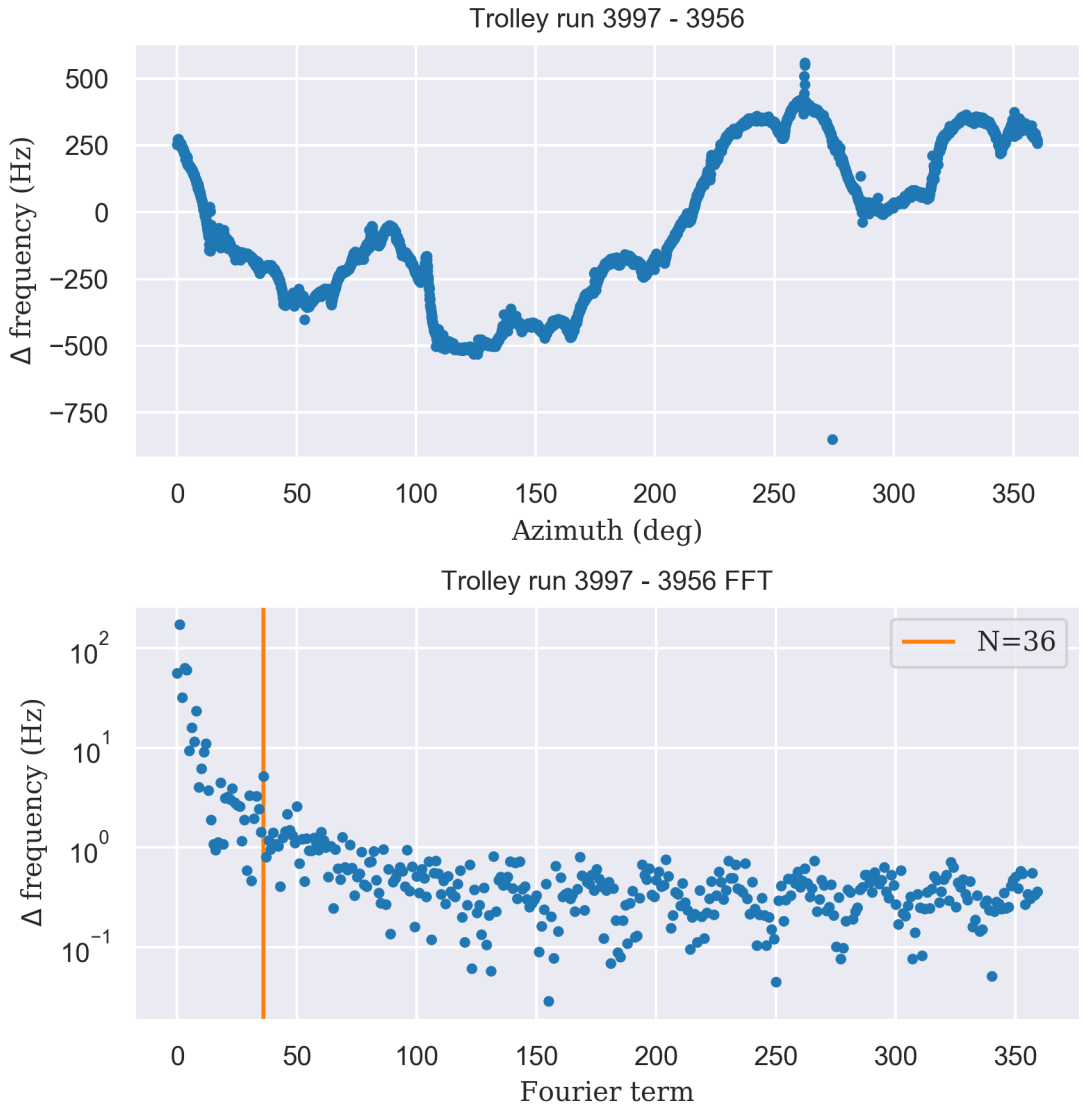

Figure 8.10: The difference of two consecutive trolley runs (separated by about 72 hours) and the difference's spatial FFT. Note that the higher Fourier terms drop off to under 1 Hz, indicating that the differential drift is mostly in the lower order terms that are tracked by the fixed probes.

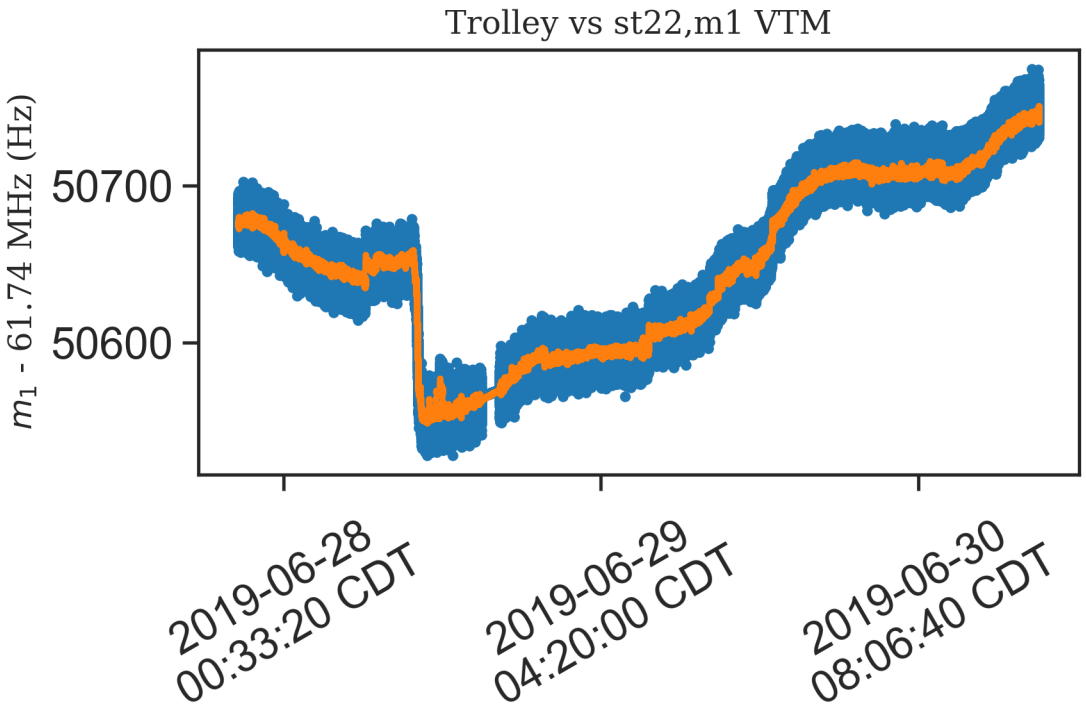

Figure 8.11: The dipole as measured by the trolley and predicted by the fixed probe during the super-long stationary run for station 22 (see Figure 4.5 for position).

This is best accomplished by examining the Allan deviation, which shows a measure of the uncertainty involved with averaging measurements as a function of the averaging time τ. The Allan deviation for the station 22 sync offset is shown in Figure 8.12. The slope of an Allan plot can be used to indicate the kind of noise that is dominant for a given averaging time. Random walks have a $\sqrt{\tau}$ dependence on averaging time and a slope of $+1/2$ (on the log-log scale) in a plot of Allan deviation. The solid line shown in Figure 8.12 is consistent with a random walk model of the sync drift. Its coefficient is $0.26Hz/\sqrt{\text{hr}}$, which corresponds to a total uncertainty of 15 Hz over a 60 hr period. This is consistent with the model above for ΔM^2 estimated by the sync offsets. It should be noted that these two estimates come from different data sets, and that the estimate for ΔM^2 in Equation 8.7 is for the average of the stations, while the estimate from the super-long stationary run is for only one station.

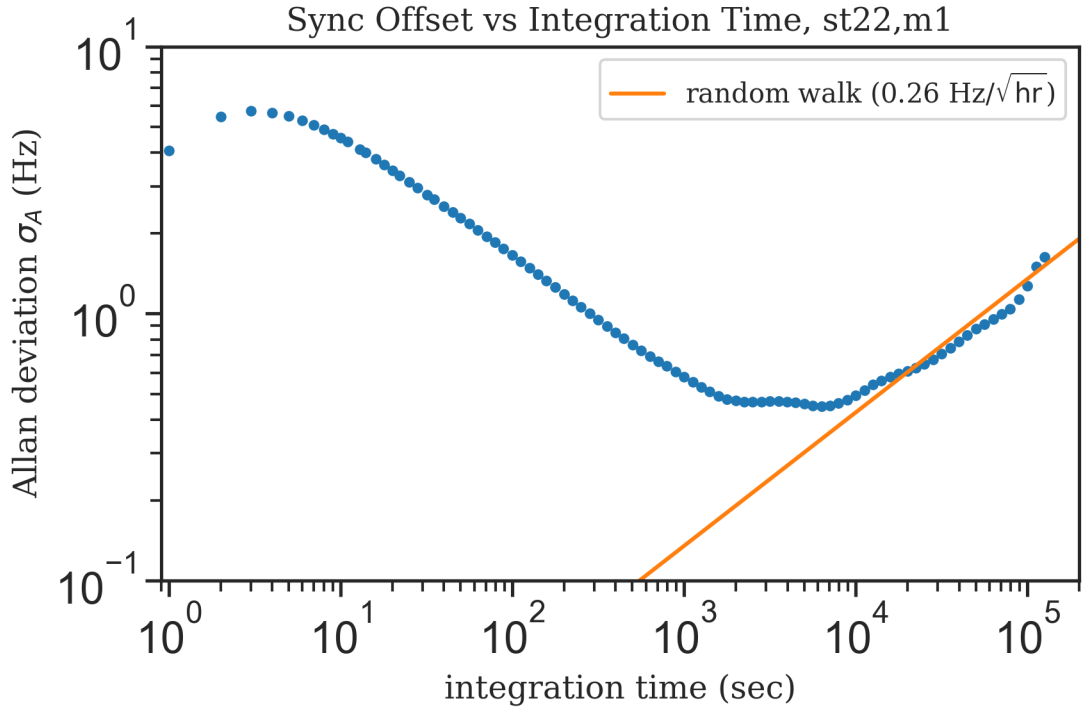

Figure 8.12: The Allan deviation of the station 22 m_1 sync offset. For long averaging times, the Allan deviation is dominated by random walk noise (the solid line).

8.3.5 Global Random Walk Rate Method

An additional proposed method for estimating the uncertainty caused by higher-order moments drifts is to use the sync offsets from every trolley pair in Run 1 to estimate a single random walk rate for the azimuthal average of the ring. Instead of using each trolley pair's

mean sync offset to estimate the random walk rate for that pair, we can use an average of the rates from all the trolley pairs.

This method could improve on the current method used above by making the method robust against over or underestimating the random walk rate based on only the final sync offset. For instance, the synchronization error can drift away from the synchronization values, and then back towards it, which would cause the estimate using only the final value of the sync offset to underestimate the rate of the intermediate drift. Similarly, if the synchronization error drifted away nearly linearly, the final sync offset would overestimate the rate of the intermediate drift (recall that any linear component of the drift is removed by the backward interpolation covered in Section 6.5).

There are 12 trolley run pairs in Run 1. The azimuthally averaged sync offset and corresponding random walk rate for each are shown in Table 8.4. Taking the average of the rates from each pair (except Endgame, pair 2) yields an estimated global rate for Run 1 of 0.0210 Hz/$\sqrt{sec}$. Over 72 hours between trolley runs, this leads to an estimated uncertainty of 12.7 Hz, in line with the estimates discussed above. One benefit of this global method is that the estimated uncertainty for each trolley pair becomes a function of just the time between the trolley runs, which can inform future trolley run planning. However, this could also be a drawback, as it means that the uncertainty estimate is agnostic to the specific conditions of each run, such as the issue in Endgame pair 2 (see Section 9.4). Further studies and analytic work are needed to assess the best way forward using this estimation method.

8.4 Systematics Conclusion

Tables 8.5, 8.6, and 8.7 show the combined systematic uncertainties, added in quadrature, from all the field sources discussed above for the 60 hour data set.

Trolley pair	Average sync offset (Hz)	Random walk rate ($\mathrm{Hz}/\sqrt{sec}$)	Notes
60 hour	-10.2	0.0198	
9 day, pair 1	4.95	0.00953	
9 day, pair 2	-12.7	0.0277	
9 day, pair 3	-6.77	0.0137	
9 day, pair 4	3.97	0.00895	
Endgame, pair 2	29.4	0.0516	Magnetic disturbance during run, see Section 9.4.
Endgame, pair 3	3.19	0.00624	
Endgame, pair 4	-21.2	0.0374	
Endgame, pair 5	13.9	0.0264	
High kick, pair 1	-13.6	0.0283	
High kick, pair 2	-4.86	0.0101	
Low kick	9.07	0.0167	
Average drift rate		0.0210	Not including Endgame, pair 2.

Table 8.4: The azimuthally averaged sync offset and associate random walk rate for each trolley pair in Run 1. Also, the average random walk rate, which can be used to estimate the uncertainty caused by higher-order moment drifts between trolley runs.

m_1 **Interpolation**		
Source	Description	Error (ppb)
Type A — Independent for each VTM		
Fixed probe shot noise	Frequency extraction and shot noise	1 ppb
Type A/B — Independent for each trolley run (baseline measurement)		
Trolley footprint removal		8 ppb
Trolley azimuthal position		5 ppb
Trolley spikes	Can benefit from future correction	5 ppb
Trolley swimming	X-Y motion in trolley	10 ppb
Trolley frequency extraction	Averaged over stations azimuthally	1 ppb
Other trolley motion effects	More in-depth studies underway	20 ppb
Type B — Cannot be improved by increased averaging time		
Temperature drift	4 ppb/ °C × 2 °C	8 ppb
Plunging probe calibration		12 ppb
Interpolation uncertainty	Using sync offsets and random walk model	83 ppb
Total		88 ppb

Table 8.5: Systematics for time- and azimuthally- averaged m_1 interpolation (for the 60 hour data set). See Chapter IX for total uncertainties for the other Run 1 data sets. Note that these are conservative estimates.

m_2 **Interpolation**		
Source	Description	Error (ppb)
Type A — Independent for each VTM		
Fixed probe shot noise	Frequency extraction and shot noise	1 ppb
Type A/B — Independent for each trolley run (baseline measurement)		
Trolley footprint removal		8 ppb
Trolley azimuthal position		5 ppb
Trolley spikes	Can benefit from future correction	5 ppb
Trolley swimming	X-Y motion in trolley	26 ppb
Trolley frequency extraction	Averaged over stations azimuthally	1 ppb
Other trolley motion effects	More in-depth studies underway	20 ppb
Type B — Cannot be improved by increased averaging time		
Temperature drift	4 ppb/ °C × 2 °C	8 ppb
Plunging probe calibration		6 ppb
Interpolation uncertainty	Using sync offsets and random walk model	7 ppb
Total		38 ppb

Table 8.6: Systematics for time- and azimuthally- averaged m_2 interpolation (for the 60 hour data set). See Chapter IX for total uncertainties for the other Run 1 data sets. Note that these are conservative estimates.

m_3 **Interpolation**		
Source	Description	Error (ppb)
Type A — Independent for each VTM		
Fixed probe shot noise	Frequency extraction and shot noise	1 ppb
Type A/B — Independent for each trolley run (baseline measurement)		
Trolley footprint removal		8 ppb
Trolley azimuthal position		5 ppb
Trolley spikes	Can benefit from future correction	5 ppb
Trolley swimming	X-Y motion in trolley	2 ppb
Trolley frequency extraction	Averaged over stations azimuthally	1 ppb
Other trolley motion effects	More in-depth studies underway	20 ppb
Type B — Cannot be improved by increased averaging time		
Temperature drift	4 ppb/ °C × 2 °C	8 ppb
Plunging probe calibration		6 ppb
Interpolation uncertainty	Using sync offsets and random walk model	25 ppb
Total		37 ppb

Table 8.7: Systematics for time- and azimuthally- averaged m_3 interpolation (for the 60 hour data set). See Chapter IX for total uncertainties for the other Run 1 data sets. Note that these are conservative estimates.

CHAPTER IX

Summary of Run 1 Data Sets

9.1 Blinding Status

The field data are blinded at two levels. The absolute calibration of the plunging probe is blinded by adding an unknown offset of ±100 ppb to each trolley calibration offset. This addition blinds only the m_1 moment. Because all of the other moments are differences of probe measurements, so the blind cancels. Additionally, each of the two independent interpolation analyses (this dissertation records one such analysis) separately blinds m_1 through m_5. These blinded moments have been used for any comparisons of the two analyses. During an interpolation review in mid-2019, the 60 hour data set was unblinded by both analysis teams. However, all the other data sets remain blinded. These blinds on the m_1 moment are ±62 Hz (1 ppm), and ±6.2 Hz (100 ppb) on the higher moments. This means that in the following plots of the azimuthally-averaged moments for the 60 hour data set, the m_1 moment is blinded at the 6.2 Hz level and the higher-order moments m_2 through m_5 are unblinded. For the other data sets, the m_1 moment is blinded at the 62 Hz level and the higher-order moments m_2 through m_5 are blinded at the 6.2 Hz level. These blinds do not influence the systematic uncertainty analyses.

9.2 60 Hour Data Set

The 60 hour data set represents a typical run bookended by trolley runs. No extreme events such as the magnet dumping or the surface coil configurations changing occurred during the course of the measurement, and the analysis includes the forward-backward sync interpolation. The data are azimuthally averaged over the 72 stations and time averaged in bins of 100 seconds for clarity in the plots in Figure 9.1. The uncertainties on the *fully time averaged* moments are shown in Table 9.1. See Appendix A for further information about the definition of the data sets and production data for all Run 1 data sets.

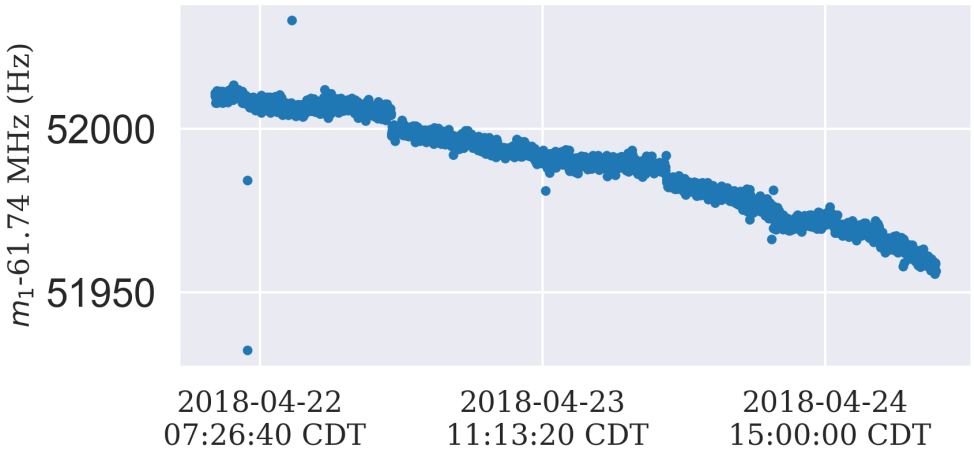
m_1-61.74 MHz (Hz)
52000
51950
2018-04-22
07:26:40 CDT
2018-04-23
11:13:20 CDT
2018-04-24
15:00:00 CDT

(a)

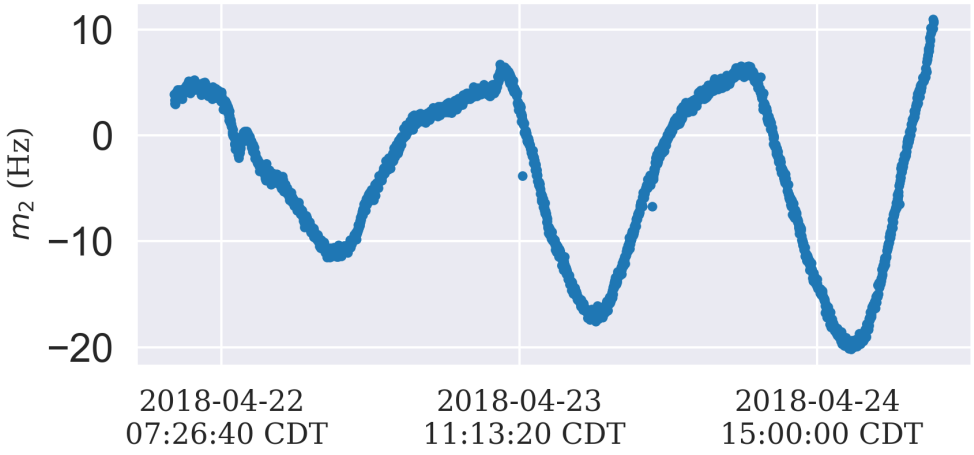
m_2 (Hz)
10
0
−10
−20
2018-04-22
07:26:40 CDT
2018-04-23
11:13:20 CDT
2018-04-24
15:00:00 CDT

(b)

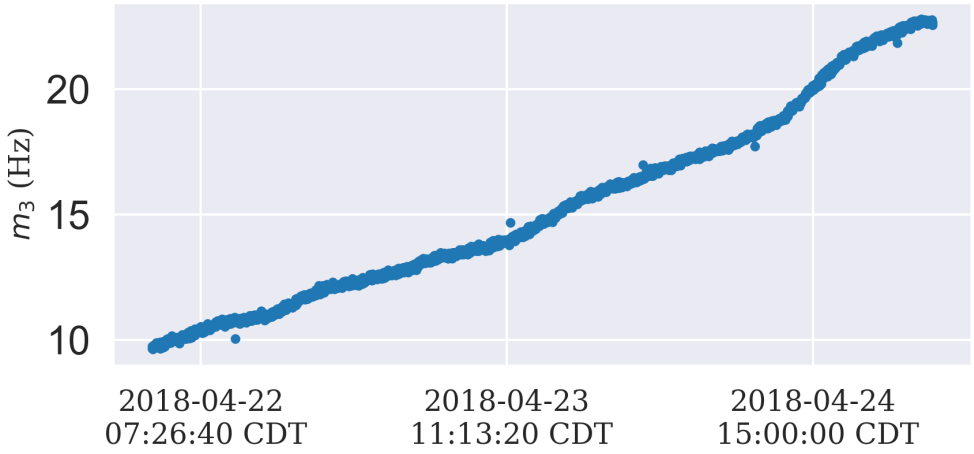
m_3 (Hz)
20
15
10
2018-04-22
07:26:40 CDT
2018-04-23
11:13:20 CDT
2018-04-24
15:00:00 CDT

(c)

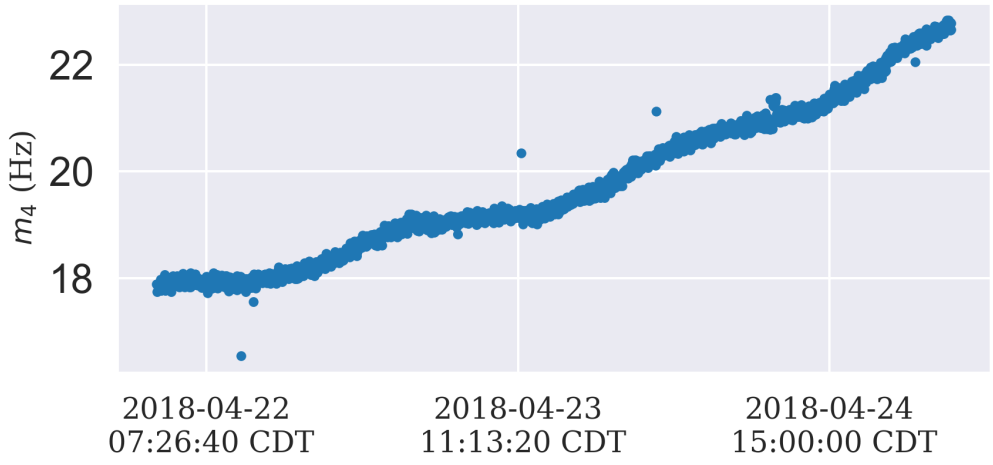

(d)

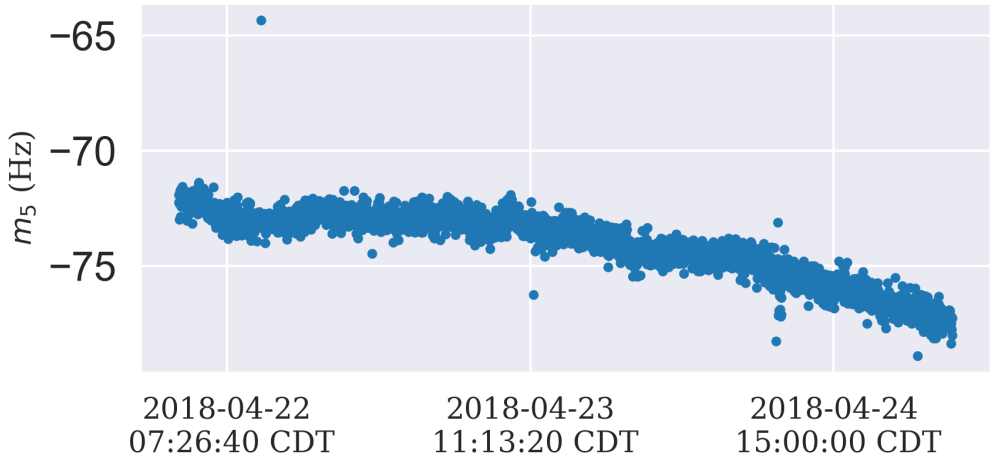

(e)

Figure 9.1: The azimuthally-averaged field moments from the 60 hour data set. Each point is an average over 100 seconds. (a) through (e): m_1 through m_5, respectively.

Source	Uncertainty (Hz)	(ppb)
Type A	0.06	1
Type A/B	1.4	23
Type B	0.62	10
m_1 Trolley Swimming	.62	10
Interpolation Uncertainty	5.12	82.8
Total	5.41	88
m_2 Trolley Swimming	1.6	26
Interpolation Uncertainty	0.422	6.83
Total	2.35	38
m_3 Trolley Swimming	0.12	2
Interpolation Uncertainty	1.55	25.1
Total	2.28	37
m_4 Trolley Swimming	0.12	2
Interpolation Uncertainty	0.354	5.72
Total	1.7	28
m_5 Trolley Swimming	1.6	26
Interpolation Uncertainty	1.37	22.2
Total	2.68	43

Table 9.1: A list of the uncertainties in the time averaged 60 hour data set. Note that the moment-dependent systematics are tabulated separately.

9.3 9 Day Data Set

The 9 day data set consists of four trolley-bookended fixed probe runs. Each fixed probe run is analyzed in the same way as the "typical run" of the 60 hour data set. The primary difference is that some of the trolley runs can be used for backward synchronization on one run, and then forward synchronization on the next run.

There were several data quality issues that occurred during this data set. The prevailing issue was that electrical interference from the pulsing electric quadrupoles intermittently caused a false trigger in the NMR probe multiplexers, causing a reading from an NMR probe to be unusable. Implementing data-quality cuts to identify and label each of the these false triggers so they can be dropped from the analysis is an ongoing effort at this time. This created isolated instances when the time grid interpolates several times between fixed probe readings. However, averaged over long periods, this makes no difference in the final result, because the uncertainty associated with averaging the fixed probe measurements is so small. For some of the noisier probes, automatic false trigger detection is difficult and improvement is ongoing.

Occasionally, the false trigger occurred in a probe that was used in the power supply feedback. The flawed measurement got averaged in to the feedback signal, causing the

PSFB to incorrectly believe the average magnetic field had suddenly moved, so it would begin to apply a correction to return to its set point. The next feedback measurement, however, would be correct, so the PSFB would stop applying the correction, and instead return to the proper set point. These times have been flagged for the ω_a team to avoid analyzing. However, they are still shown in Figure 9.2, but will be omitted automatically during the time averaging step explained in Chapter VII.

There were two issues with the trolley runs during this data set. First, right after the second trolley run (the end of the first fixed probe run) was completed, the magnet began to slow dump (a process where it dumps the current in the superconducting coils to prevent any possible damage from a detected environmental change). After the field was brought down and back up, a third trolley run was performed. The consequence is that the second trolley run can only be used for backward synchronization and that the third trolley run is only used for forward synchronization. Second, after the fifth trolley run (the beginning of the final fixed probe run), a study was performed that involved drastic changes to the surface correction coil currents. Upon analyzing the final fixed probe run, it was discovered that these changes led to large sync offsets, indicating that the synchronization doesn't track well over such studies. Therefore, the final fixed probe run is only synced to the sixth trolley run and only synchronizes backwards.

The data shown here are azimuthally averaged over the 72 stations and time averaged in bins of 100 seconds for clarity in the plots in Figure 9.1. The uncertainties of the *fully time averaged* moments are shown in Table 9.1.

9.4 End Game Data Set

The end game data set is the longest continuous data set in Run 1, at approximately 23 days. It nominally consists of six fixed probe runs and nine trolley runs. However, due to a hardware failure in the SCC crates during the first fixed probe run, that run has been dropped entirely and is not included here. The second and third fixed probe runs were bookended by independent trolley runs due to a magnet cycle that occurred between them (trolley runs 2 and 3, and 4 and 5, respectively). The next three fixed probe runs occurred consecutively; they are bookended by trolley pairs 6 and 7, 7 and 8, and 8 and 9. During the second fixed probe run, a magnetic cable connector that was accidentally left near the field was pulled against the vacuum chamber by the magnet, significantly perturbing the local field abruptly. During trolley run 9, the magnet began to slow dump, preventing the trolley run from completing. For this reason, fixed probe run 6 is only forward synced — trolley run 9 is not used.

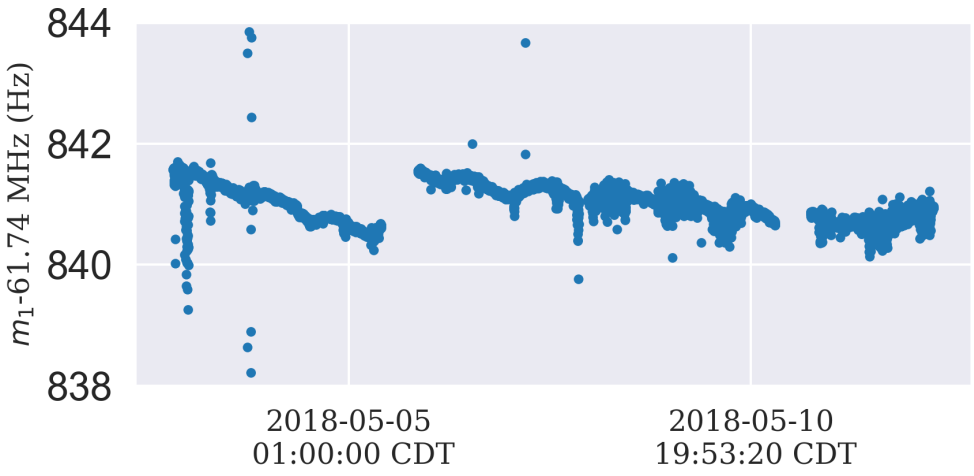
844
842
840
838
m_1-61.74 MHz (Hz)
2018-05-05
01:00:00 CDT
2018-05-10
19:53:20 CDT

(a)

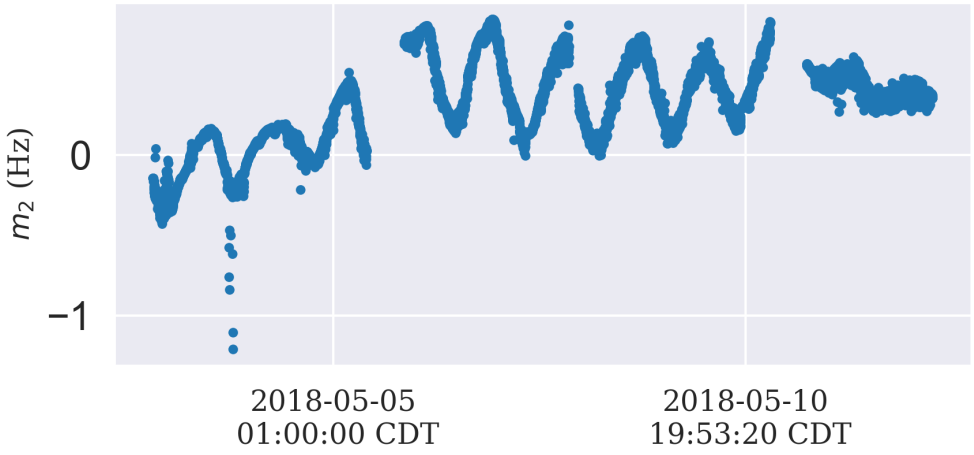
0
−1
m_2 (Hz)
2018-05-05
01:00:00 CDT
2018-05-10
19:53:20 CDT

(b)

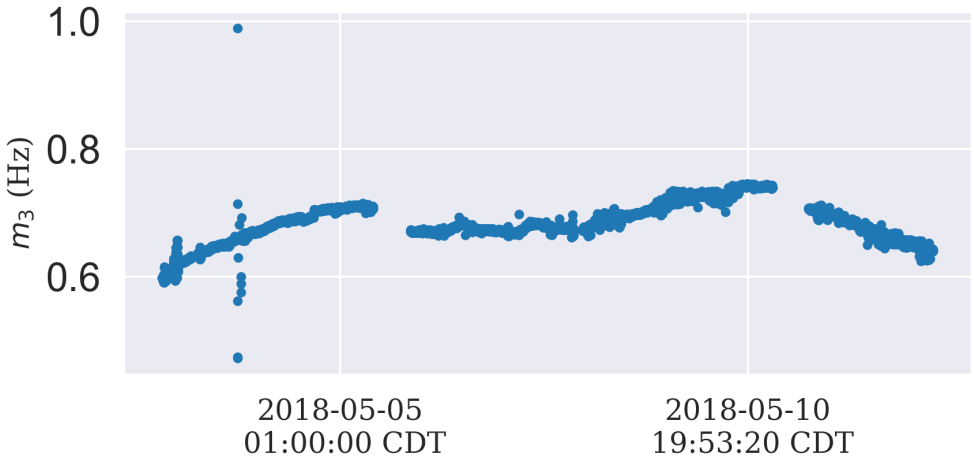
1.0
0.8
0.6
m_3 (Hz)
2018-05-05
01:00:00 CDT
2018-05-10
19:53:20 CDT

(c)

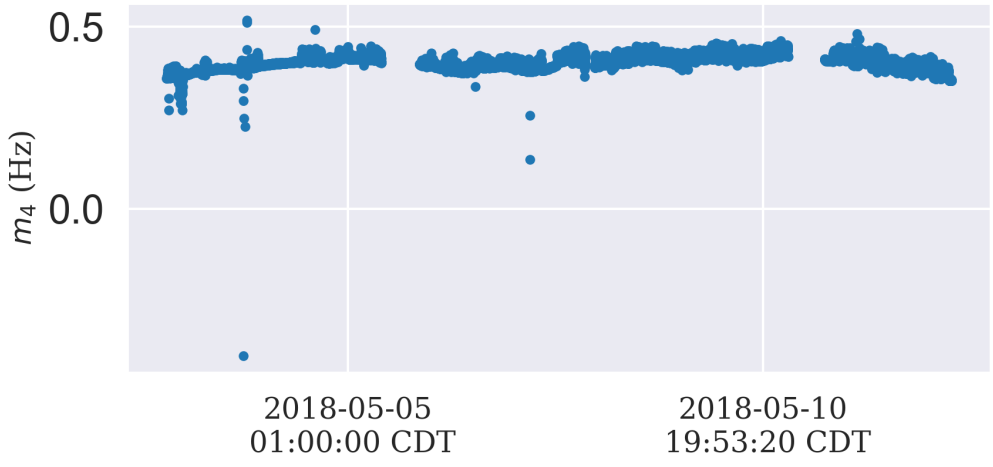

(d)

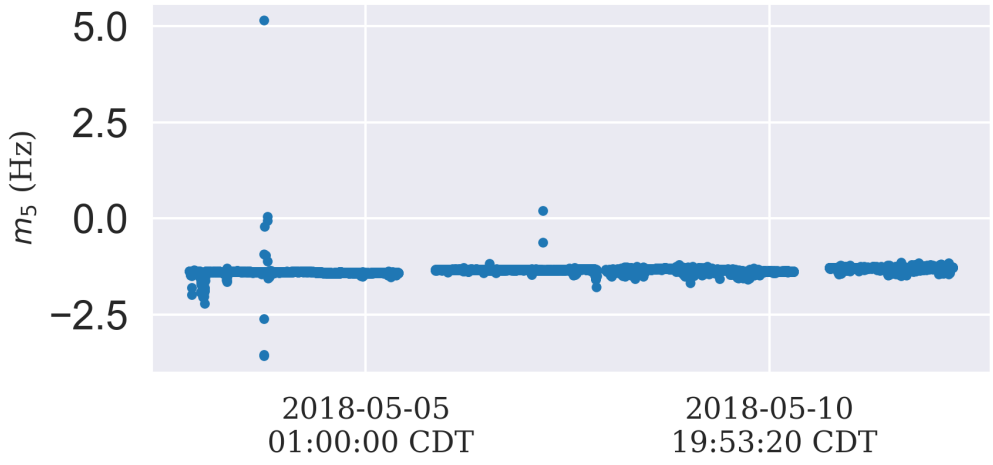

(e)

Figure 9.2: The azimuthally-averaged field moments over the 9 day data set. Each point is an average over 100 seconds. The 9 day data set is currently still blinded. (a) through (e): m_1 through m_5, respectively.

Source	Uncertainty (Hz)	(ppb)
Type A	0.06	<1
Type A/B	1.4	23
Type B	0.62	10
m_1 Trolley Swimming	.62	10
Interpolation Uncertainty	3.97	64
Total	4.35	70
m_2 Trolley Swimming	1.6	26
Interpolation Uncertainty	5.00	81
Total	5.51	89
m_3 Trolley Swimming	0.12	2
Interpolation Uncertainty	2.28	37
Total	2.83	46
m_4 Trolley Swimming	0.12	2
Interpolation Uncertainty	0.346	6
Total	1.7	28
m_5 Trolley Swimming	1.6	26
Interpolation Uncertainty	1.19	19
Total	2.59	42

Table 9.2: A list of the uncertainties in the time averaged 9 day data set. Note that the moment-dependent systematics are tabulated separately.

Apart from the issues with fixed probe runs 1 and 2, and trolley run 9, the endgame data set was very well behaved. The data shown here are azimuthally averaged over the 72 stations and time averaged in bins of 100 seconds for clarity in the plots in Figure 9.3. The uncertainties in the *fully time averaged* moments are shown in Table 9.3.

9.5 High Kick Data Set

The high kick data set was approximately six days long and consists of two fixed probe runs and three trolley runs. Both fixed probe runs are forward-backward synced, so the second trolley run is used to synchronize both fixed probe runs. There was one PSFB event during the second fixed probe run, which is shown in this data. However, the field data quality team has flagged it for removal from the ω_a analysis, so it will not influence the field average in the end. The data shown here are azimuthally averaged over the 72 stations and time averaged in bins of 100 seconds for clarity in the plots in Figure 9.4. The uncertainties in the *fully time averaged* moments are shown in Table 9.4.

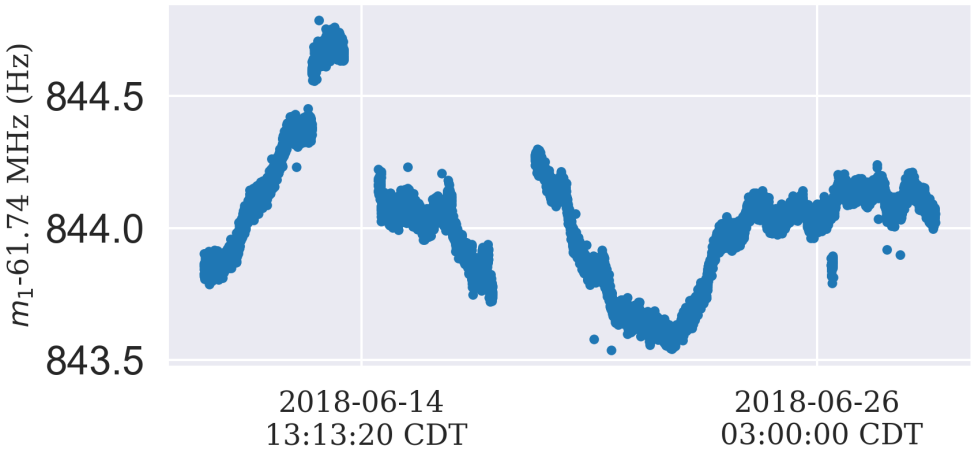
m_1-61.74 MHz (Hz)
844.5
844.0
843.5
2018-06-14
13:13:20 CDT
2018-06-26
03:00:00 CDT

(a)

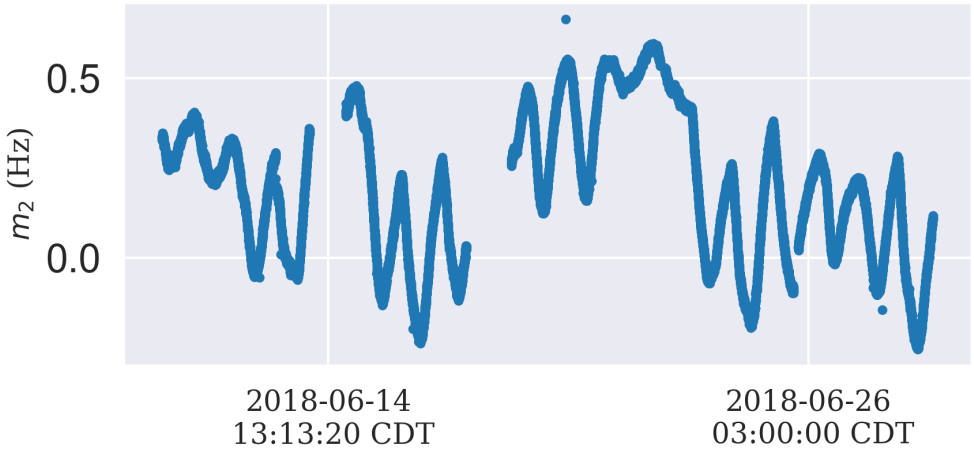
m_2 (Hz)
0.5
0.0
2018-06-14
13:13:20 CDT
2018-06-26
03:00:00 CDT

(b)

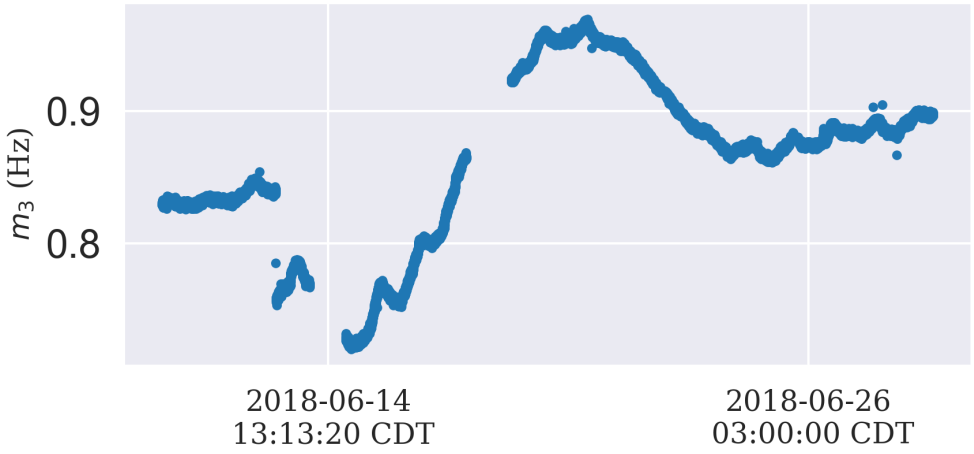
m_3 (Hz)
0.9
0.8
2018-06-14
13:13:20 CDT
2018-06-26
03:00:00 CDT

(c)

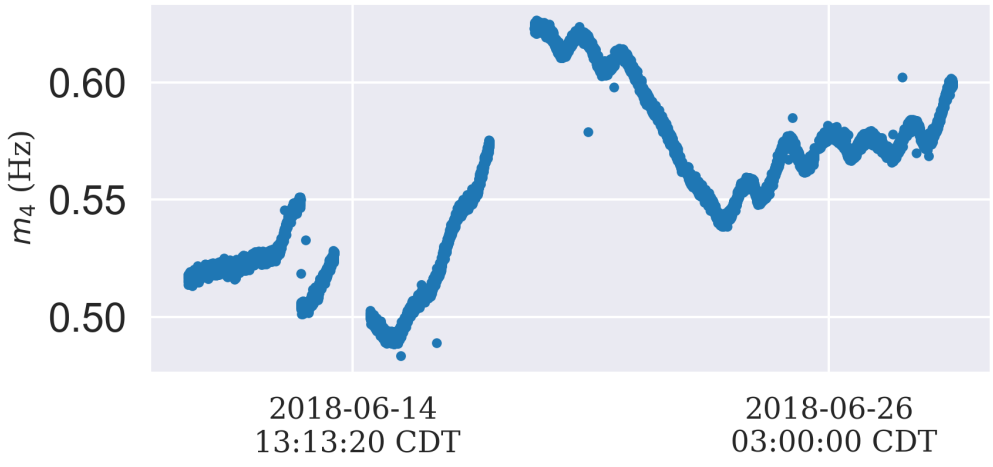

(d)

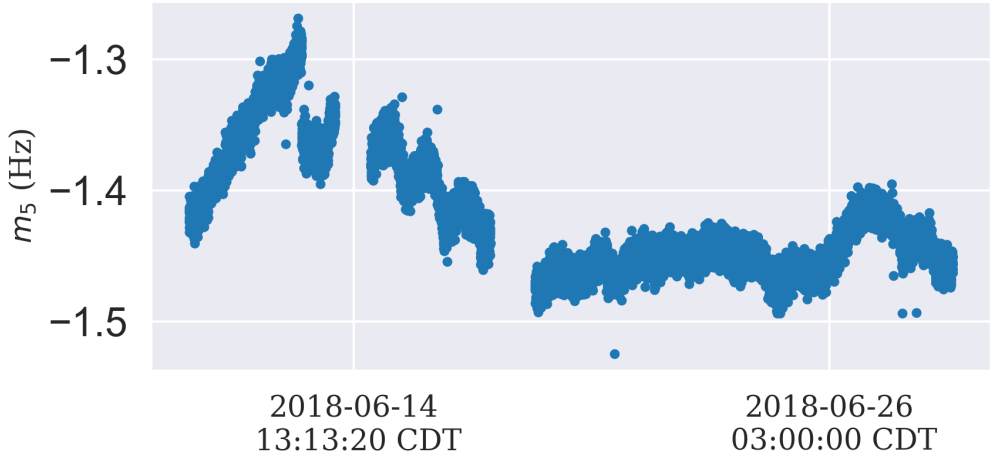

(e)

Figure 9.3: The azimuthally-averaged field moments over the end game data set. Each point is an average over 100 seconds. The end game data set is currently still blinded. (a) through (e): m_1 through m_5, respectively.

Source	Uncertainty (Hz)	(ppb)
Type A	0.06	<1
Type A/B	1.4	23
Type B	0.62	10
m_1 Trolley Swimming	.62	10
Interpolation Uncertainty	12.8	207
Total	13.0	210
m_2 Trolley Swimming	1.6	26
Interpolation Uncertainty	3.84	62
Total	4.48	73
m_3 Trolley Swimming	0.12	2
Interpolation Uncertainty	1.07	17
Total	1.98	32
m_4 Trolley Swimming	0.12	2
Interpolation Uncertainty	1.42	23
Total	2.19	35
m_5 Trolley Swimming	1.6	26
Interpolation Uncertainty	4.56	74
Total	5.11	83

Table 9.3: A list of the uncertainties in the time averaged end game data set. Note that the moment-dependent systematics are tabulated separately.

Source	Uncertainty (Hz)	(ppb)
Type A	0.06	<1
Type A/B	1.4	23
Type B	0.62	10
m_1 Trolley Swimming	.62	10
Interpolation Uncertainty	5.22	84
Total	5.51	89
m_2 Trolley Swimming	1.6	26
Interpolation Uncertainty	3.01	49
Total	3.79	61
m_3 Trolley Swimming	0.12	2
Interpolation Uncertainty	1.25	20
Total	2.08	34
m_4 Trolley Swimming	0.12	2
Interpolation Uncertainty	0.588	10
Total	1.77	29
m_5 Trolley Swimming	1.6	26
Interpolation Uncertainty	1.10	18
Total	2.56	41

Table 9.4: A list of the uncertainties in the time averaged high kick data set. Note that the moment-dependent systematics are tabulated separately.

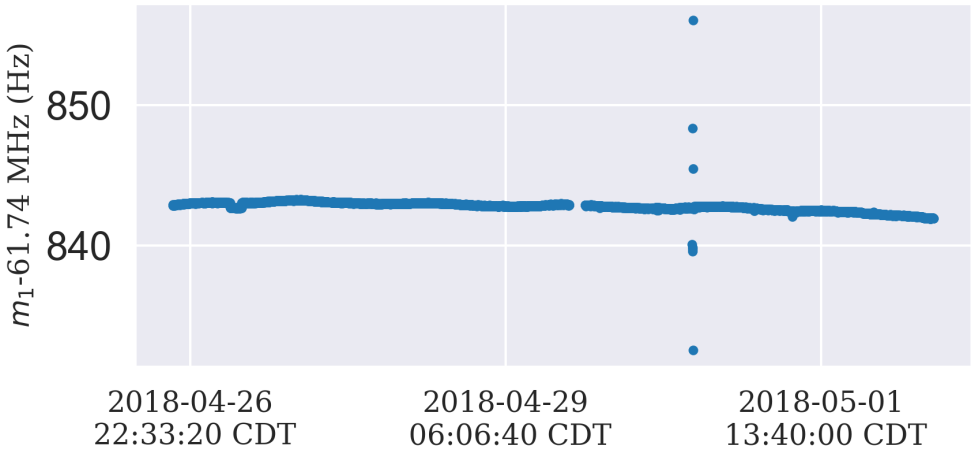
m_1-61.74 MHz (Hz)
850
840
2018-04-26
22:33:20 CDT
2018-04-29
06:06:40 CDT
2018-05-01
13:40:00 CDT

(a)

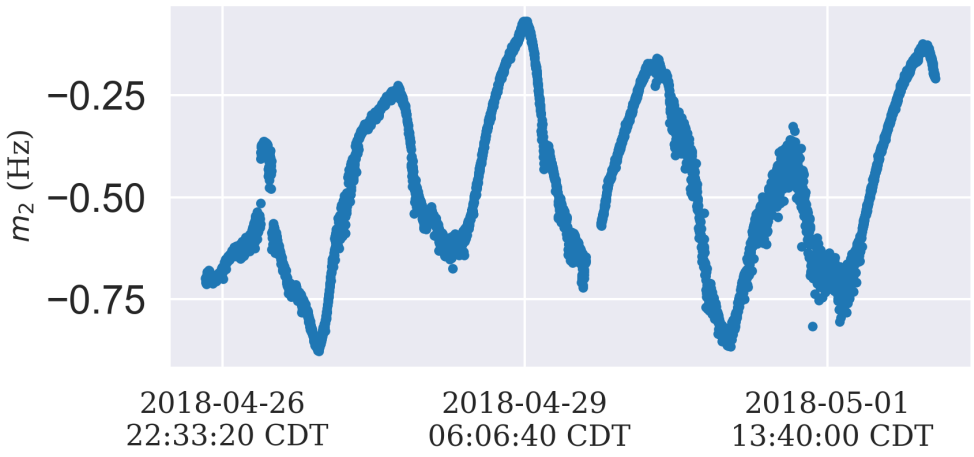
m_2 (Hz)
−0.25
−0.50
−0.75
2018-04-26
22:33:20 CDT
2018-04-29
06:06:40 CDT
2018-05-01
13:40:00 CDT

(b)

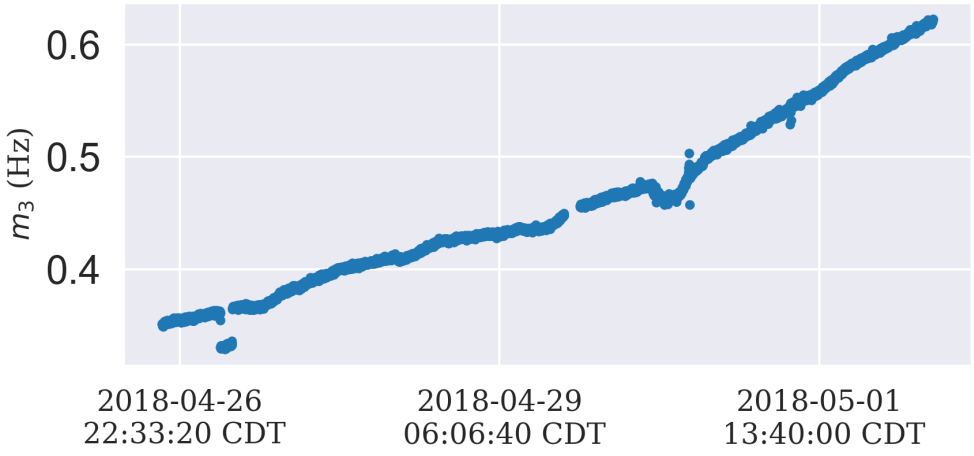
m_3 (Hz)
0.6
0.5
0.4
2018-04-26
22:33:20 CDT
2018-04-29
06:06:40 CDT
2018-05-01
13:40:00 CDT

(c)

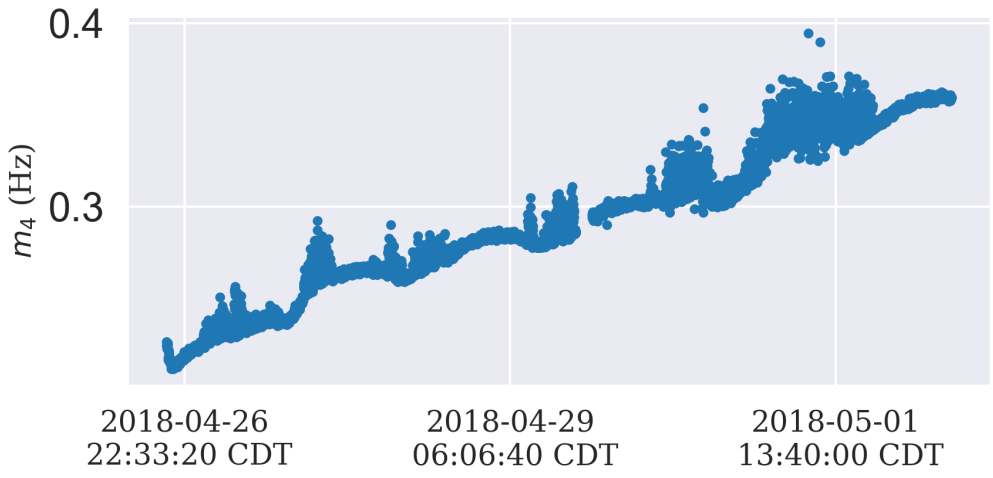

(d)

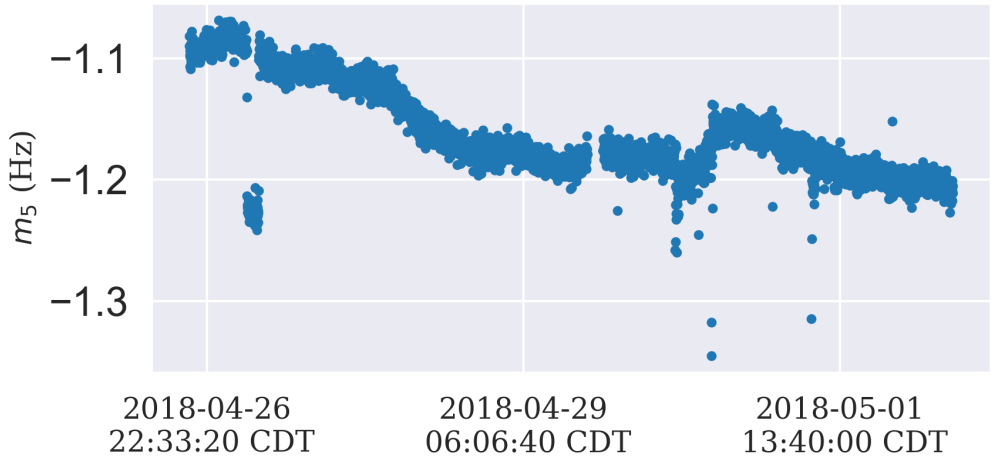

(e)

Figure 9.4: The azimuthally-averaged field moments over the high kick data set. Each point is an average over 100 seconds. The high kick data set is currently still blinded. (a) through (e): m_1 through m_5, respectively.

Source	Uncertainty (Hz)	(ppb)
Type A	0.06	<1
Type A/B	1.4	23
Type B	0.62	10
m_1 Trolley Swimming	.62	10
Interpolation Uncertainty	4.53	73
Total	4.87	79
m_2 Trolley Swimming	1.6	26
Interpolation Uncertainty	0.194	3
Total	2.32	37
m_3 Trolley Swimming	0.12	2
Interpolation Uncertainty	0.741	12
Total	1.82	30
m_4 Trolley Swimming	0.12	2
Interpolation Uncertainty	0.423	7
Total	1.72	28
m_5 Trolley Swimming	1.6	26
Interpolation Uncertainty	1.38	22
Total	2.69	44

Table 9.5: A list of the uncertainties in the time averaged low kick data set. Note that the moment-dependent systematics are tabulated separately.

9.6 Low Kick Data Set

The low kick data set is another typical run bookended by trolley runs, with no extreme events or configuration changes. It lasted approximately 3 days, and includes the forward-backward sync interpolation. The data shown here are azimuthally averaged over the 72 stations and time averaged in bins of 100 seconds for clarity in the plots in Figure 9.5. The uncertainties in the *fully time averaged* moments are shown in Table 9.5. Although this is a good run from the perspective of the magnetic field, due to issues with the beam storage systems, the ω_a statistical and systematic uncertainties for this run would be quite large. Therefore, these data are not currently used in the Run 1 analysis.

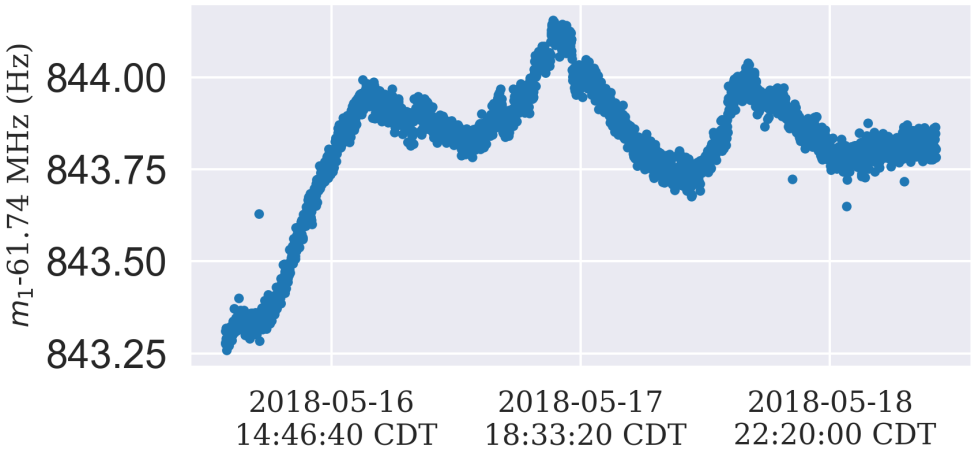
m_1-61.74 MHz (Hz)
844.00
843.75
843.50
843.25
2018-05-16
14:46:40 CDT
2018-05-17
18:33:20 CDT
2018-05-18
22:20:00 CDT

(a)

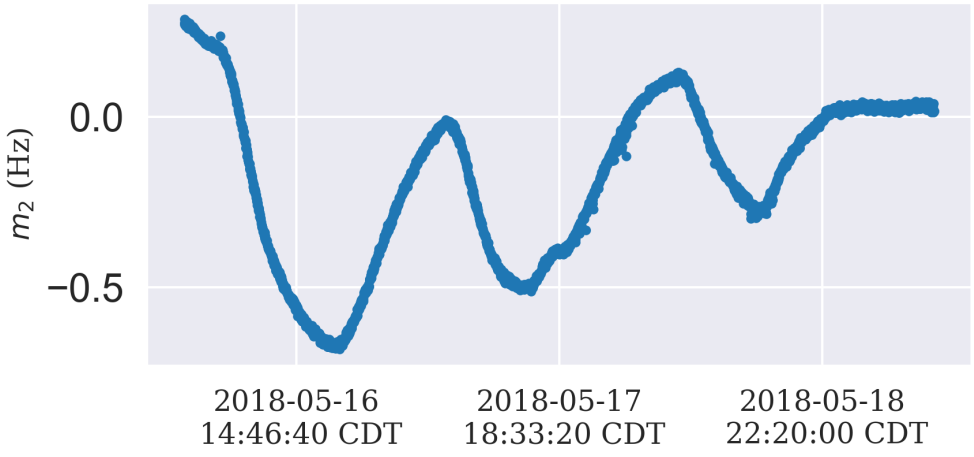
m_2 (Hz)
0.0
−0.5
2018-05-16
14:46:40 CDT
2018-05-17
18:33:20 CDT
2018-05-18
22:20:00 CDT

(b)

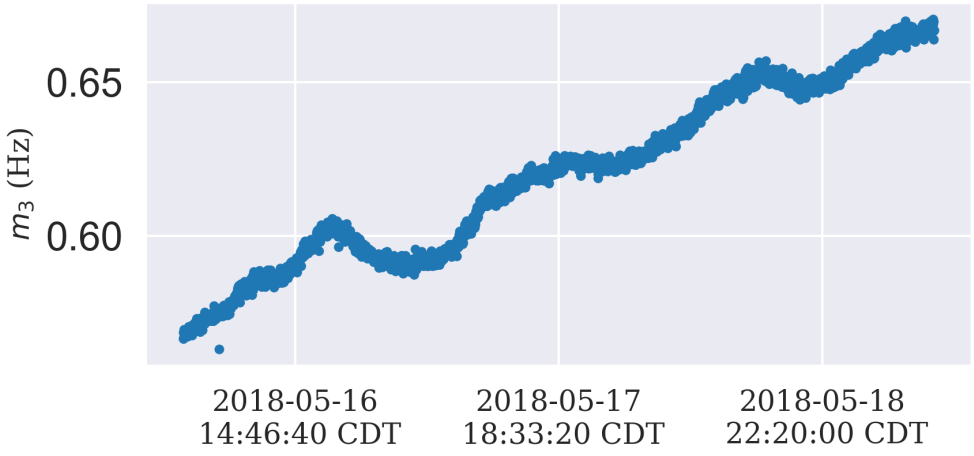
m_3 (Hz)
0.65
0.60
2018-05-16
14:46:40 CDT
2018-05-17
18:33:20 CDT
2018-05-18
22:20:00 CDT

(c)

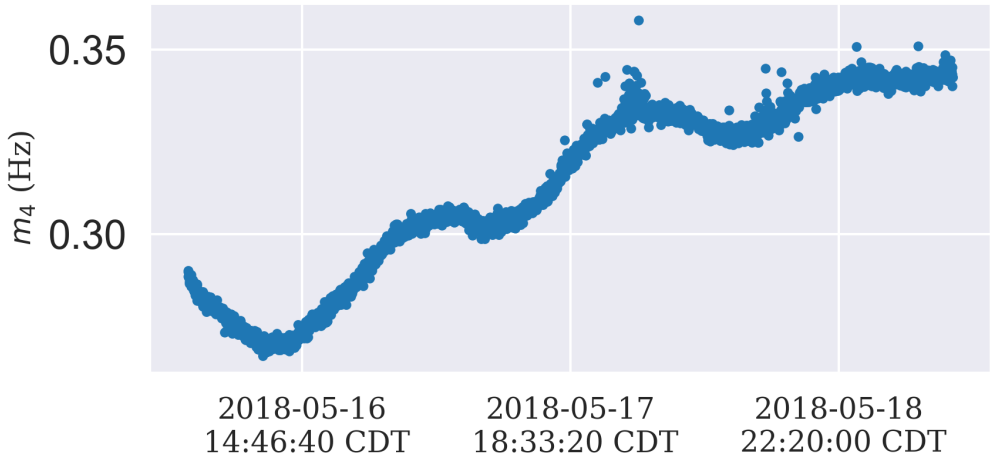

(d)

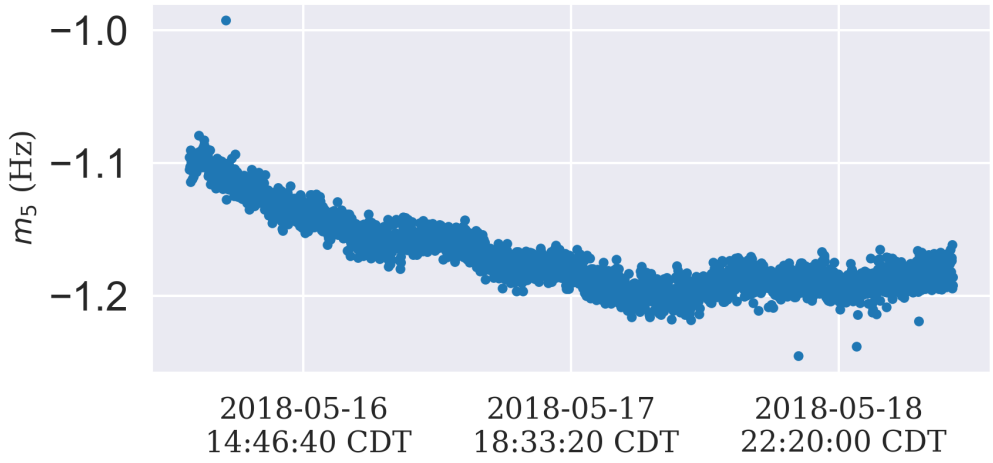

(e)

Figure 9.5: The azimuthally-averaged field moments over the low kick data set. Each point is an average over 100 seconds. The low kick data set is currently still blinded. (a) through (e): m_1 through m_5, respectively.

CHAPTER X

Conclusions and Outlook

This work presented an analysis of the full field maps for the five primary data sets from Run 1, as well as conservative estimates of the systematic uncertainties for each data set. The systematic uncertainties are dominated by the sync offset estimate of the higher-order gradient drift. As mentioned in Section 8.3, however, these estimates represent a conservative estimate of the azimuthal average. More dedicated studies are needed to determine the correct correlation between the stations (see Figure 8.11). This work also presented a framework for performing the muon-weighted average of the field map to determine $\widetilde{\omega}_p$. The actual averaging is awaiting input from the beam dynamics, tracker, and ω_a analyses. The current estimates of the systematic uncertainties from the Run 1 data sets all exceed the 70 ppb error budget allocated to the field analysis for the experiment (see Table 3.2). The interpolation uncertainty estimates for each data set (See summary tables in Chapter IX), in particular, exceed the budgeted 30 ppb. Improvements to the magnet, data taking procedures, and analysis all need to be made to reduce the systematic uncertainties to the budgeted level.

10.1 Future Work

The framework presented in this dissertation is a complete algorithm for calculating field maps given input trolley and fixed probe runs. Final production data sets are not yet available, but when they are, the tools are in place to analyze them. Future work on this analysis is primarily aimed at folding in the beam dynamics and straw tracker analyses to complete the muon-weighted average. By integrating the full field maps produced in this dissertation into the beam tracking simulations, more accurate models of the beam profile in the ring can be generated, which in turn can improve the field average. Further work is also needed to properly average the ratio of the the muon-weighted field average $\widetilde{\omega}'_p$ with the measurement of the anomaly frequency ω_a in Equation 3.5 to calculate a value for a_μ.

There is also the possibility of moving to an interpolation framework based on 3D field moments, instead of the 2D moments used in this analysis. A fully 3D framework has the advantage of being better motivated physically. The 2D moment derivation assumes that there is no dependence of the field on the third dimension. There have been several attempts to derive an accurate framework for 3D moments, but so far, none have been implemented in the full interpolation.

The largest source of uncertainty in the interpolation comes from the higher-order moment drift, estimated by the sync offsets. Further studies that correlate the trolley and fixed probe measurements over long periods of time (see Section 8.3.4) would ideally be performed at all 72 stations. A model of the time dependence of higher-order moment drift would help correct the fixed probe measurements, and reduce the uncertainty in the field measurement by determining the station-wise correlations in the sync offsets. Further studies that correlate the sync offsets to differences in the higher-order moments between trolley runs could also be performed to support Concept 1. Such a model might be generated by an in-depth analysis of the diurnal field cycles and the temperature of the magnet, although both are very complicated and would require detailed dedicated studies. An improved trolley run method would also improve the interpolation uncertainty, which is dominated by stations with poor resolution. In Run 1, the trolley continuously moved as it mapped the field, but this method introduces uncertainty from both the motional effects and by reducing the averaging time for poor resolution fixed probe stations to synchronize with the trolley. More frequent trolley runs could also minimize the uncertainties caused by higher-order moment drifts.

APPENDICES

APPENDIX A

Data Set Definitions

Production data are generated from the raw data by the field production team. The production data sets include the extracted frequencies from the NMR probes, the trolley positions, and data quality flags that mark individual events as good or problematic. The framework that produces the production data is still being updated as improved frequency extraction algorithms are implemented and new methods for flagging poor quality data are developed. The production data used in this work are from version v9_20_00 of the production. Table A.1 lists all of the production data runs by data set in Run 1, as well as the dates of each data set.

Date (2018)	Name	Trolley Runs	Fixed Probe Runs	Notes
4/22 - 4/24	60 Hour	3956, 3997	3959-3994	
4/26 - 5/02	High Kick	4058, 4098, 4138	4061-4095, 4101-4121, 4123-4136	No run 4122 exists.
5/04 - 5/12	9 Day	4138, 4181, 4189, 4226, 4265, 4493	4141-4179, 4193-4222, 4229-4262, 4283-4488	
5/17 - 5/19	Low Kick	4539, 4584	4542-4581	
6/06 - 6/29	End Game	4997, 5054, 5105, 5117, 5157, 5169, 5217, 5259, 5303	5000-5049, 5057-5100, 5120-5154, 5172-5214, 5220-5256, 5262-5300	Trolley run 5303 did not complete.

Table A.1: The data sets referenced in this work, and the field run numbers associated with them.

BIBLIOGRAPHY

BIBLIOGRAPHY

[1] B. Odom, D. Hanneke, B. D'urso, and G. Gabrielse, "New measurement of the electron magnetic moment using a one-electron quantum cyclotron," *Physical Review Letters*, vol. 97, no. 3, 2006.

[2] G. W. Bennett *et al.*, "Final report of the E821 muon anomalous magnetic moment measurement at BNL," *Physical Review D*, vol. 73, p. 072003, Apr. 2006.

[3] T. D. Lee and C. N. Yang, "Question of parity conservation in weak interactions," *Physical Review*, vol. 104, no. 1, pp. 254–258, 1956.

[4] C. S. Wu, E. Ambler, R. W. Hayward, D. D. Hoppes, and R. P. Hudson, "Experimental test of parity conservation in beta decay [5]," 1957.

[5] B. L. Roberts, "The history of the muon (g-2) experiments," *SciPost Physics Proceedings*, Nov. 2019.

[6] R. L. Garwin, D. P. Hutchinson, S. Penman, G. Shapiro, D. P. Hutchinsqn, S. Penman, and G. Shapirq, "Accurate Determination of the μ^+ Magnetic Moment," *Physical Review*, vol. 118, pp. 271–283, Apr. 1960.

[7] J. Schwinger, "On quantum-electrodynamics and the magnetic moment of the electron [9]," *Physical Review*, vol. 73, no. 4, pp. 416–417, 1948.

[8] G. Charpak, F. J. Farley, R. L. Garwin, T. Muller, J. C. Sens, and A. Zichichi, "A new measurement of the anomalous magnetic moment of the muon," *Physics Letters*, vol. 1, pp. 16–20, Apr. 1962.

[9] J. Bailey, W. Bartl, G. Von Bochmann, R. C. Brown, F. J. Farley, H. Jöstlein, E. Picasso, and R. W. Williams, "Precision measurement of the anomalous magnetic moment of the muon," *Physics Letters B*, vol. 28, pp. 287–290, Dec. 1968.

[10] J. Bailey *et al.*, "Final report on the CERN muon storage ring including the anomalous magnetic moment and the electric dipole moment of the muon, and a direct test of relativistic time dilation," *Nuclear Physics, Section B*, vol. 150, no. C, pp. 1–75, 1979.

[11] NIST, "The NIST Reference on Constants, Units, and Uncertainty," 2019.

[12] A. Keshavarzi, D. Nomura, and T. Teubner, "Muon g-2 and α (MZ2): A new data-based analysis," *Physical Review D*, vol. 97, June 2018.

[13] J. D. Jackson, *Classical Electrodynamics*. John Wiley & Sons, Inc., second ed., 1975.

[14] M. E. Peskin and D. V. Schroeder, *An Introduction to Quantum Field Theory*. Westview Press, 1995.

[15] M. Tanabashi *et al.*, "Review of Particle Physics," Aug. 2018.

[16] T. Aoyama, M. Hayakawa, T. Kinoshita, and M. Nio, "Complete tenth-order QED contribution to the Muon g-2," *Physical Review Letters*, vol. 109, Sept. 2012.

[17] T. Aoyama, T. Kinoshita, and M. Nio, "Revised and improved value of the QED tenth-order electron anomalous magnetic moment," *Physical Review D*, vol. 97, Feb. 2018.

[18] R. Bouchendira, P. Cladé, S. Guellati-Khélifa, F. Nez, and F. Biraben, "New Determination of the Fine Structure Constant and Test of the Quantum Electrodynamics," *Physical Review Letters*, vol. 106, p. 080801, Feb. 2011.

[19] C. Gnendiger, D. Stöckinger, and H. Stöckinger-Kim, "The electroweak contributions to (g-2)μ after the Higgs-boson mass measurement," *Physical Review D - Particles, Fields, Gravitation and Cosmology*, vol. 88, Sept. 2013.

[20] M. Davier, A. Hoecker, B. Malaescu, and Z. Zhang, "Reevaluation of the hadronic vacuum polarisation contributions to the Standard Model predictions of the muon g- 2 and α(mZ2) using newest hadronic cross-section data," *European Physical Journal C*, vol. 77, Dec. 2017.

[21] F. Jegerlehner, "Leading-order hadronic contribution to the electron and muon g-2," *EPJ Web of Conferences*, vol. 118, p. 01016, 2016.

[22] A. Kurz, T. Liu, P. Marquard, and M. Steinhauser, "Hadronic contribution to the muon anomalous magnetic moment to next-to-next-to-leading order," *Physics Letters, Section B: Nuclear, Elementary Particle and High-Energy Physics*, vol. 734, pp. 144–147, June 2014.

[23] T. Blum, P. A. Boyle, V. Gülpers, T. Izubuchi, L. Jin, C. Jung, A. Jüttner, C. Lehner, A. Portelli, and J. T. Tsang, "Calculation of the Hadronic Vacuum Polarization Contribution to the Muon Anomalous Magnetic Moment," *Physical Review Letters*, vol. 121, July 2018.

[24] G. Abbiendi, C. M. Calame, U. Marconi, C. Matteuzzi, G. Montagna, O. Nicrosini, M. Passera, F. Piccinini, R. Tenchini, L. Trentadue, and G. Venanzoni, "Measuring the leading hadronic contribution to the muon g-2 via μe scattering," *European Physical Journal C*, vol. 77, Mar. 2017.

[25] J. Prades, E. de Rafael, and A. Vainshtein, "The Hadronic Light-by-Light Scattering Contribution to the Muon and Electron Anomalous Magnetic Moments," in *Lepton Dipole Moments*, pp. 303–317, World Scientific, Apr. 2010.

[26] A. Nyffeler, "Precision of a data-driven estimate of hadronic light-by-light scattering in the muon g-2: Pseudoscalar-pole contribution," *Physical Review D*, vol. 94, Sept. 2016.

[27] N. Asmussen, A. Gérardin, A. Nyffeler, and H. B. Meyer, "Hadronic light-by-light scattering in the anomalous magnetic moment of the muon," in *The 15th International Workshop on Tau Lepton Physics*, (Amsterdam, The Netherlands), Sept. 2018.

[28] W. J. Marciano, "Muon anomalous magnetic moment: A harbinger for "new physics"," *Physical Review D - Particles, Fields, Gravitation and Cosmology*, vol. 64, no. 1, p. 10, 2001.

[29] D. Stöckinger, "(g-2) muon and physics beyond the Standard Model," *Nuclear Physics B - Proceedings Supplements*, vol. 181-182, pp. 32–36, Sept. 2008.

[30] K. Hagiwara, K. Ma, and S. Mukhopadhyay, "Closing in on the chargino contribution to the muon g-2 in the MSSM: current LHC constraints," *Physical Review D*, vol. 97, June 2018.

[31] A. Cherchiglia, D. Stöckinger, and H. Stöckinger-Kim, "Muon g-2 in the 2HDM: Maximum results and detailed phenomenology," *Physical Review D*, vol. 98, Aug. 2018.

[32] M. Krawczyk, "The new (g-2) for muon measurement and limits on the light Higgs bosons in 2HDM (II)," *arXiv*, Mar. 2001.

[33] C. Y. Chen, H. Davoudiasl, W. J. Marciano, and C. Zhang, "Implications of a light "dark Higgs" solution to the gμ-2 discrepancy," *Physical Review D*, vol. 93, Feb. 2016.

[34] M. Raggi and V. Kozhuharov, "Results and perspectives in dark photon physics," *Rivista del Nuovo Cimento*, vol. 38, pp. 449–505, Oct. 2015.

[35] M. Pospelov, "Secluded U(1) below the weak scale," *Physical Review D - Particles, Fields, Gravitation and Cosmology*, vol. 80, Nov. 2009.

[36] M. Ablikim *et al.*, "Dark photon search in the mass range between 1.5 and 3.4 GeV/c2," *Physics Letters, Section B: Nuclear, Elementary Particle and High-Energy Physics*, vol. 774, pp. 252–257, Nov. 2017.

[37] S. N. Gninenko, N. V. Krasnikov, and V. A. Matveev, "Muon g-2 and searches for a new leptophobic sub-GeV dark boson in a missing-energy experiment at CERN," *Physical Review D - Particles, Fields, Gravitation and Cosmology*, vol. 91, May 2015.

[38] H. Davoudiasl, H. S. Lee, and W. J. Marciano, "Muon g-2, rare kaon decays, and parity violation from dark bosons," *Physical Review D - Particles, Fields, Gravitation and Cosmology*, vol. 89, May 2014.

[39] W. J. Marciano, A. Masiero, P. Paradisi, and M. Passera, "Contributions of axionlike particles to lepton dipole moments," *Physical Review D*, vol. 94, Dec. 2016.

[40] J. Grange *et al.*, "Muon (g-2) Technical Design Report," p. 666, Jan. 2015.

[41] B. Kiburg, "Fermilab e989, new muon g-2 docdb 4171-v4," *Internal*, July 2016.

[42] M. Farooq, *Absolute Magnetometry with ^{3}He: Cross Calibration with Protons in Water*. PhD thesis, University of Michigan, 2019.

[43] D. Flay, "Fermilab e989, new muon g-2 docdb 18025-v1," *Internal*, May 2019.

[44] S. Corrodi, "Fermilab e989, new muon g-2 docdb 18016-v1," *Internal*, May 2019.

[45] B. Carter, "Filter design in thirty seconds." `https://www.ti.com/lit/an/sloa093/sloa093.pdf`, Dec. 2001. Online.

[46] NIST, "Uncertainty of measurement results." `https://physics.nist.gov/cuu/Uncertainty/basic.html`. Online.

[47] D. Flay *Private communication*, Oct 2019.

[48] D. Flay, "Fermilab e989, new muon g-2 docdb 19877-v1," *Internal*, Oct 2019.

[49] S. Corrodi, "Fermilab e989, new muon g-2 docdb 14280-v1," *Internal*, Oct 2018.

[50] A. Tewsley-Booth and T. Chupp, "Fermilab e989, new muon g-2 docdb 17287-v1," *Internal*, Apr 2019.

[51] R. Hong, "Fermilab e989, new muon g-2 docdb 18347-v2," *Internal*, Jul 2019.

[52] S. Smith, *The Scientist & Engineer's Guide to Digital Signal Processing*. California Technical Pub, 1997.